EXTREME TEMPERATURE EVENTS

CAUSED BY CLIMATE CHANGE AND VARIABILITY:

DRIVERS AND ITS IMPACT

A Dissertation

by

JANGHO LEE

Submitted to the Graduate and Professional School of
Texas A&M University
in partial fulfillment of the requirements for the degree of

DOCTOR OF PHILOSOPHY

Chair of Committee,	Andrew E. Dessler
Committee Members,	John Nielsen-Gammon
	Yangyang Xu
	Ping Chang
Head of Department,	R. Saravanan

May 2023

Major Subject: Atmospheric Sciences

ABSTRACT

This dissertation investigates extreme temperature events, their drivers, and their impact on society across three main sections. As the climate warms, understanding these events and their consequences becomes increasingly important for developing adaptation strategies and informing policy decisions.

In the first section, the dissertation examines the role of global warming and the internal variability of climate systems in extreme heat and humidity events using a large ensemble of climate models. It is found that extreme heat and humidity events significantly elevate between 1.5°C and 2.0°C of global warming. The El-Niño Southern Oscillation is the largest driver of extreme heat and humidity events on a smaller scale, while global warming becomes more significant when looking at larger regions. With 3°C of warming, 10% of the population will experience extreme heat conditions, and regions with lower GDP will be more vulnerable to extreme heat events. This highlights the need for targeted adaptation strategies in vulnerable regions.

The second section evaluates the impact of climate change on Texas' energy sector, focusing on the Electric Reliability Council of Texas (ERCOT), which controls the state's electric power. An empirical model for estimating power demand based on temperature is developed, accounting for the insufficiency of using only the last decade of temperature data for calculating seasonal power demand. The model reveals a 17% and 19% chance of power demand exceeding extreme peak-load scenarios in summer and winter, respectively. In the Texas winter storm Uri, the study concludes that power demand exceeded ERCOT's extreme peak load scenario by 15 GW or 22%, emphasizing the need for improved demand forecasting and infrastructure resilience.

The final section investigates the impact of climate change on temperature-related deaths in the United States. A temperature-mortality relationship for 106 cities is established, and a model is developed to approximate the role of adaptation by comparing cities with different climates. Using high-resolution climate model outputs, future temperature-related deaths are projected under various adaptation scenarios. At 3°C of global average warming, temperature-related deaths will reach 175,000 per year, a significant increase from the current 37,000 deaths. Adaptation can minimize this increase by 37,000 per year, with a notable northward shift in temperature-related deaths. This underscores the importance of proactive adaptation measures to minimize the human cost of climate change.

This dissertation serves as a capstone project for climate informatics, which combines climate data with data from other sectors to investigate the climate impact. Its findings contribute to a deeper understanding of extreme temperature events and their consequences, offering insights for effective adaptation strategies and policymaking in a warmer climate.

CONTRIBUTORS AND FUNDING SOURCES

Contributors

This work was supervised by a thesis committee consisting of Professors Andrew E. Dessler, John Nielsen-Gammon, Yangyang Xu of the Department of Atmospheric Sciences and Professor Ping Chang of the Department of Oceanography.

All other work conducted for the thesis dissertation was completed by the student independently.

Funding Sources

Graduate study was supported by a fellowship from Texas A&M University.

This work was also made possible in part by the National Science Foundation under Grant Number AGS-1661861 and AGS-1841308. Its contents are solely the responsibility of the authors and do not necessarily represent the official views of the National Science Foundation.

TABLE OF CONTENTS

LIST OF FIGURES

FIGURE Page

LIST OF TABLES

CHAPTER I

INTRODUCTION

1.1. Motivation

Since the industrial period, anthropogenic activities, mainly CO_2 emissions, have altered the long-term climate. Due to this climate change, not only the global average temperature has increased. Since extreme climate events occur from the combination of high mean and high variability of the climate, climate change overall has increased multiple climate hazards.

Recently, the impact of extreme temperature events has received considerable attention due to its frequency, magnitude, and impact. For example, Pacific Northwest heat wave in 2021 (Overland, 2021; Patel et al., 2022; Silberner, 2021; Vasquez, 2022) left billions of dollars of damages, including collapse of infrastructure that could not tolerate the heat. Society is still vulnerable to extreme climate variability, not only extreme heat, but also to extreme cold. Winter storm Uri, which occurred in Texas 2021, has caused power outages leading to hundreds of tens of billions of dollars of damage (Busby et al., 2021; Doss-Gollin, Farnham, Lall, & Modi, 2021; Ivanova, 2021; C. W. King et al., 2021; Ulrich, 2022). Thus, it is important to thoroughly investigate the physical drivers of extreme temperatures along with their impact on human and natural systems.

This doctoral study tackles major scientific questions regarding drivers and impact of extreme temperature events, and further suggests the possibility of incorporating climate data effectively with other sectors of society which can be used for climate informatics.

1.2. Background and Literature Review

Three levels of analysis should be performed to thoroughly investigate extreme temperature events. The first is determining the causes of extreme temperature events, and the second is quantifying the change in temperature and temperature metric due to those causes. Lastly, the impact of extreme temperature events in our society and a range of diverse natural systems should be studied.

1.2.1. Drivers of Extreme Temperature Events

Regarding the drivers of extreme temperature events, a few prevalent drivers influence extreme temperature events: external forcing, internal variability, and local modulation of temperature. External forcings, which come from anthropogenic or natural activities, drive energy imbalances in the climate system. These have been investigated in previous studies and it has been concluded that they modulate the frequency and magnitude of extreme temperature events. For the anthropogenic effect, global average temperature increase due to emission of greenhouse gases, also known as global warming, is the major contributor (Allen et al., 2019; Frölicher, Winton, & Sarmiento, 2014). For the natural part of external forcing, intensity of solar output (Erlykin, Sloan, & Wolfendale, 2009) and impact of Milankovitch cycle (Marsh, 2014) have been studied. Volcanic eruptions (Black, Lamarque, Marsh, Schmidt, & Bardeen, 2021; H. Zhang et al., 2022) are another example of natural forced change, which alters regional and global temperature for relatively short-term.

Internal variability is unforced variability that comes from the chaotic nature of climate system. Mechanisms of internal variabilities impacting extreme temperature events has been studied intensively, where major modes of variability include El Niño Southern Oscillation (ENSO) (Birk,

Lupo, Guinan, & Barbieri, 2010; Meehl, Tebaldi, Teng, & Peterson, 2007; Thirumalai, DiNezio, Okumura, & Deser, 2017), Pacific Decadal Oscillation (PDO) (Birk et al., 2010; G. Zhang, Zeng, Li, & Yang, 2020), Atlantic Multi-decadal Oscillation (AMO) (G. Zhang et al., 2020), and Northern Atlantic Oscillation (NAO) (Moore & Renfrew, 2012). These major modes of variability are known to have bi-annual to decadal oscillations and known to impact regional and global extreme temperature events.

Local modulators of large-scale extreme heat events come from small-scale phenomenon, such as city-level urban heat island (UHI) effect. UHI effect is a phenomenon in which urban built-up areas are significantly warmer than surrounding rural areas and it can contribute to local extreme heat event (Jay et al., 2021; Mallen, Stone, & Lanza, 2019; Qian et al., 2022).

Local extreme temperature events are always a combination of long-term forced change, acting in concert with internal variability of climate and local modulators. So, it is critical to determine the mechanism of each driver to comprehend the nature of extreme temperature events, and for assessing the future risk of extreme events.

1.2.2. Change in Temperature and Temperature Metric

Although we physically understand the drivers of extreme temperature events, it is also important to quantify the change of temperature each drivers results in. For example, multiple studies quantitively linked long-term forced change with extreme heat (Allen et al., 2019; Masson-Delmotte et al., 2018). Furthermore, previous studies identified how much ENSO (Feng & Hao, 2021; Hao, Hao, Singh, & Zhang, 2018; Seager, Kushnir, Nakamura, Ting, & Naik, 2010), PDO (Mariano, Carolina, & Miranda Leandro, 2018; G. Zhang et al., 2020), AMO (Shi et al., 2018; Zhou & Wang, 2016), and NAO (López-Moreno et al., 2011; Moore & Renfrew, 2012) increase

or decrease local extreme temperature event.

Furthermore, since temperature is a representation of only one single metric, other metrics such as the absolute increase of maximum temperature from the reference period (Wobus et al., 2018), risk ratio of population's exposure to heat (Kharin et al., 2018), wet-bulb temperature (Heo, Bell, & Lee, 2019), and heat wave magnitude index (S. Russo, Sillmann, & Sterl, 2017) are used for detailed assessment of extreme temperature event.

1.2.3. Impact of Extreme Temperature Events

One of the important motivations to conduct research on extreme temperature events is because it has a significant impact on human and natural systems. Thus, it is essential to investigate the impact of extreme temperature on those systems. This topic is often referred to as climate impacts research, where researchers incorporate climate data with data from other sectors to assess the impact of climate. Several sectors of human and natural systems have been studied in this aspect.

Impact on human system includes the energy sector, public health, economic inequity, agriculture, and dairy farming (IPCC, 2022). Impacts on the natural system have also been analyzed. For the cryosphere, previous studies mainly focused on ice sheet and permafrost melting (Colucci & Guglielmin, 2019; Koenigk, Key, & Vihma, 2020; Naughten et al., 2021; Stokes et al., 2022). Studies of the ocean biosphere have analyzed animal biomass (Chapman, Lea, Meyer, Sallée, & Hindell, 2020) and primary production in the ocean (Kulk et al., 2020).

1.2. Dissertation Outline

This dissertation aims to examine extreme temperature events from cause to impact.

Chapter 2 employs a single-model initial-condition large ensemble (SMILE) of global climate

model (GCM) to investigate the causes of extreme heat and humidity events, as well as the corresponding increase in temperature and humidity metrics. Using a SMILE allows us to separate increasing temperature and extreme heat events into forced change (global warming) and internal variability components. Furthermore, in this chapter, per capita gross domestic product data, as well as energy-related metrics, including cooling degree days and warming degree days, are used to quantify the impact of global warming on economic inequity and energy demand.

Chapter 3 of the dissertation moves to the impact sector of extreme temperature events. The Electric Reliability Council of Texas (ERCOT) manages the grid that supplies electricity to the majority of Texas residents. However, when projecting potential power demand, ERCOT only uses weather data from the previous decade, ignoring changing climate and climate variability beyond the recent historical record. In this section, we propose a new method for using a SMILE to generate realistic probability-based future weather forecasts to predict Texas energy demand.

Chapter 4 focuses on temperature-related deaths in the US. Three factors influence future temperature-related deaths. The first is the magnitude of climate change, followed by demographic and population change. The final factor is society's adaptation to the warming temperature. In this section of the dissertation, we integrate future climate scenarios, demographic and population projections, and adaptation assumptions to create a comprehensive framework for projecting future temperature-related deaths.

Chapter 5 synthesizes this study's findings about extreme temperature events and provides concluding remarks and implications for the future work.

CHAPTER II

THE EFFECT OF FORCED CHANGE AND UNFORCED VARIABILITY ON HEAT WAVES, TEMPERATURE EXTREMES, AND ASSOCIATED POPULATION RISK IN A CO_2-WARMED WORLD[*]

2.1. Introduction

The long-term goal of the 2015 Paris agreement is to keep the increase in global temperature well below 2°C above pre-industrial levels, while pursuing efforts to limit the warming to 1.5°C. Given that no one lives in the global average, however, understanding how these global average thresholds translate into regional occurrences of extreme heat and humidity is of great value (Harrington, Frame, King, & Otto, 2018). Previous studies have reported that regional extreme heat events will not only be more frequent, but also more extreme in a warmer world. This was discussed in various assessment and reports such as US National Climate assessment and those by IPCC (Hoegh-Guldberg et al., 2018; Masson-Delmotte et al., 2018; Melillo, Richmond, & Yohe, 2014; Wuebbles, Fahey, & Hibbard, 2017) and it is expected to have significant impacts on human society and health. More importantly, previous studies have analyzed the risk (Lundgren, Kuklane, Gao, & Holmer, 2013; Quinn et al., 2014; Sun et al., 2014), exposure (Dahl, Licker, Abatzoglou, & Declet-Barreto, 2019; Liu et al., 2017; Luber & McGeehin, 2008; Ruddell, Harlan, Grossman-Clarke, & Buyantuyev, 2009), vulnerability (Chow, Chuang, &

[*] Reprinted with permission from "The effect of forced change and unforced variability in heat waves, temperature extremes, and associated population risk in a CO2-warmed world" by Jangho Lee, Jeffrey C. Mast, and Andrew E. Dessler, 2021. *Atmospheric Chemistry and Physics*, 21, 11889-11904, Copyright 2021 by Jangho Lee

Gober, 2012; Wilhelmi & Hayden, 2010) and susceptibility (Arbuthnott, Hajat, Heaviside, & Vardoulakis, 2016) of population in the current and warmer climates.

Many criteria and indices have been used to assess extreme heat, such as the absolute increase of maximum temperature from the reference period (Wobus et al., 2018), risk ratio of population's exposure to heat (Kharin et al., 2018), and heat wave magnitude index (S. Russo et al., 2017). In this study, we utilize four locally defined heat wave indices from Fischer and Schär (2010) and Perkins, Alexander, and Nairn (2012) of duration, frequency, amplitude, and mean. We also focus on consecutive-day extremes, which are known to cause more harm than single-day events (Baldwin, Dessy, Vecchi, & Oppenheimer, 2019; Simolo, Brunetti, Maugeri, & Nanni, 2011; Tan et al., 2010). In addition, because the combined effect of temperature and humidity is known to affect human health by reducing the body's ability to cool itself through perspiration, wet-bulb temperature is frequently analyzed (Kang & Eltahir, 2018), so we will analyze wet-bulb temperature also.

Climate extremes often occur from a combination of long-term forced climate change acting in concert with unforced variability (Deser, Phillips, Bourdette, & Teng, 2012). Thus, characterizing and quantifying both long-term change due to external forcing and the unforced variability of the climate system is crucial in assessing the future risk of extreme events. There have been numerous studies that link dominant modes of unforced variability to extreme events. For example, previous studies have investigated temperature connections with El Niño Southern Oscillation (ENSO) (Meehl et al., 2007; Thirumalai et al., 2017), the Pacific Decadal Oscillation (PDO) (Birk et al., 2010) , the Atlantic Multidecadal Oscillation (AMO) (Mann, Steinman, Brouillette, & Miller, 2021; G. Zhang et al., 2020). The effect of climate extremes on different populations depends on numerous factors, including the level of economic development, with

impacts of heat extremes being more severe in less economically developed countries (de Lima et al., 2021; Diffenbaugh & Burke, 2019; Harrington et al., 2016; A. D. King & Harrington, 2018). For example, as temperatures go up, increased energy demand to cool buildings will be required (Parkes, Cronin, Dessens, & Sultan, 2019; Sivak, 2009) in metropolitan area. But this requires resources to both install air conditioning and then operate it. The greater impacts of extreme heat in economically less developed region in a warmer climate has been discussed in multiple studies (Marcotullio, Keßler, & Fekete, 2021; Simone Russo et al., 2019).

In this paper, a single-model initial-condition ensemble of 28 simulations of a global climate model (GCM) are used to quantify heat and humidity extremes in a warmer world. We use population data to look at population risk for mortality events in daytime (Mora et al., 2017) and nighttime (Chen & Lu, 2014). We also utilize per capita gross domestic product (GDP per capita) data to investigate how climate change impacts extreme heat events on different levels of economic status. To quantify the impact on energy demand, we also quantify changes in cooling degree days and warming degree days.

2.2. Data

2.2.1. MPI-GE ensembles

Simulation data in this study come from an ensemble of runs of the Max-Plank Institute Earth System Model collectively known as the MPI Grand Ensemble (MPI-GE) project (Maher et al., 2019). Each of the 28 ensemble members branches from different points of a 2000-year pre-industrial control run and are integrated for 150 years, forced by CO_2 concentration increasing at 1% per year (hereafter, 1% runs). Because the radiative forcing scales as the log of CO_2 concentration, the 1% runs feature radiative forcing that increases approximately linearly in time.

We analyze 6-hourly output with 1.875° × 1.875° spatial resolution, which is the original resolution of the model output, for land areas between 60°N and 60°S. Our analysis will focus on 2-meter temperature (hereafter, t2m) and 2-meter dew point temperature (d2m), from which 2-meter relative humidity (rh) and wet-bulb temperature (w2m) are calculated using the methods of Davies-Jones (2008) with a predesigned module, HumanIndexMod (J. Buzan, Oleson, & Huber, 2015).

Unforced variability in the climate system generates uncertainties in the projection of the climate by impacting the dynamic component of the climate, especially for extreme events (J. E. Kay et al., 2015; Thompson, Barnes, Deser, Foust, & Phillips, 2015). One way to analyze the impact of unforced variability in climate system is to use an initial-condition ensemble. Each members of initial-condition ensemble are generated by perturbating the initial conditions of single climate model. This perturbation will then propagate to generate different sequence of climate, such as ENSO, PDO, etc. (Deser et al., 2012; J. E. Kay et al., 2015). In this paper, we use the ensemble to allow us to estimate the impact of unforced variability on temperature extremes.

Since the model used only considers CO_2 forcing without aerosols, and it represents a continuously warming climate, one might question if the model simulation accurately represents the real climate. To judge the fidelity of the simulations, we compare 15 years (2003-2017) of ERA-Interim reanalysis data (Dee et al., 2011) from the European Centre for Medium Range forecast (ECMWF) with 15 years of the MPI-GE 1% ensemble which have the same ensemble- and global-average temperatures (years 39-53); in the rest of the paper, we will refer to these as the reference periods. In both data sets, we then calculate 90^{th} percentile and mean t2m and w2m for each grid points. This calculation was done for each member of the model ensemble. For each of the 4 values (90^{th} percentile t2m/w2m and mean t2m/w2m), we determine if the values from the

reanalysis fall into the spread of 28 ensemble members of the 1% runs. For each grid point, if the reanalysis value falls within the ensemble spread, we mask out the grid point; if not, we plot how far the reanalysis value is from the closest member of the 1% ensemble (Figure 2.1).

Generally, the 1% runs overpredicts t2m and w2m in Northern hemisphere, and underpredicts in Southern hemisphere, except for India. This difference is consistent with the fact that the 1% models do not contain aerosol forcing, which should lead to biases of the sign seen in Fig. 2.1. The w2m shows larger area of differences than t2m, which suggests that there are larger biases in the dew point, which is needed in the calculation (Davies-Jones, 2008). The area-weighted averages of these differences are -0.08°C, -0.03°C, -0.04°C, and -0.11°C globally for 90^{th} percentile t2m, mean t2m, 90^{th} percentile w2m, and mean w2m respectively, which means that the model is, on average, underpredicting land temperature. Breaking down to Northern and Southern hemisphere, the bias is 0.20°C, 0.21°C, 0.15°C, 0.14°C in NH and -0.64°C, -0.54°C, -0.36°C, and -0.44°C, confirming that the model is overpredicting temperature in NH land and underpredicting in SH land.

To quantify the impact of the biases in Fig. 2.1 on the occurrence of heat extremes, we will perform sensitivity tests on the calculations by adding to each grid point of each member of the ensemble the average differences between the ensemble average t2m and w2m and the reanalysis. By evaluating how much our results change, we come up with an estimate of the impact of model biases on our results. As we will show later, these biases have little impact on the results of the paper.

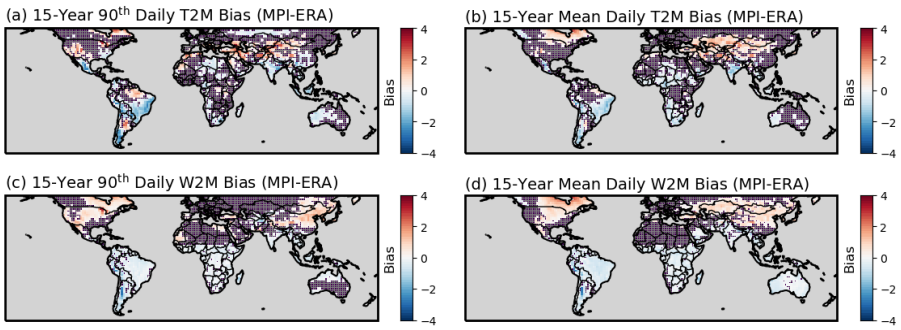

Figure 2.1. Difference of 1% CO_2 runs compared with ERA-Interim in same level of global warming (0.87°C). The grid points where ERA-Interim falls within the ensemble spread of 1% runs are masked with gray, while other grid points show the difference between the nearest ensemble member and ERA-Interim for (a) 90th percentile of 15-year daily average t2m, (b) mean of 15-year daily average t2m, (c) 90th percentile of 15-year daily average w2m, and (d) mean of 15-year daily average w2m.

2.2.2. Global population and GDP per capita data

Global population data from the NASA Socioeconomic Data and Applications Center (SEDAC, 2018) are used to weight the heat wave indices by population. The data represent the population in year 2015 at $30'' \times 30''$ spatial resolution, and we re-gridded to the $1.875° \times 1.875°$ grid of the MPI model by summing the values in grid boxes surrounding the MPI grid centers. In our population-weighted calculations, we assume that the relative distribution of population remains fixed into the future.

Gridded GDP per capita data (Kummu, 2019) over 1990-2015 are used to estimate the risk of heat extreme events for different levels of wealth. These data are re-gridded from the original $5'' \times 5''$ spatial resolution to the MPI model's resolution of $1.875° \times 1.875°$ by averaging the GDP inside the grid box. When doing this average, per capita GDP was weighted by population and

also averaged over the 1990-2015 period. We assume that the relative percentile of GDP per capita for each grid point is fixed into the future, so changes in climate risk are due to exposure to warmer climate extremes, not changes in relative per capita wealth.

2.3. Method of analysis

2.3.1. Global warming

Global warming is defined as the global and annual average temperature increase compared to the average of first 5 years of the 1% run. We find that ensemble- and global-average t2m reaches 1.5°C, 2°C, 3°C and 4°C occur in years 59, 76, 108, and 133 years, respectively, and reaches 4.6°C at the end of the 150-year run. The increase of global average temperature is nearly linear for both t2m and w2m, consistent with a linear ramping of the forcing (J. R. Buzan & Huber, 2020).

The focus on the paper will be on heat extremes at 1.5°C, 2°C and 3°C. The 1.5°C and 2°C thresholds are the limits described in the Paris Agreement, while 3°C is the warming we are presently on track for (Hausfather & Peters, 2020).

2.3.2. Heat wave indices

Identification of heat waves is done in several steps. First, for each grid point, we smooth a daily maximum temperature (determined form 6-hourly temperatures) using a 15-day moving window for the first 5 years of 1% runs, which is the period before significant warming has occurred. Then, the 90^{th} percentile of smoothed daily maximum temperature for the first 5 years was calculated at each grid point (Fischer & Schär, 2010). This value is used as a threshold for the

heat waves at that grid point. Then we calculate the heat wave days, defined as days that exceed the threshold for three or more consecutive days (Baldwin et al., 2019).

We then define four indices to represent the characteristics of these heat waves. To determine the occurrence of events, heat wave duration (HWD; longest heat wave of the year) and heat wave frequency (HWF; total number of heat wave days in a year) are calculated. From an intensity perspective, heat wave amplitude (HWA; maximum temperature during heat wave days during a year) and heat wave mean (HWM; mean temperature during heat wave days in a year) are selected. These indices are also calculated in an analogous fashion for wet bulb temperature (w2m), since wet-bulb temperature is arguably more relevant for human health (J. R. Buzan & Huber, 2020; Heo et al., 2019; Morris, Gonzales, Hodgson, & Tustin, 2019). These indices are summarized in Table 2.l.

2.3.3. Deadly days and tropical nights

Heat wave thresholds are different for each grid point because they are based on pre-industrial temperatures at that grid point. Combined with regional differences in the ability to adapt, this means that heat waves in different regions may have different implications for human society. We therefore also count the number of days each year with daily maximum w2m above 26°C, which we refer to as "deadly days". We note that other values could be chosen (Liang et al., 2011), with higher values occurring less frequently but having more significant impacts. This value is based on the analysis of Mora et al. (2017), who demonstrated that w2m of about 24°C is the threshold which fatalities from heat-related illness occur. However, since we find that there are some regions that already experience over 9 months of 24°C w2m events per year, we increase this threshold to 26°C in our analysis. We could have chosen higher w2m values, but any choice

in this range is associated with negative impacts, so we have chosen a value near the bottom of the range where mortality occurs in order to maximize the signal in the model runs.

A warm nighttime minimum temperature can be as important as a high maximum temperature for human health and mortality (Argaud et al., 2007; Patz, Campbell-Lendrum, Holloway, & Foley, 2005), so we define "tropical nights" as a daily minimum t2m over 25°C (Lelieveld et al., 2012).

2.3.4. Cooling degree days and heating degree days

To assess the economic and energy impact of heat extremes, cooling degree days (CDD) and heating degree days (HDD) are calculated. CDD and HDD are metrics of the energy demand to cool and heat buildings. For each grid point, annual CDD is calculated by subtracting 18°C from the daily average temperature and summing only the positive values over the year. HDD is the absolute value of the sum of the negative values. Previous studies reported that CDD and HDD are closely related to energy consumption (Sailor & Muñoz, 1997).

Table 2.1. Explanation of heat wave indices used in this study.

Acronym	Index	Definition	Units
$HWD_{t2m/w2m}$	Heat wave duration	Length of longest period of consecutive heat wave days in a year	# days
$HWF_{t2m/w2m}$	Heat wave frequency	Total number of heat wave days in a year	# days
$HWA_{t2m/w2m}$	Heat wave amplitude	Maximum temperature over all heat wave days in a year	°C

$HWM_{t2m/w2m}$	Heat wave mean	Average temperature over all heat wave days in a year	°C
Deadly Days	Deadly Days	Daily maximum wet-bulb temperature over 26°C	# days
Tropical Nights	Tropical Nights	Daily minimum temperature over 25°C	# days
CDD	Cooling degree days	Sum of positive values after removing 18°C from daily average temperature	°C days
HDD	Heating degree days	Absolute value of sum of negative values after removing 18°C from daily average temperature	°C days

2.4. Results

2.4.1. Impact of unforced variability of climate on regional heat extremes

To investigate the impact of unforced variability on more regional heat extremes, we take the 15 largest cities by population (Fig. 2.2a) and determine the number of deadly days and tropical nights over time by averaging the heat wave metric of the 3×3 grid points surrounding the city, only including the land grid points. Figure 2.2b-d depicts the ensemble averaged number of deadly days and tropical nights, as well as the spread between the ensemble members. The error bars in Figure b-d show the highest and lowest values of the extremes.

This difference within the ensemble is the result of unforced variability. For all 15 cities, average spread in the number of deadly days at 1.5°C, 2.0°C, 3.0°C, and 4.0°C of global warming between the ensemble members with maximum and minimum numbers are 14.3, 15.1, 20.6, and 21.9 days per year. For tropical nights, the spreads are 29.3, 27.7, 29.1, and 26.7 days on 5-year averaged values. So, on average, unforced variability can change the number of extreme days and

nights by a few weeks per year. There is no significant variance of ensemble spread between the cities except for cities with very low ensemble-averaged values (e.g., Mexico City at 1.5°C warming) or very high values (e.g., tropical nights in Manila at 4.0°C warming). However, for the cities that do not see large increase in extreme temperatures (e.g., New York City), this represents a very large fraction of the predicted change of extremes, while for cities that experience much larger increase (e.g., Manila), it represents a smaller percentage.

As discussed in Section 2.2.1, we examine the sensitivity of our results to potential biases of the model by recalculating the deadly days and tropical nights using model data after adding in the bias estimated by comparison to the reanalysis. The average difference of deadly days in the sensitivity test (absolute difference) at 1.5°C, 2.0°C, 3.0°C, and 4.0°C warming is 2.1, 2.5, 5,5, and 7.6 days per year when averaged over 15 cities. The standard deviation of difference calculated between the cities is 2.5, 3.4, 6.7, and 9.7 days at each level of warming. For tropical nights, sensitivity test produced differences of 3.6, 3.6, 5.3, and 3.5 days per year at each level of warming, with standard deviations within the ensemble of 3.6, 4.9, 6.9, and 1.8 days. Thus, model mean biases are unlikely to have a large impact on our results.

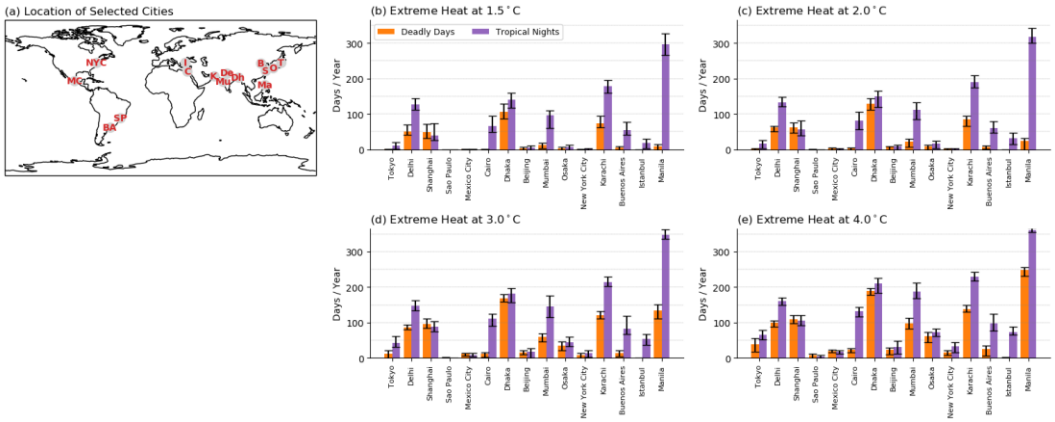

Figure 2.2. (a) Location of 15 largest cities in the world and the number of annual heat extremes at (b) 1.5, (c) 2.0, (d) 3.0, and (e) 4.0°C of global warming. Orange (purple) bars represent the ensemble average annual number of deadly days (tropical nights), averaged 5 years after each level of warming is exceeded. Number of heat extreme days are calculated by averaging 3×3 land-only grid covering the selected city. Error bars represent the values of maximum and minimum ensemble members.

Previous work has attempted to distinguish the mechanisms of unforced variability of temperature and temperature extremes (Birk et al., 2010; Meehl et al., 2007; G. Zhang et al., 2020). To probe the statistical modes of variability affecting this ensemble spread and to identify the underlying physical mechanisms, empirical orthogonal function (EOF) analysis (North, 1984) was performed on the detrended and normalized time series of deadly days and tropical nights for the 15 cities. For each city, the 28 ensemble members are concatenated together (total of 28×150 years) in order for all ensemble to share the same EOF. In this way, we aim to find the dominant drivers of unforced variability that impacts heat extremes in the largest cities around the world.

The first three EOF patterns for each city are plotted in Fig. 2.3 as bars. The first EOF mode of deadly days shows large values for Delhi, Shanghai, Dhaka, and Karachi, while cities in other regions show lower values. The second and third EOFs for deadly days show more variability between the cities. The first EOF for tropical nights (Fig. 2.3d) show large positive values for cities in the India-Pakistan region, with other cities showing smaller magnitude changes. The second EOF shows large negative values in Cairo, Istanbul, and Manila, while the third EOF for tropical nights shows more variability between the cities.

The PC time series are projected onto detrended annual sea surface temperature (SST) anomalies. This allows us to investigate how heat extreme events in 15 major cities are associated with global modes of unforced variability. Maps of correlation coefficients are also plotted in Fig. 2.3. Characteristic patterns for ENSO (Trenberth, 2020), PDO (Deser & Trenberth, 2016), and AMO (Trenberth & Zhang, 2021) are calculated for each ensemble using all 150-year of SSTs, and the pattern is averaged over ensembles to come up with a single ENSO, PDO, and AMO SST pattern for the ensemble. Then, those patterns are compared with the PC projection on SST to see how PC projected SST resembles the patterns of unforced variability. Correlation coefficients between the standard climate indices and PC projected SST is shown on lower panel of Fig. 2.3 as numbers. All of the projections of deadly day PCs and projections of the first two modes of tropical nights shows patterns similar to El Niño-Southern Oscillation (ENSO) and Pacific Decadal Oscillation (PDO).

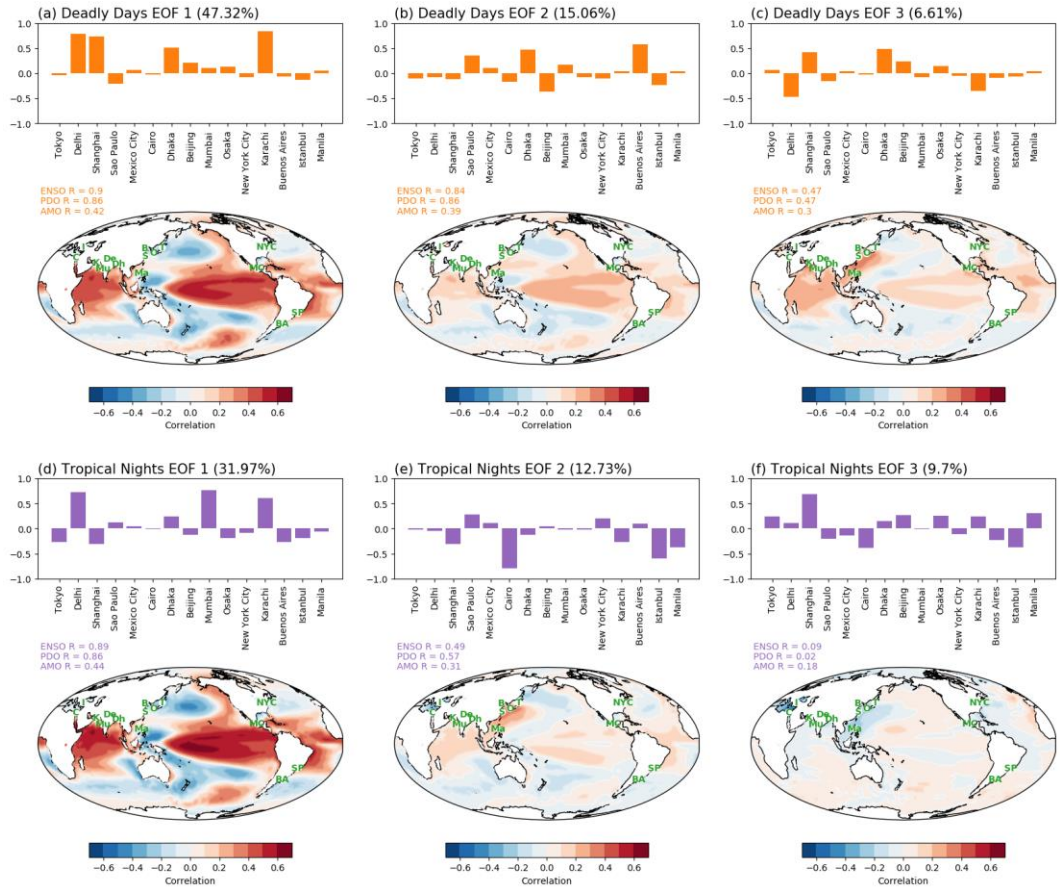

Figure 2.3. First three EOFs of annual values of deadly days (a, b, c) and tropical nights (d, e, f) in the world's 15 largest cities. For each panel, the bar graph shows the EOF pattern of the number of heat extreme days per year. Contour plots shows the SST pattern associated with the EOF mode, obtained by projecting each mode of PC onto SST anomalies. Ensemble members are averaged to yield the SST pattern. Pattern correlation with major modes of climate variability (ENSO, PDO, AMO) are also shown, as discussed in the text.

Power spectra of the PCs are calculated individually for each ensemble member, and then the ensemble average is plotted Figure 2.4. Overall, the spectra of the deadly day PCs look very much like the spectrum for ENSO, and it notably does not have the ~20-year peak of the PDO

spectrum. This tells us that, in this model at least, the variability in the occurrence of deadly days in these four large cities is strongly regulated by ENSO. This may be a consequence of the fact that these large cities are mostly located near ocean and at lower latitudes. The third deadly day PC has lower correlations with ENSO or PDO index, so it is harder to draw firm conclusions about the mechanism behind it. Also, higher modes of EOFs are unlikely to refer to a single mode of climate due to the orthogonality constraints between each mode. The tropical night PCs also show peaks at ENSO periods (Fig. 2.4b) suggesting that, like deadly days, tropical night variability is controlled by ENSO.

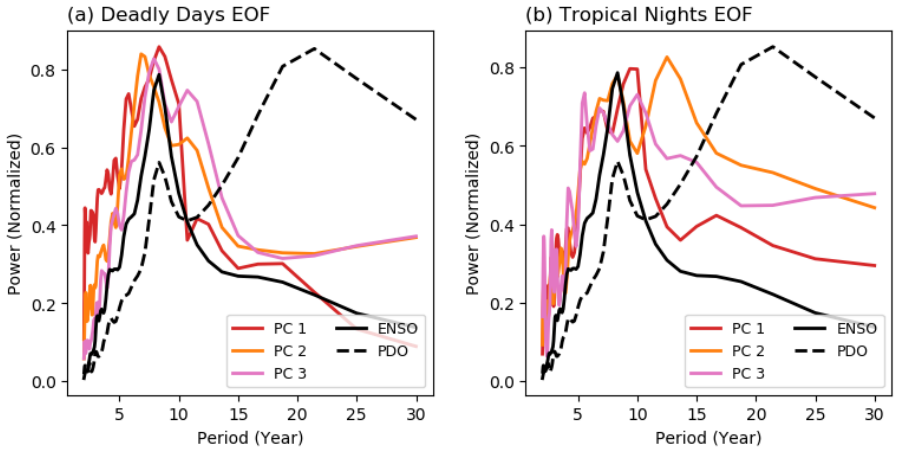

Figure 2.4. Frequency power spectrum of ENSO, PDO, and PC of first three EOF modes for (a) deadly days and (b) tropical nights. ENSO is calculated with the Niño 3.4 Index, and PDO is calculated as a leading EOF of SST anomaly in North Pacific basin. Monthly SST data is used for both ENSO and PDO, and then each index is averaged over the year to have consistency with deadly days and tropical nights.

2.4.2. Cluster analysis and population risk of heat wave indices

We calculate HWD, HWF, HWA, and HWM for both t2m and w2m each year at each grid point, which generates eight different 150-year time series for each of the 28 ensemble members. Each time series at each grid point is regressed vs. time, yielding a slope and the intercept for each time series in all 28 ensemble members. The 16 variables (8 [heat wave indices] × 2 [slope, intercept]) are then utilized as a predictor variable for K-means clustering (Likas, Vlassis, & Verbeek, 2003) to categorize the spatial variation of heat waves using the Euclidean distance of its predictor variables (16 variables). With slope and intercept, we can characterize the heat indices of each grid point with response to CO_2 forcing (slope) and climatology (intercept). The number of clusters in this study is set to 6, using the elbow method (Syakur, Khotimah, Rochman, & Satoto, 2018). When using 5 clusters, we find that two clusters (the light and dark blue regions in Figure 2.5a) merge, and when using 7 clusters, we find that one cluster (the dark blue region in Figure 2.5a) divides into two separate clusters.

Figure 2.5a shows the cluster value that most ensembles assigned to each grid point and it shows distinct geographical characteristics, as summarized in Table 2.2 (the result of clustering shows little difference between individual ensemble members). As might be expected from how we calculated the 16 variables for clustering, each cluster shows a different evolution of heat extremes in warmer world (Figure 2.6). Although the warming signal is largest in the polar regions (Figure 2.5b), the largest increases of HWD and HWF are found at lower latitudes (in cluster 1 and 2 on Figure 2.6a-d). This is mostly due to low variability in these regions compared to polar regions, making it easier for a trend to exceed the heatwave threshold.

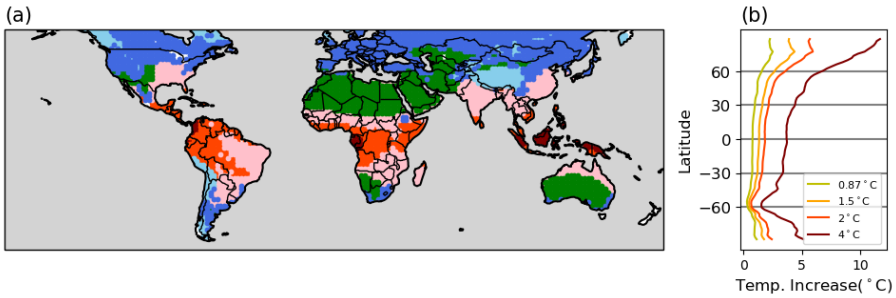

Figure 2.5. (a) Clustered regions via K-means clustering. Characteristics of each cluster are listed in Table 2.2. (b) Zonal average of temperature increases at the time of 0.87°C (our reference period), 1.5°C, 2°C, and 4°C of global warming compared to pre-industrial baseline in the 1% runs. Temperatures are averaged over a 5-year period after each warming threshold is exceed in the model.

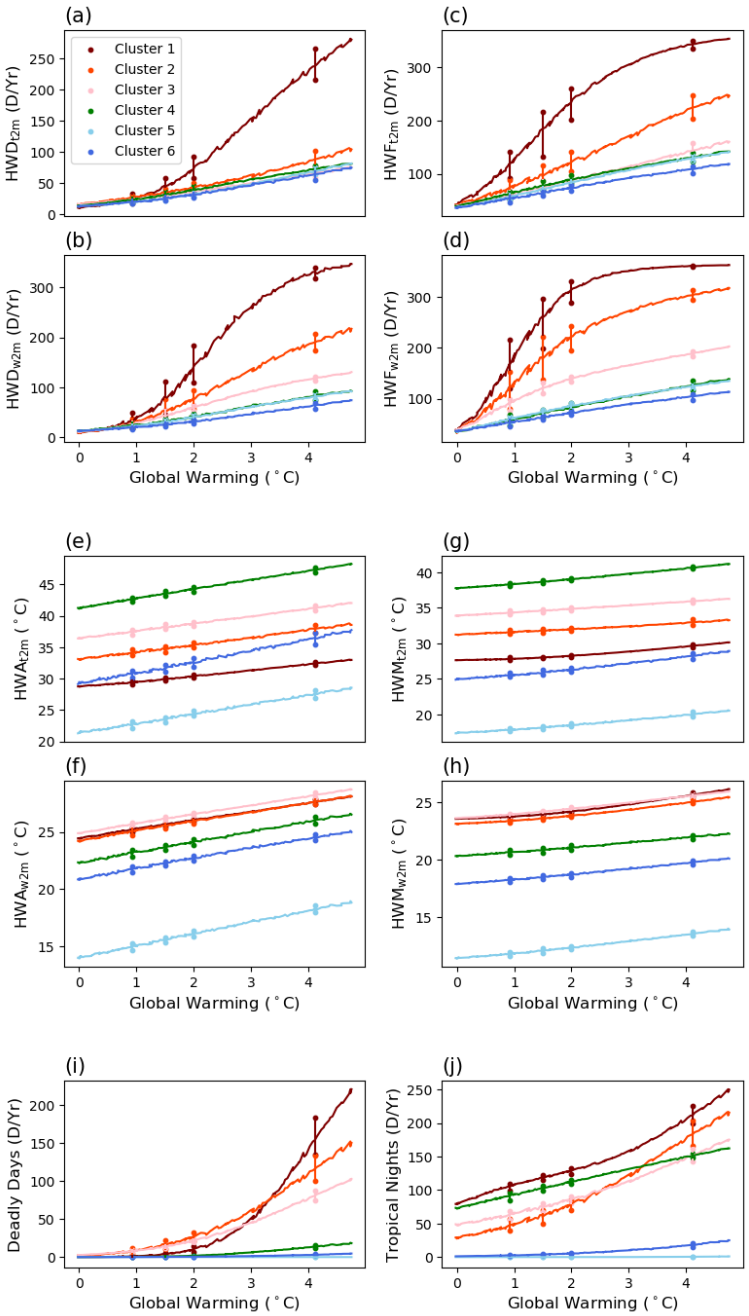

Figure 2.6. Evolution of each index averaged over each cluster. Colors are consistent with Figure 2.5 and Table 2.2. Values of each metric are calculated by averaging the grid points that belongs to each cluster. This was done for each ensemble member and then the ensemble average is plotted.

Vertical lines with dots show the maximum and minimum of 28 ensemble members at each threshold of warming to represent the spread between the ensemble members.

These results are insensitive to potential model biases. Sensitivity tests show that adding the bias to the model changes HWD, HWF, deadly days, and tropical nights, by less than 5% for all metric and clusters. For HWA and HWM, the difference caused by adding the bias was less than 1°C for all metric and clusters, suggesting that the impact of model biases is small in this analysis.

For HWA and HWM, the rate of increase is similar for all clusters, with increases of HWA_{t2m} and HWA_{w2m} of 1.45°C per degree of global average warming and 0.85°C per degree of global average warming, respectively, and HWM_{t2m} and HWM_{w2m} of 0.66°C per degree of global average warming and 0.47°C per degree of global average warming, respectively (Figure 2.6e-h). The exception is HWA_{t2m} in cluster 6. The large increase of HWA_{t2m} in this region is connected to the strong global warming signal in high latitudes that has been predicted for decades and now observed (Stouffer & Manabe, 2017).

Turning to deadly days (Fig. 2.6i), we find a substantial increase occurs in cluster 1 after 2.0°C of warming; this is important because it gives additional support for the Paris Agreement's aspirational goal of limiting global warming to 2.0°C. Almost all increases in deadly days are in low latitudes (cluster 1, 2, and 3). For tropical nights, low latitudes and deserts (cluster 4) contribute most of the increase. Figure 2.6 also shows the spread in within the ensemble for each metric and cluster. We find that the spread for a cluster is generally small compared to the change over time as well as the difference between the clusters.

We also generated indices weighted by global population. Heat wave indices for the 95th percentile of population (meaning 5% of the population is exposed to higher values), 90th percentile of population, and median of the population are depicted in Figure 2.7. Figure 2.7a shows that with 3°C of warming, 5% of the Earth's population will experience heat waves lasting 122 days (standard deviation between ensemble members: 1σ = 17 days), 10% of the population will experience heat waves of 94 days (1σ = 7 days), and half of the population will experience heat waves around 50 days (1σ = 4 days). These are large increases over present-day values of 50, 42, and 21 days. The average of the standard deviation between the ensemble members (calculated every year and then averaged), are 10.6, 6.2 and 3.7 days for the 95th, 90th percentile and median, respectively. This is significantly smaller than values from the analyses of cities in Figure 2.2, where the unforced variability makes larger differences in the occurrence of heat waves.

The rate of increase of HWF_{w2m} in Fig. 2.7d shows a rapid increase until global average warming reaches about 2.5°C. Given that the planet has already warmed about 1°C above pre-industrial, this suggests that the world should presently be experiencing a rapid increase of wet-bulb extreme frequency, particularly in the tropics. This is related to the increased slope in Figure 2.6, in which cluster 1 and 2's values of HWD_{w2m} and HWF_{w2m} increase rapidly until 3.0°C and 2.0°C of global warming. At warmer temperatures, HWD_{w2m} and HWF_{w2m} reach a plateau, since values over 300 days per year means there is little room for additional increase. For $HWA_{t2m/w2m}$ and $HWM_{t2m/w2m}$, the increase is mostly linear. Also note that, at 3°C of global warming, the 90th percentile of population weighted HWA_{w2m} reaches over 29°C, which while not immediately fatal to humans may nevertheless indicate great difficulty for even a developed society to adapt to.

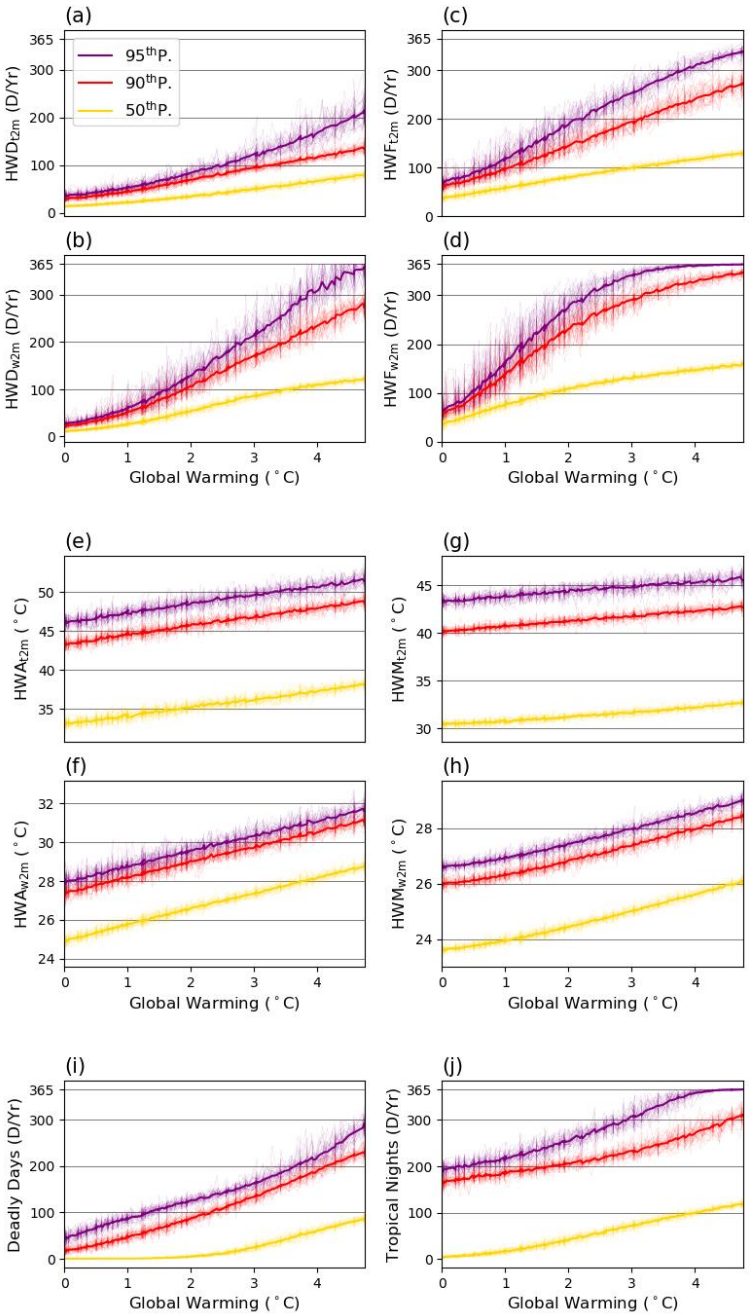

Figure 2.7. Changes of population-weighted heat wave indices as a function of global average warming. Each line denotes one ensemble member for different percentiles of population.

Currently, 10% of the total population faces more than 45 deadly days and 181 tropical nights per year. This grows to 65 and 195 days, respectively, at 1.5°C warming. With 2°C of global warming, 10% of the population will face about 3 months of deadly days and 7 months of tropical nights every year, and this increase to 4 months and 8 months in 3°C of warming. Also, with 3°C of global warming, 5% of the population will be in an environment where 8 months and 10 months in a year is a deadly days and tropical night. Our sensitivity tests suggest that model bias generates less than 5% differences for HWD, HWF, deadly days, and tropical nights for all metrics and percentile of population at every level of global warming, except when the metrics are near-zero. Potential model biases also generate small differences in HWA and HWM, with less than 1°C difference in all metrics for every period. Furthermore, with 3°C of global warming, the minimum ensemble member of deadly days is above the maximum ensemble of the present-day reference (0.87°C) for all population percentiles (5%, 10%, and 50%). This occurs at 2°C for tropical nights. Details of ensemble spread are also shown in Table 2.3.

Table 2.3. Number of deadly days each percentile of global population faces with reference period (0.87°C), 1.5°C, 2°C, 3°C, and 4°C global warming from the pre-industrial condition. Standard deviations between the ensembles (1σ) are also shown.

		Global Warming				
	Population	0.87°C	1.5°C	2.0°C	3.0°C	4.0°C
Deadly Days	95^{th} p.	85 ($\pm$ 7)	105 ($\pm$ 10)	125 ($\pm$ 7)	161 ($\pm$ 12)	229 ($\pm$ 15)
	90^{th} p.	45 ($\pm$ 5)	65 ($\pm$ 10)	86 ($\pm$ 8)	132 ($\pm$ 12)	198 ($\pm$ 12)
	50^{th} p.	0.3 ($\pm$ 0.1)	1.5 ($\pm$ 1.3)	5 ($\pm$ 2)	23 ($\pm$ 4)	63 ($\pm$ 5)
Tropical Nights	95^{th} p.	211 ($\pm$ 11)	232 ($\pm$ 14)	253 ($\pm$ 13)	306 ($\pm$ 17)	358 ($\pm$ 3)
	90^{th} p.	280 ($\pm$ 7)	195 ($\pm$ 9)	205 ($\pm$ 9)	232 ($\pm$ 12)	277 ($\pm$ 14)
	50^{th} p.	15 ($\pm$ 4)	27 ($\pm$ 7)	41 ($\pm$ 6)	71 ($\pm$ 6)	102 ($\pm$ 4)

It is notable that, although there is a large spread between the ensemble members in each city (Figure 2.2), the spread in the clusters (Figure 2.6) and population-weighted metrics (Figure 2.7) is not as large. This emphasizes that the effect of unforced variability might be large at small scales but, as the region expands, the impact of unforced variability decreases. This is also found in Table 2.3, where in each case, the standard deviation between ensembles is less than 20% of the average, except in a few cases. This indicates that unforced variability will generally play a minor role in determining global exposure to temperature above thresholds, although different people may be affected in different realizations of unforced variability.

In addition, with 1.5°C of global warming, the lowest ensemble of the 90th percentile of HWD_{t2m}, HWD_{w2m}, and HWF_{t2m} exceeds the highest ensemble of the same metric in the current climate (red lines in Figure 2.7). With 2°C of warming, the minimum ensemble of $HWD_{t2m/w2m}$, $HWF_{t2m/w2m}$, HWM_{w2m}, and tropical nights exceed the maximum ensemble of the current climate, and with 2.5°C of warming, the minimum ensemble of all metrics exceeds the maximum ensemble of the same metric in the current climate. Thus, this model predicts that the occurrence of extremes will soon be able to exceed values likely possible in our present climate for these metrics.

2.4.3. Analysis on GDP per capita

It is well-known that not everyone is equally vulnerable to extreme weather, with rich, relatively more developed communities having more resources to deal with extreme events than poorer communities. In that context, global gridded GDP per capita is used to calculate average risk at each level of wealth. The ensemble-average result is depicted in Figure 2.8, which shows the absolute number of deadly days and tropical nights as well as the increase in number of deadly

days and tropical nights that each level of economic level experience relative to the reference period warming of 0.87°C. This plot assumes that the relative distribution of population and GDP remains fixed through time. Our sensitivity tests show that the model bias yields small differences in the results, with less than 5% difference in both the absolute number of extreme events as well as the changes in extremes.

For each level of warming, we find that the lower GDP regions will experience not only higher absolute numbers of extreme temperature days but also the largest increases. For deadly days, the increase is largest between 10^{th} to 40^{th} percentile of GDP, and for tropical nights, the increase is largest below the 30^{th} percentile of GDP. The regions that contribute the most for the low GDP percentiles are Southeast Asia, including Myanmar, Laos, and Cambodia, and Tropical Africa, including Republic of the Congo, Kenya, Uganda, Ethiopia, and Sudan, which are in clusters 1 and 2 in our cluster analysis (Figure 2.5). The maximum difference of heat wave days between the ensembles is less than 25% for all GDP and global warming levels.

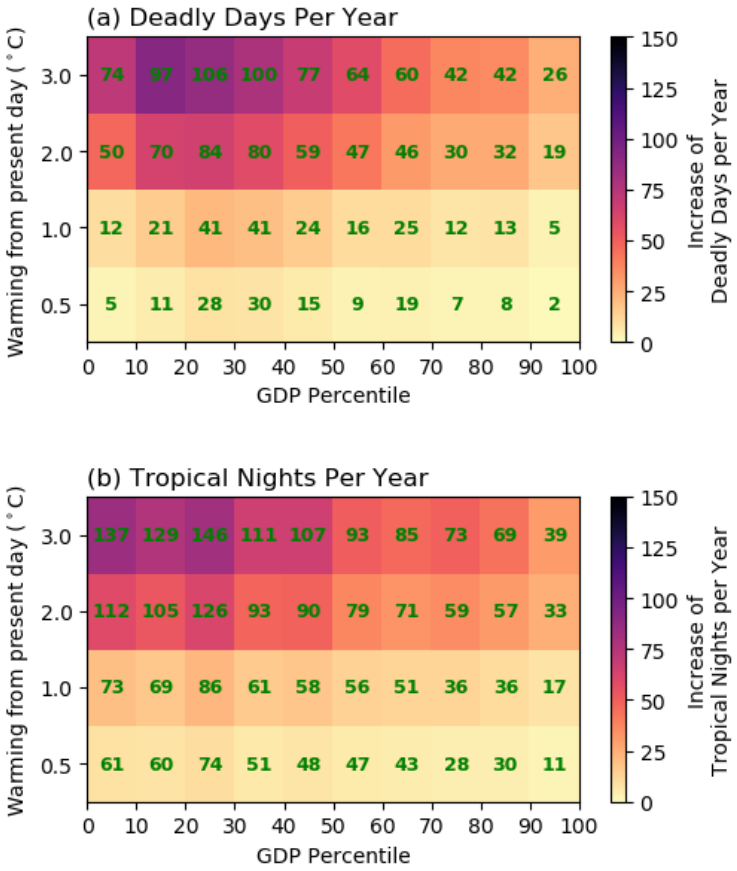

Figure 2.8. Increase in (a) deadly days and (b) tropical nights compared to the reference period (0.87°C warming), binned by percentile of GDP per capita at selected levels of warming compared to reference climate (calculated by subtracting reference values, shown as heatmap), averaged over the population within the GDP percentile (for example, averaged over population in 0~10 percentile of GDP), and over all ensemble members for 5-year window after each level of warming first occurs. Green text inside the heatmap represent the absolute number of deadly days and tropical nights in each level of warming.

2.4.4. Energy demand on large cities

Annual CDD and HDD have been calculated for the 15 cities in section 2.4.1. Both CDD and HDD are calculated by averaging the CDD and HDD values of 3×3 grid points surrounding each city, including only land grid points. CDD and HDD values are then averaged for 5 years after global warming reaches each levels of threshold. Fig. 2.9 shows the percent change of CDD and HDD at 1.5°C, 2.0°C, 3.0°C, and 4.0°C relative to the reference period CDD and HDD values. This was done for each city, and for each ensemble member. At 1.5°C, 2.0°C, 3.0°C, and 4.0°C warming, CDDs in the 15 cities increase by an average of 9%, 22%, 54% and 70%. Our sensitivity tests show that the application of the average model bias yields changes of less than 1% in these numbers. This suggests an enormous increase in energy required for cooling.

In contrast, average energy demand on cold days (HDD) decreases by 21%, 36%, 59%, and 65% in cities considered, compared to present day, partially offsetting the increase in energy required for cooling. Mania shows 0% change in HDD for all period, since Manila does not experience HDD days in present or future periods. Sensitivity tests also show less than a 1% difference in HDD change due to model biases.

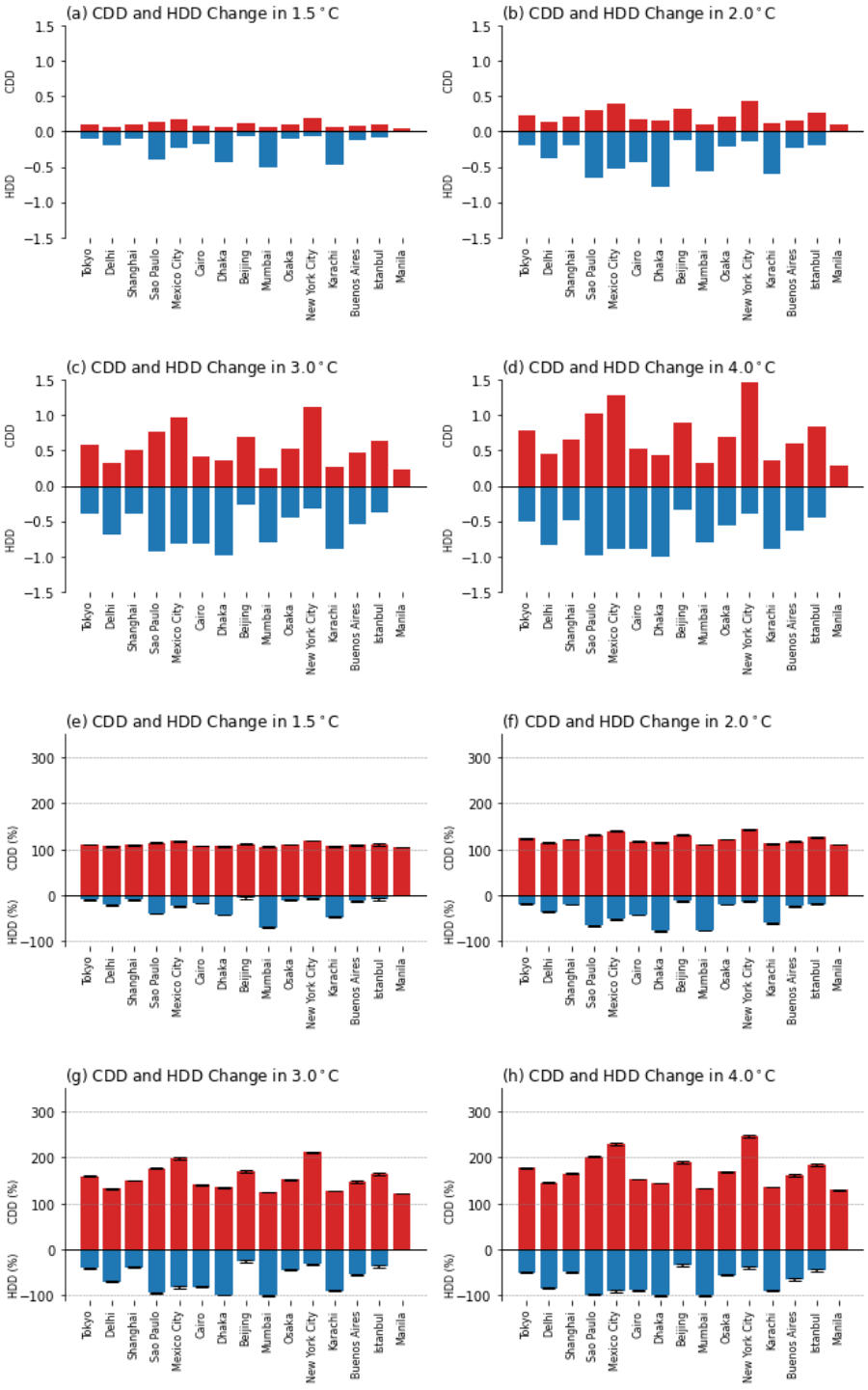
(a) CDD and HDD Change in 1.5 °C
(b) CDD and HDD Change in 2.0 °C
(c) CDD and HDD Change in 3.0 °C
(d) CDD and HDD Change in 4.0 °C
(e) CDD and HDD Change in 1.5 °C
(f) CDD and HDD Change in 2.0 °C
(g) CDD and HDD Change in 3.0 °C
(h) CDD and HDD Change in 4.0 °C
CDD
HDD
CDD (%)
HDD (%)
Tokyo
Delhi
Shanghai
Sao Paulo
Mexico City
Cairo
Dhaka
Beijing
Mumbai
Osaka
New York City
Karachi
Buenos Aires
Istanbul
Manila

Figure 2.9. (a-d) Change (absolute value) of ensemble averaged cooling degree days (CDD; red) and heating degree days (HDD; blue) compared to the reference climate (0.87°C) in the 1% CO_2 experiments at the time they reach the global mean temperature thresholds of (a) 1.5°C, (b) 2.0°C, (c) 3.0°C, and (d) 4.0°C, respectively. Error bars represent the standard deviation of CDD and HDD values between the ensemble members. (e-h) Same as (a-d), but for percent change.

2.5. Conclusion

In this study, we found that extreme heat events will become more frequent and severe in a warming world. We find that both forced and unforced variability play a key role in extreme heat events, highlighting the necessity of considering both contributions to extreme heat. We also look at population weighted, and GDP sorted statistics of extreme heat in warmer world.

Our results show that ENSO is the dominant mode of unforced variability impacting the occurrence of extreme heat and humidity events in the world's largest 15 cities. But while the impact of unforced variability might be significant regionally and temporarily, it becomes less important when one looks at larger aggregate regions.

Looking at global population-weighted statistics, we found that with 1.5°C of global average warming, over 10% of population will face heat waves of 45°C temperature, and 28°C wet bulb temperatures. And 5% of the population will face more than 105 days of deadly days and 232 tropical nights per year. With 3°C of warming, which we are currently on track for, 10% of the population will experience over 132 days of deadly days and over 232 days of tropical nights per year. And 10% of population will face 47°C temperature and 30°C wet bulb temperature. Given these two metrics have important implications for human mortality, such increases may have significant impact on human health globally.

Sorting heat and humidity events by wealth, we confirm that increasing frequency and severity of extreme events will fall mostly on the poorer people. To further investigate some economic impacts of increasing heat extremes, cooling degree days (CDD) and heating degree days (HDD) are calculated for the world's 15 largest cities. Energy demand for cooling (CDD) increases by average of 9% on 1.5°C and 54% on 3.0°C of warming, while energy demand for heating (HDD) decreases by 21% and 59%. Since CDD is known to have a piecewise linear relationship with the energy consumption, with slope increasing with higher CDD (De Rosa, Bianco, Scarpa, & Tagliafico, 2014; Shin & Do, 2016), increasing CDD in a warmer world could be one of the factors driving increased economic inequity from global warming related heat extremes, due to relative high cost and need for energy in poorest countries.

Uncertainties in this analysis include our use of gridded 6-hourly climate model output. More detailed analysis could be done with climate simulations with higher temporal and spatial resolution. The model has biases relative to measurements, potentially due to the fact that there are no aerosols in the forcing, which is another source of uncertainty. This was tested by adding the difference between the ensemble average and the reanalysis data to the model fields and recomputing the heat wave indices. In general, the impact of this bias was not important. In future analyses, this could be better resolved with use of multi-model ensembles or detailed bias-correction of the model.

Another uncertainty is that our runs are continuously warming, and it is possible that an equilibrium world at any given temperature may experience different occurrence of extremes than in the runs in this paper. Additionally, since an increasing proportion of the population is expected to live in dense metropolitan areas, there is also the possibility that actual heat and humidity extremes that populations experience could be more severe than the gridded data due to local

phenomena such as the urban heat island effect (Murata, Nakano, Kanada, Kurihara, & Sasaki, 2012). Statistical or dynamical downscaling could be used for a more detailed analysis (Dibike & Coulibaly, 2006; Wood, Leung, Sridhar, & Lettenmaier, 2004). Also, land models with capacity to decompose urban and rural environment could be applied in same context (Bonan et al., 2002; Dickinson et al., 2006). Also, this study could gain further insights by considering changing population and socioeconomic distribution in the future. Overall, however, none of these things are expected to change the broad conclusions of this study that global warming will lead to increased exposure to extremes in heat and humidity.

CHAPTER III

THE IMPACT OF NEGLECTING CLIMATE CHANGE AND VARIABILITY ON ERCOT'S FORECASTS OF ELECTRICITY DEMAND IN TEXAS[*]

3.1. Introduction

Most of the citizens of the State of Texas get electricity from a grid managed by the Electric Reliability Council of Texas (ERCOT). During February 2021, a significant winter storm (Doss-Gollin et al., 2021) caused widespread blackouts throughout the State that left more than 10 million people without electricity (Busby et al., 2021). These blackouts and their downstream impacts led to the deaths of hundreds of people and caused nearly $200B of damages (Frankenfield, 2021; Ivanova, 2021).

To maintain the reliability of the grid, ERCOT makes short-term seasonal power-demand assessments (e.g., https://www.ercot.com/files/docs/2020/11/05/SARA-FinalWinter2020-2021.pdf) to ensure adequate resources will be available. These assessments are based on the weather from the past decade and factors such as population, but they do not account for a changing climate or the likelihood of climate variability outside the very recent historical record. The impact of extreme temperatures due to climate change and extreme variability on power demand has been investigated in multiple studies and in different regions (Auffhammer, Baylis, & Hausman, 2017; Franco & Sanstad, 2008; Kim & Lee, 2019). In this paper, we evaluate ERCOT's methodology

[*] Reprinted with permission from "The Impact of Neglecting Climate Change and Variability on ERCOT's Forecasts of Electricity Demand in Texas" by Jangho Lee and Andrew E. Dessler, 2022. *Weather, Climate, and Society*, 14, 499-505, Copyright 2022 by Jangho Lee @ American Meteorological Society. Used with permission.

and develop a new method for incorporating more realistic predictions of future weather into energy projections for Texas.

3.2. The model ensemble and comparisons to historical temperature data

Our observational temperature data are daily-average 2-m air temperatures from the ECMWF ERA5 reanalysis (Hersbach et al., 2020), which has a resolution of 0.25° for both latitude and longitude and hourly temporal resolution. Average daily temperature for ERA5 is calculated by averaging the hourly temperatures in a day. While the reanalysis might produce a smoother temperature field than reality, our analysis uses Texas-average temperature, and this large-scale average should be insensitive to smoothing of the temperature field.

We also use temperatures from an ensemble of 39 model runs known as the Community Earth System Model Large Ensemble (CESM-LE) (Jennifer E Kay et al., 2015), which has a resolution of 0.94° × 1.25° for latitude and longitude. CESM-LE only has daily average values of temperature, and we take these values from 1981 to 2021 for historical analysis and to 2025 for future analysis. The members of this ensemble use an identical climate model and the same evolution of historical natural and anthropogenic forcing. The members differ only in their initial conditions, so the variation in climate across the ensemble is entirely due to random climate and weather variability.

To estimate the temperature of Texas, we average the grid points whose centers are within the state border of Texas. We find a difference of 0.7°C and 0.6°C in the June-July-August (JJA) and December-January-February seasons (DJF) between the ensemble average and the ERA5 over the last 40 years. Such a bias is not surprising since the climate model is not tuned to simulate the absolute temperature of the Earth. This bias is small compared to the magnitude of the temperature

variations we are analyzing, but we nonetheless adjust for it by adding the offset to each grid point and time step of the model fields so to bring the average values into agreement.

Figure 3.1 shows the highest 1-day and 5-day average temperature during each JJA and lowest 1-day and 5-day average temperature during each DJF since 1981 in the ECMWF ERA5 reanalysis and bias-corrected CESM-LE. The convention in this paper is that DJF refers to three consecutive months; for example, DJF 2010 is Dec. 2009 and Jan. and Feb. 2010. For the JJA maximum, the highest 5-day average temperature was in 2011 (32.9°C) while the highest 1-day temperature (33.1°C) was in 2020. For the DJF minimum, the coldest 5-day (-6.3°C) and 1-day average temperature (-11.1°C) were both in 2021.

We note that that focus of this paper is on the temperature extremes, and we see no evidence of larger biases in the tails of the distributions. Fitting the ERA5 and CESM-LE data to a generalized extreme value (GEV) distribution tells us that the 2020 1-day temperature of 33.1°C was a 1-in-7 year event in the ERA5, while it was a 1-in-5 year event in CESM-LE. The 2021 winter 1-day temperature of -11.1°C was a 1-in-55 year event in the ERA5, while it was a 1-in-87 year event in the CESM-LE. The standard deviation of ERA5 data is 2.0°C and 4.9°C in JJA and DJF, while the average of standard deviation in each member of CESM-LE is 1.8 (1σ of ensemble standard deviation values is 0.22) and 4.0 (1σ=0.58). Based on these comparisons, we feel confident we can use this ensemble to evaluate ERCOT's forecasts.

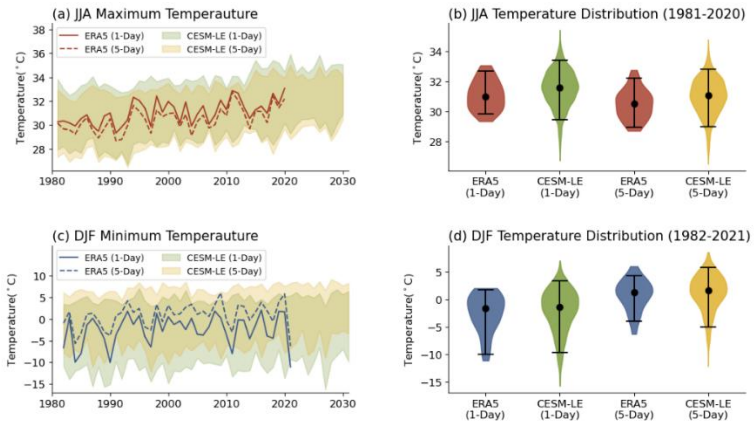

Figure 3.1. Time series of seasonal maximum and minimum temperature over Texas (not population weighted). (a) JJA maximum 1-day (solid line) temperature and 5-day (dashed line) temperature in ERA5, and green and yellow area each denotes the maximum and minimum ensemble member of 1-day and 5-day temperature in CESM-LE. (b) Violin plot for distribution of 1-day and 5-day JJA maximum temperature in ERA5 and CESM-LE. Error bars represent the 95th and 5th percentile of the distribution, and the dots represent the median of the distribution. (c, d) Same as (a, b), but for DJF minimum temperature.

3.3. The connection between electricity consumption and temperature in the historical record

Historical hourly electric power consumption is obtained from ERCOT for the period Jan. 1996-Feb. 2021 (http://www.ercot.com/gridinfo/load/load_hist/). 2001 data are not available, so our analysis excludes DJF 2001, JJA 2001, and DJF 2002. The first step is to regress population-weighted daily average temperature against daily average power. We use the population distribution averaged from 2000 to 2020 from CIESIN (2016) for the population weighting. We

use time-invariant population distribution since we found there are negligible changes in the population distribution over this period

We perform the regression separately for each season of each year. Figs. 3.2a and 3.3a show a tight relationship between temperature and power usage in JJA and DJF for the first and last year of ERCOT's record — other years (not shown) show similarly tight relationships. This indicates that, within a season, variations in temperature are the primary controlling factor for power usage.

Based on our examination of the data, we use a linear fit for JJA and a non-linear polynomial fit ($P = C_0 + C_1 T + C_2\, T^{1.75}$) for DJF. Previous studies also discussed power usage increasing with higher temperature in summer and colder temperature in winter (Auffhammer et al., 2017; Craig, Jaramillo, Hodge, Nijssen, & Brancucci, 2020; Franco & Sanstad, 2008; Mirasgedis et al., 2007; Murphy, Sowell, & Apt, 2019; Psiloglou, Giannakopoulos, Majithia, & Petrakis, 2009). This was done by using everything from a simple linear and piecewise-linear fit (Almuhtady, Alshwawra, Alfaouri, Al-Kouz, & Al-Hinti, 2019; Guan, Beecham, Xu, & Ingleton, 2017; Guan et al., 2014; Ihara, Genchi, Sato, Yamaguchi, & Endo, 2008) to complex regressions up to 5th degree fit (Jovanović et al. 2015). In Section 1 of the supplement, we discuss this in detail how we arrive at the form of our fit.

From each year's fit, we calculate P_{ref} for that year, which is power usage at a reference temperature (T_{ref}). We use a reference temperature equal to the median temperature for JJA (28.8°C) and DJF (10.9°C). The time series of P_{ref} is plotted in Figs. 3.2b and 3.3b; this can be thought of as the seasonal average power usage that would have occurred if the temperature were fixed at the reference temperature. The increase in P_{ref} over time is due to changes in non-climate

factors, such as population. We then perform a linear fit to represent P_{ref} as a function of year ($P_{ref}(y)$) (coefficients for all of the fits can be found in Supplement Section 2).

We expect the coefficients from each year's temperature-power regressions (Fig. 3.2a and 3.3a) to be correlated with P_{ref}. For example, increases in population will change the slope of the power-temperature relation because, as population increases, changes in temperature will drive larger changes in power usage. Figs. 3.2c, 3.3c, and 3.3d show that these coefficients are indeed correlated with P_{ref}.

Given this, we can model daily average power usage at as a function of year and daily average temperature T. For JJA:

$$P_{JJA}(y,T) = P_{ref}(y) + \left(S(y) \times (T - T_{ref})\right) \quad (1)$$

Where $P_{JJA}(y,T)$ is the daily average power for a day in year y with a population-weighted, daily average temperature T. $P_{ref}(y)$ is the value of P_{ref} during JJA in year y, $S(y)$ is the slope of the power-temperature regression in year y, and T_{ref} is the JJA reference temperature. Note that S was plotted in Fig. 2c as a function of P_{ref}, but because P_{ref} is a function of year, we can also express S as a function of year y.

Our equation for DJF is similar to the JJA equation except that the power-temperature relation has higher order terms:

$$P_{DJF}(y,T) = P_{ref}(y) + \left(C_1(y) \times (T - T_{ref})\right) + \left(C_2(y) \times (T - T_{ref})^{1.75}\right) \quad (2)$$

As with the JJA relation, the coefficients C_1 and C_2 correlate with P_{ref} (Figs. 3c and 3d), so we can also express them as functions of year. Also remember that DJF P_{ref} and T_{ref} are different from JJA P_{ref} and T_{ref}.

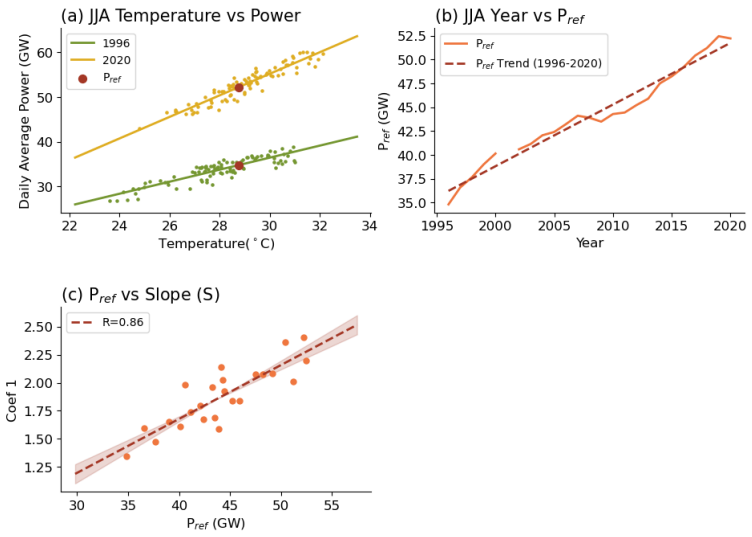

Figure 3.2. (a) Scatterplot of population-weighted daily average temperature and JJA daily average power usage in the first and last year of ERCOT's historical record. Red circle denotes the power at the reference temperature (P_{ref}). (b) Evolution of P_{ref} over time. The red dashed line is a linear trend. (c) Slope of the temperature-power relation as a function of P_{ref}. Each point represents a value from a single year. Shaded area represents the standard error of the linear fit.

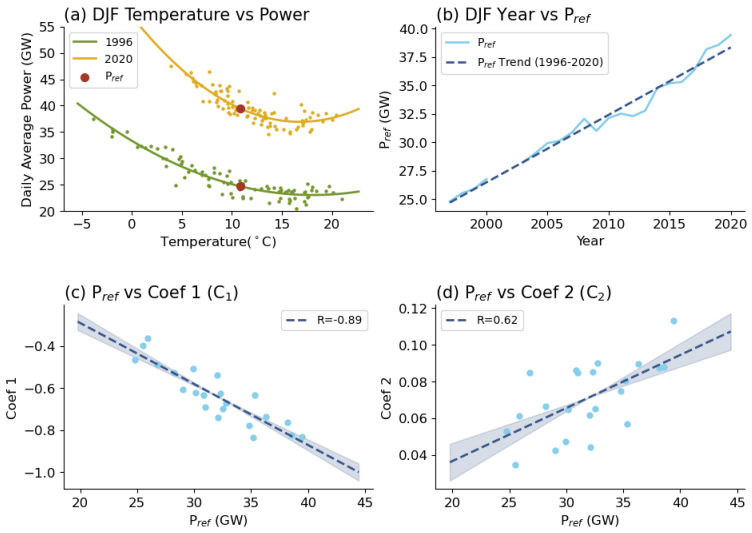

Figure 3.3. Same as Figure 3.2, but for DJF. Because we use a 1.75-D power-temperature fit in DJF, we have two constants, and these are plotted in panels c and d.

3.4. Prediction of future electricity consumption

Using the methodology described in the last section, we can produce an estimate of daily average power usage using the coefficient estimates from the parametric fits. For comparison to ERCOT forecasts, we convert this to daily *maximum* power (hereafter DMP), the highest hourly power demand during the day, using a linear regression between daily maximum and daily average power usage developed from the historical data. The correlation between these quantities has R values of 0.99 and 0.98 in JJA and DJF and an RMS error of 1.0 and 1.1 GW, respectively.

Plugging ERA5 temperatures into Eq. 1 and 2, we can reproduce the historical seasonal maximum power (the highest hourly power demand during the season, hereafter SMP) quite closely (Figs. 3.4a and 3.4b), with RMS differences of 1.0 GW and 1.5 GW for JJA and DJF, respectively (2021 is excluded from the DJF calculation due to the blackout). This good agreement may be surprising because we left out factors that one might have anticipated would be important (e.g., weekday vs. weekend). We investigated these factors and found that none of them significantly improved our ability to reproduce the observations (Supplement Section 3). We note that this is true when averaging of a large area like the state of Texas, but other factors may be important at smaller scales, such as a county or neighborhood.

We also have taken the CESM-LE temperatures and used Eq. 1 and 2 to estimate SMP for the 1996-2021 period. The shaded regions show the range of power predicted by the ensemble and ERCOT's historical power demand falls comfortably within the ensemble's envelope. This result

is consistent with the fact that observed temperatures over this period fall within the CESM-LE's range of predicted temperatures (Fig. 3.1).

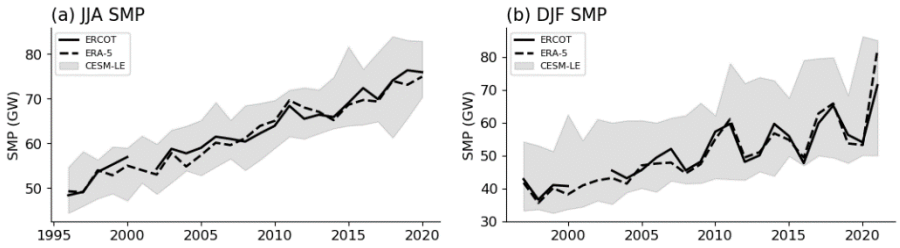

Figure 3.4. Time series of seasonal maximum hourly power usage (SMP). (a) JJA SMP for 1996-2020. Black solid line represents the historical ERCOT record, and black dashed line represent the historical power usage estimated by us using ERA5 temperatures. The grey area depicts the range of power usage estimated from the CESM-LE. (b) Same as panel (a), but for DJF 1997-2021.

3.5. Comparison of seasonal power demand

3.5.1. Summer power demand

In order to evaluate ERCOT's seasonal 2021 summer resources assessment (https://www.ercot.com/files/docs/2021/05/06/SARA-FinalSummer2021.pdf), we have calculated a probability distribution of SMP for JJA 2021 using temperatures from the CESM-LE from the period 2016-2025, but with 2021's P_{ref} (Fig. 3.5a).

ERCOT predicted a most likely SMP of 77 GW, in good agreement with the peak of our probability distribution. ERCOT also predicted an extreme peak-load scenario of 80 GW, which they derived assuming that the worst-case scenario is a repeat JJA 2011 temperatures. Note that ERCOT publicly provides no probabilistic information with which to interpret their extreme scenarios, although in an email they told us that it should be exceeded in 10% of the years (Jeff

Billo, personal communication, 2021). We calculate that there was a 17% chance of JJA 2021 SMP exceeding 80 GW (Fig. 3.5a), suggesting that the use of limited historical temperatures may lead to an underestimate of the occurrence of extreme demand.

ERCOT also estimated a best-case of 87 GW of power available to satisfy peak demand. Comparing this to Fig. 3.5a shows that the ERCOT grid is running with very little margin, with 5% of the summers in the CESM-LE having an SMP within 4.3 GW of ERCOT's estimate of best-case available power and 20% of summers within 7.1 GW. In such a situation, minor but unanticipated declines in available power, such as what happens when several power plants go offline due to forced outages (Craig et al., 2020; Murphy et al., 2019), puts the ERCOT grid at risk of being unable to satisfy power demand.

3.5.2. Comparison of winter power demand

We now evaluate ERCOT's seasonal resource assessment made right before the DJF 2021 season (https://www.ercot.com/files/docs/2020/11/05/SARA-FinalWinter2020-2021.pdf). We do that by comparing it to a probability distribution of SMP for DJF 2021 that we calculated using temperatures in the CESM-LE between 2016 and 2025, but with 2021's P_{ref} (Fig. 3.5b). ERCOT's most-likely SMP is 57 GW, very close to the peak of our predicted distribution. ERCOT's extreme peak load scenario is 67 GW, calculated assuming that the worst case was that Texas would experience temperatures as cold as DJF 2011's, the most recent very cold Texas winter.

Like their summer estimates, this extreme peak load scenario is low — we estimate that there was an 19% chance that SMP would exceed this value. Reality provided support for this: 2021 DJF minimum daily average population-weighted temperatures were 3.4°C colder than

2011's, from which we estimate that peak demand was 82 GW — about 15 GW above ERCOT's worst-case prediction.

ERCOT communicated to us that their estimate of DMP during the 2021 winter storm was 76 GW (Jeff Billo, personal communication, 2021), 6 GW lower than our estimate. We do not know how ERCOT comes up with their number, and without more information about ERCOT's methodology, we cannot identify the source of the disagreement. This difference has important implications for how much margin the ERCOT grid has. ERCOT estimates that, in the best case, there was 83 GW of power available. If our estimate is correct, then the ERCOT grid had essentially no margin in DJF 2021, so that any loss of power, e.g., due to lack of weatherization of energy infrastructure, meant that the ERCOT grid could not satisfy power demand.

More generally, Fig. 3.5b shows that the ERCOT grid also runs with very little margin in winter, just as it does in summer. For DJF 2021, we estimate that 5% of winters in the CESM-LE had an SMP within 7.9 GW of ERCOT's best-case estimate of available power and 10% and 20% of winters were within 12 and 17 GW, respectively. And 1.5% of the winters had SMP in 2021 DJF exceeding best-case available power, as apparently happened in 2021.

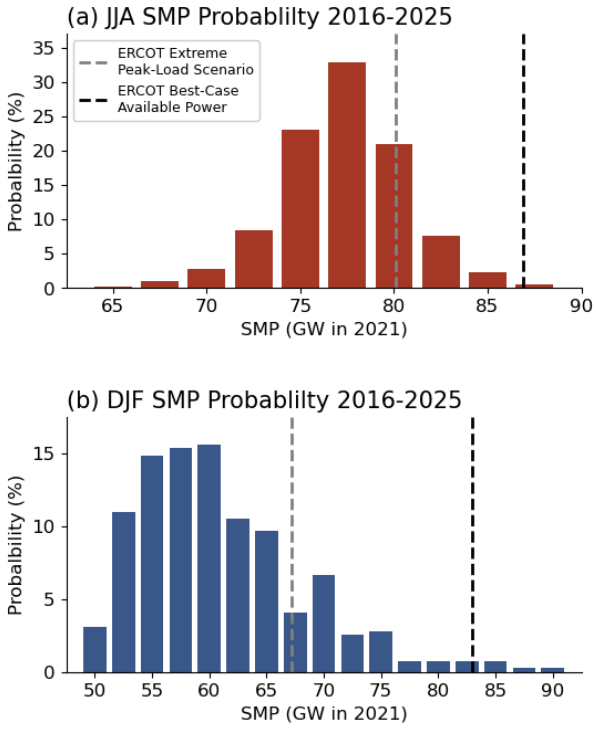

Figure 3.5. Probability distribution of seasonal hourly maximum power usage (SMP) in (a) JJA 2021 and (b) DJF 2021, predicted by the CESM-LE. Calculations use temperatures from 2016-2025 and P_{ref} for 2021. Grey and black vertical lines represent the ERCOT's seasonal forecast for extreme peak-load and best-case available power.

3.6. Conclusions

One of ERCOT's most important jobs is ensuring that there is sufficient power available to the Texas electrical grid. In support of this objective, ERCOT makes seasonal assessments of future power demand. However, ERCOT does not use modern climate forecasting tools to estimate climate variability when making these forecasts. Instead, they exclusively use the recent historical climate record.

In this paper, we describe an empirical methodology to estimate the impacts of weather variability on power demand. We then use output from an ensemble of climate model runs (the CESM-LE) to estimate the impact of climate variability on ERCOT's forecasts. We find that ERCOT's exclusive use of historical temperatures means that they underestimate the worst-case scenarios. In 2021, we estimate a 17% and 19% chance that Texas temperature could have caused the power demand to exceed ERCOT's extreme peak load scenarios, respectively. After the fact, we find that 2021 DJF maximum power demand exceeded ERCOT's extreme peak load scenario by 15 GW or 22%.

JJA in 2021 was not unusually hot in Texas. Maximum load in JJA 2021 was 74 GW, which is lower than ERCOT's extreme peak-load scenario (80 GW). The CESM-LE tells us that JJA 2021 was at the lower end in the distribution of possible summertime temperatures. There was 88 % chance that summer with higher temperature would have happened, and 17 % chance that it would have exceeded ERCOT's extreme peak-load scenario.

ERCOT disputes our estimate of peak demand during the 2021 DJF (82 GW) — they estimate demand was 76 GW. Resolution of this difference is important because it has implications for how robust the ERCOT grid is when power plants unexpectedly go offline, but ERCOT's model and underlying data are not publicly available so we are unable to identify the source of this disagreement. ERCOT should be transparent about their forecasts and should make their forecast model public so researchers can better evaluate their methodology.

In both summer and winter, we find that ERCOT's electricity grid has little spare capacity. According to ERCOT, best-case power available in 2021 is in the mid-80s GW. We find that power demand can get close to that limit in both summer and winter. That means that unforeseen

problems that reduce supply even slightly below the best case can lead to the power grid being unable to satisfy power demand.

Finally, we encourage ERCOT to make probabilistic forecasts of temperature using modern tools, like climate model ensembles. ERCOT's insistence on using a relatively short historical record means they are underestimating climate variability, leading to underestimates of the most extreme power demand forecasts. Using a longer historical record would be a poor solution since it would ignore the fact that the climate is changing.

3.7. Supplementary Materials for Chapter 3

3.7.1. Selection of temperature-power relationship

As discussed in the main text, there are several approaches to model the relationship between temperature and power. Linear (Guan et al., 2017; Guan et al., 2014), piecewise fits (Almuhtady et al., 2019; Ihara et al., 2008), and polynomial regressions with up to 5th order (Jovanović, Savić, Bojić, Djordjević, & Nikolić, 2015) have been used in previous studies. Previous work has also used cooling and heating degree-days instead of temperature (Mirasgedis et al., 2007; Psiloglou et al., 2009). Here we show the sensitivity of model selection and describe the best performing model.

3.7.1.1. Model for DJF

We tested a piecewise-linear fit — where the slope changes at 10°C— and a set of non-linear polynomials ($P = C_0 + C_1 T + C_2\, T^x$ where x = 1.25, 1.5, 1.75, and 2). Because using degree-days is equivalent to a linear fit of temperature over (or below) a certain threshold, this shows similar results to the piecewise fit. After fitting the data using all these models, we calculated

each model's mean and RMS error as a function of temperature. These values are then divided by average power usage of each season of the year to account for overall increase of power usage (see Fig. 3 in main text), which yields a relative error.

The results are shown in Fig. 3.6 for piecewise linear and x = 1.75 and 2. All of the models tested show similar performance between 3°C to 18°C. However, at very cold temperatures, below -3°C, the x = 2 model tends to overpredict the power while piecewise-linear fit underpredicts power. The x = 1.75 model shows the best performance in terms of relative error.

Because of this, we have used the x = 1.75 fit in the paper. The choice of model really only matters at the coldest temperatures, such as DJF 2021. Previous studies also examined the empirical relationship between temperature and daily electricity usage (Auffhammer et al., 2017; Franco & Sanstad, 2008) and reported a non-linear relationship between temperature and electricity usage at cold temperatures.

3.7.1.2. Model for JJA

Summertime temperature is consistently hot in Texas (see Fig. 1 and 2 in the main text), meaning that the difference between the hottest and coolest summer is small. As a result of the relatively small range of temperatures, the temperature-power relationship in JJA is well described by a linear relation. We tested non-linear fits and found they did no better than a linear model.

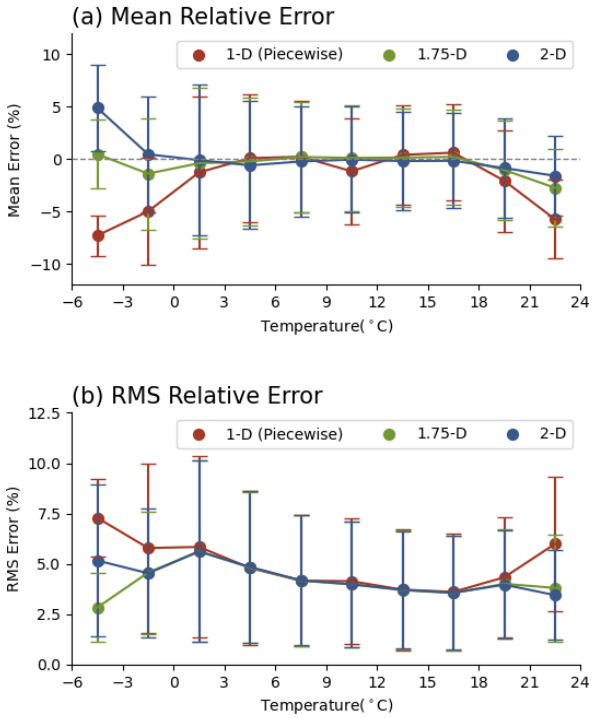

Figure 3.6. (a) Mean relative error and (b) RMS relative error for 1-D, 1.75-D, and 2-D fit of temperature-power relationship. Relative errors are averaged for every 3°C bins of temperature. The dots represent the mean error in each temperature bins, while the error bars represent the standard deviation of errors in each temperature bins.

3.7.2. Description of temperature-power relationship

As discussed in the main text, our model for estimating daily average power usage (DAP) from the daily average temperature are given as follows:

$$P_{JJA}(y,T) = P_{ref}(y) + \left(S(y) \times (T - T_{ref})\right) \quad (S1)$$

$$P_{DJF}(y,T) = P_{ref}(y) + \left(C_1(y) \times (T - T_{ref})\right) + \left(C_2(y) \times (T - T_{ref})^{1.75}\right) \quad (S2)$$

Where y indicates year and T denotes temperature (°C). In this section, we provide the coefficients of this fit.

(1) Coefficients for JJA (Eq. S1)

a. $P_{ref}\,(y) = (y \times 0.6470) - 1255.2777$

b. $S(y) = (P_{ref}\,(y) \times 0.0480) - 0.2424$

(2) Coefficients for DJF (Eq. S2)

a. $P_{ref}\,(y) = (y \times 0.5942) - 1162.0179$

b. $C_1(y) = \left(P_{ref}\,(y) \times -0.0291\right) + 0.2907$

c. $C_2(y) = \left(P_{ref}\,(y) \times 0.0029\right) - 0.0213$

With historical hourly power load data from ERCOT, we are able to calculate the linear relationship between daily average power usage (DAP) and daily maximum power usage (DMP). The equations for JJA and DJF are:

$$DMP_{JJA} = DAP_{JJA} \times 1.1290 - 2.0849 \quad (S3)$$

$$DMP_{DJF} = DAP_{DJF} \times 1.1247 + 0.7091 \quad (S4)$$

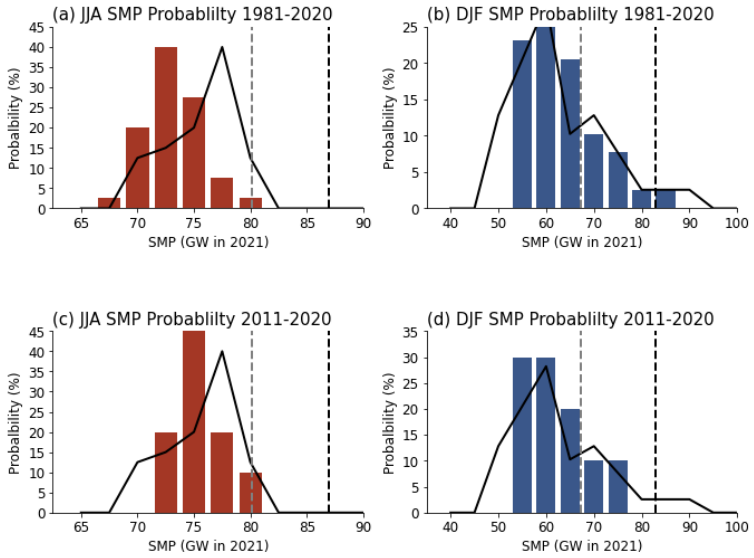

Figure 3.7. (a) Probability distribution of SMP probability in JJA, using the last 40 years of ERA-5 data. (b) Same as (a), but for DJF. (c, d) same as (a, b), but for the last 10-years of record. Grey and black dashed lines show the ERCOT's estimate of extreme peak-load scenario and best-case available power. Black solid line represents the values from in Fig. 5 in the main text (derived from the CESM-LE temperatures).

3.7.3. Sensitivity on including weekend effect

As discussed in the main text, we tested the sensitivity of our model by including other factors that are expected to impact the power usage other than daily average temperature. In this section, we include weekend effect and see how it changes our result.

To include the weekend effect, we estimate two different model for each season (JJA and DJF), one for weekdays and the other for weekends. We follow the same procedure described in the main text and supplementary section 2 but using only weekday or weekend data. After coming up with models for weekdays and weekends, we then compare those with the original model used in the main text.

When comparing with historical daily ERCOT load data, average of RMS error for each year of the original model is 3.05 (1σ=0.56) % and 4.01 (0.42) % for JJA and DJF. The combined weekday/weekend models yield RMS errors of 2.97 (0.58) % and 3.91 (0.41) % for JJA and DJF.

There is less than 0.1% increase of performance when adding weekend effect to our current model. Adding weekend effect will increase the sensitivity of our model due to smaller sample size and also add complexity, while it only adds very small amount of predictability. So, we decided not to add the weekend effect in our analysis.

3.7.4. Advantages of using CESM-LE

Figure 3.7 shows a plot similar to Fig. 3.5 in the main text, but with ERA-5 data with last 40 years (Fig S2a, S2b) and last 10 years (Fig 3.7.c, 3.7.d) of the historical record instead of CESM-LE temperatures.

In JJA, the PDFs using ERA5 temperatures are shifted to lower values (by a few GW) compared to those in Fig. 3.5 in the main text (shown in Fig 3.7 as the solid black line), almost certainly due to climate change that has occurred over this period.

In DJF, the main peak of the PDF is quite similar, reflecting the fact that typical temperatures are frequently near the flat part of the power-temperature relation, so slight global warming will not have much of an effect. It's at unusually cold temperatures where we would expect to see an impact (if one exists), but it's hard to determine since the historical record does not really have enough cold events to fill out the tail. Nevertheless, we see nothing in the PDFs using ERA5 temperatures that contradicts the results using the CESM-LE temperatures.

CHAPTER IV

FUTURE TEMPERATURE RELATED DEATHS IN THE U.S.: THE IMPACT OF CLIMATE CHANGE, DEMOGRAPHICS, AND ADAPTATION

4.1. Introduction

The relationship between temperature and human mortality has been the subject of many previous studies (Berko, 2014; Bobb, Peng, Bell, & Dominici, 2014; Demoury, Aerts, Vandeninden, Van Schaeybroeck, & De Clercq, 2022; Dimitrova et al., 2021; Gasparrini & Armstrong, 2011; Gasparrini, Guo, Hashizume, Lavigne, et al., 2015; Guo, Barnett, Pan, Yu, & Tong, 2011; Kalkstein & Greene, 1997; Ma et al., 2015; Yi & Chan, 2015; Y. Zhang et al., 2016). Previous studies have projected future temperature-related mortality covering different regions, such as global major cities (Gasparrini et al., 2017; Takahashi, Honda, & Emori, 2007; Vicedo-Cabrera et al., 2018), the U.S. (Anderson, Oleson, Jones, & Peng, 2018; A. I. Barreca, 2012; Jackson et al., 2010; Knowlton et al., 2007; Lo et al., 2019; Petkova et al., 2017; Wang, Shi, Zanobetti, & Schwartz, 2016; Weinberger et al., 2017), cities in Europe (Hajat, Vardoulakis, Heaviside, & Eggen, 2014; Martínez-Solanas et al., 2021; Muthers, Matzarakis, & Koch, 2010), or Asia (J. Y. Lee & Kim, 2016; Yang et al., 2021). Using historical data sets, previous studies have found that temperature and mortality show a V-shaped curve, where mortality increases as temperatures become very hot or very cold (Berko, 2014; de Schrijver et al., 2022; Dimitrova et al., 2021; Gosling, McGregor, & Lowe, 2009; Vardoulakis et al., 2014). Thus, we expect climate change to influence temperature-related mortality.

Another issue we explore in this paper is the impact of demographics. Older populations are known to be more vulnerable to temperatures extremes (Anderson et al., 2018; Åström,

Forsberg, Edvinsson, & Rocklöv, 2013; Barnett, 2007; Bobb et al., 2014; de Schrijver et al., 2022; Hintz, Luederitz, Lang, & von Wehrden, 2018; J. Y. Lee & Kim, 2016; Lin, Ho, & Wang, 2011; Yi & Chan, 2015; Y. Zhang et al., 2016), and since population is projected to both age and grow globally, the compound effect of demographic and population changes will increase temperature-related mortality (Li et al., 2016; Marsha, Sain, Heaton, Monaghan, & Wilhelmi, 2018). Previous studies included demographic and population change in their projection (Deschenes & Moretti, 2009; Deschênes & Greenstone, 2011; Hajat et al., 2014; Jenkins et al., 2014; J. Y. Lee & Kim, 2016; Li et al., 2016; Petkova et al., 2017; Vardoulakis et al., 2014), mostly using population projections from shared socioeconomic pathways (SSPs) (Hauer, 2019).

It is also clear that people will take actions to head off the impacts of extreme temperatures (A. Barreca, Clay, Deschenes, Greenstone, & Shapiro, 2016; Carson, Hajat, Armstrong, & Wilkinson, 2006; Davis, Knappenberger, Michaels, & Novicoff, 2003; Folkerts et al., 2020; Fouillet et al., 2008; Gasparrini, Guo, Hashizume, Kinney, et al., 2015; Kyselý & Plavcová, 2012). However, such adaptation takes resources, which many people do not have, so how well this can be done is an uncertainty that any analysis of future temperature-related mortality must address. There are few ways to incorporate adaptation to the future projections. Previous studies simply shifted the temperature-mortality relationship to warmer temperatures (Folkerts et al., 2020; Gosling et al., 2009; Jenkins et al., 2014), extrapolated the historical trends of temperature-mortality relationship (Muthers et al., 2010; Petkova et al., 2017), or adjusted the slope of temperature-mortality relationship (Jenkins et al., 2014). Here we use an "analog city" approach (Heutel, Miller, & Molitor, 2021; Kalkstein & Greene, 1997; Knowlton et al., 2007), where the mortality model for a city with warmer climate is applied to cooler city in a warming climate. For example, in Knowlton et al. (2007), they assumed that New York in the 2050s will have similar

temperature-mortality relationship as Washington and Atlanta in 1973-1994, since temperatures in New York in 2050s are similar to temperatures in Washington and Atlanta in 1973-1994.

In this paper, we consider all three of the factors that will impact future temperature-related mortality: climate change, population and demographics change, and adaptation, in order to determine how important each factor is.

4.2. Temperature-Mortality Relationship

Mortality data from the National Morbidity Mortality Air Pollution Study (NMMAPS) (Samet et al., 2000) contain the number of daily non-accidental deaths, stratified by age group (<65, 65-75, >75). We aggregate the two younger age groups to create a single category for ages <75. Data are collected from 106 large U.S. cities (Fig. 4.1a) and cover the period from 1987 to 2000. Population data are also included in NMMAPS, which come from the National Center for Health Statistics (NCHS). These 106 cities contain 65% of the population in the US.

Historical hourly 2-m air temperatures from ERA-5 Land reanalysis (Muñoz-Sabater et al., 2021) are averaged to obtain daily average temperatures. The data have a horizontal resolution of 0.1°×0.1° and the average of the 9 grid points nearest to the center of each city are used to represent the daily average temperature of the city.

Following the framework of Gasparrini, Guo, Hashizume, Kinney, et al. (2015) and Gasparrini, Guo, Hashizume, Lavigne, et al. (2015), we use a Distributed Lag Non-Linear Model (DLNM) to describe the association between temperature and mortality. We model the daily number of deaths as a function of daily average temperature separately for each city and age group (under/over 75). An important advantage of the DLNM is that it can capture the lagged effect of temperature, where consecutive extreme days results in higher risk compared to single-day event

(Gasparrini & Armstrong, 2011; Wang et al., 2016). Previous studies reported that the impact of a hot day can extend for up to 3 days, while the impact of a cold day could extend 21 days (Demoury et al., 2022; Dimitrova et al., 2021). Therefore, we include lags of up to 21 days in the DLNM model. We also include the day of week to account for the weekly cycle, day of year for the annual cycle, and year for the long-term trend. A detailed explanation of the DLNM model used in this study can be found in section 1 of the supplement.

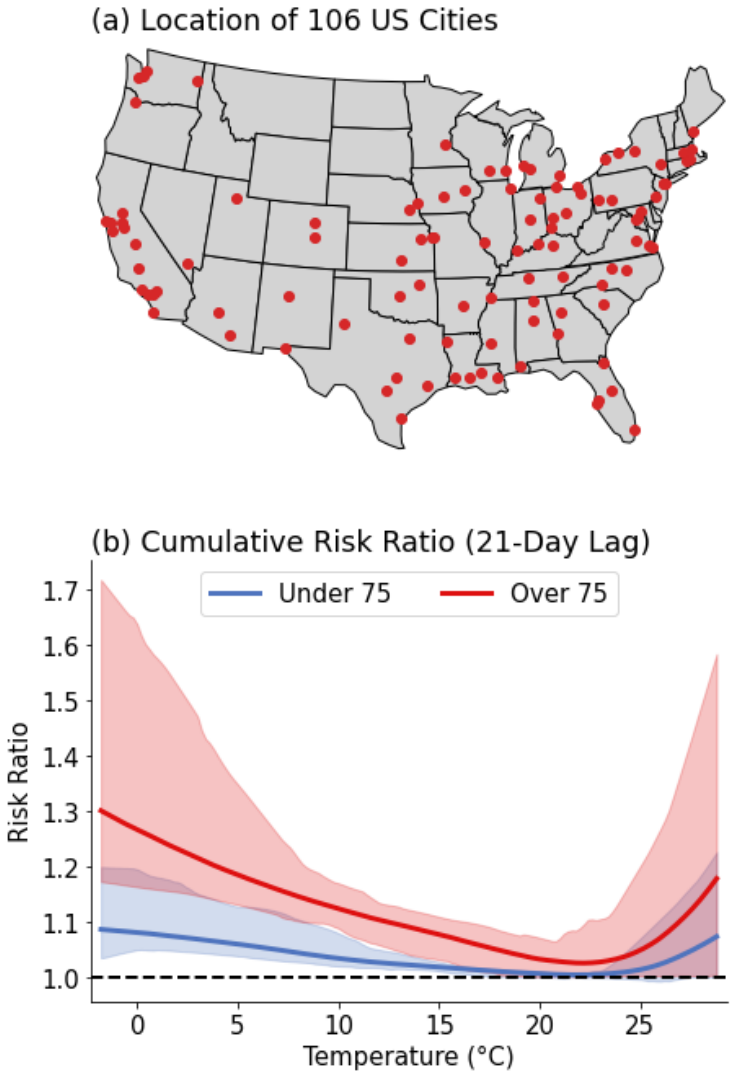

Figure 4.1. (a) Location of 106 cities used in this study. (b) Risk ratio (RR) of under/over 75 age groups, averaged for all cities in this study. Shaded regions show the 5th percentile to 95th percentile

range of RR curve for all cities. RR is the number of deaths at each temperature divided by the number of deaths at the curve's minimum (the MMT), around 22°C.

4.3. Historical Temperature-Related Mortality

Fig. 4.1b summarizes the mortality risk as a function of temperature, averaged over all cities (curves for individual cities can be found in Fig. S1). The quantity plotted here, the cumulative relative risk (RR), is the number of deaths at each temperature divided by the number of deaths at the minimum mortality temperature (MMT), after summing the RR at each lag, up to 21 days. Our curve is similar to those found in previous work (Gasparrini, Guo, Hashizume, Kinney, et al., 2015; Gasparrini, Guo, Hashizume, Lavigne, et al., 2015; Gasparrini et al., 2017; Guo et al., 2011; Lin et al., 2011; Ma et al., 2015; Yi & Chan, 2015; Y. Zhang et al., 2016).

With the regression models for each city and age group, we calculate the number of temperature-related excess deaths in the NMMAPS data in two steps. First, we define baseline deaths, which is the number of deaths at the MMT, calculated by averaging the number of deaths at temperatures around MMT (±0.5°C). With this baseline death value, we then calculate the number of deaths in each city using observed temperatures and the mortality-temperature curves.

There are an average of 36,444 temperature-related deaths per year between 1987-2000 (solid line in Fig. 4.2a). There is a clear trend over this period, and we can remove the effect of population changes by dividing the number of excess deaths by the population in each year, and then multiplying by the average population over the period. Doing this removes most of the trend (dashed line in Fig. 4.2a).

We can separate temperature-related deaths occurring above and below MMT, which by convention we refer to as heat- and cold-related deaths. We estimate there are an average of 4,819

heat-related deaths per year and 31,625 cold-related deaths. This is consistent with previous work that also found that most of the deaths were due to cold, rather than heat (Vardoulakis et al., 2014). We also found that 75.3% of deaths are from older (over 75) age groups (1 standard deviation of inter-city variance = 6.2%). The older age group is responsible for 75.6% (1σ=4.6%) and 75.1% (1σ=6.9%) of the heat- and cold-related mortality, respectively, despite being only 5.1% (1σ=1.3%) of the population. This point will be important later in the paper.

While 86% of temperature-related deaths are cold-related mortality, most of the deaths categorized as "cold-related" occur at temperatures only slightly below the MMT (typically around 22°C). While the risk of temperature-related death for these pleasant temperatures is low, the temperatures occur so frequently that a significant number of deaths nevertheless is occurring at these temperatures, a point also made by Gasparrini, Guo, Hashizume, Lavigne, et al. (2015).

This motivated us to look at mortality caused by significant heat and cold. For each city, we select the 30 days each year with the highest heat- and cold-related deaths, which we refer to as significant heat- and cold-related deaths (Fig. 4.2d and 2e). Summing up all cities, there are on average 2,607 deaths per year due to significant heat, and 6,894 due to significant cold, which are 54% and 21% of total heat and cold related deaths, respectively. Thus, heat-related deaths tend to be more skewed towards extreme heat than cold deaths are towards extreme cold.

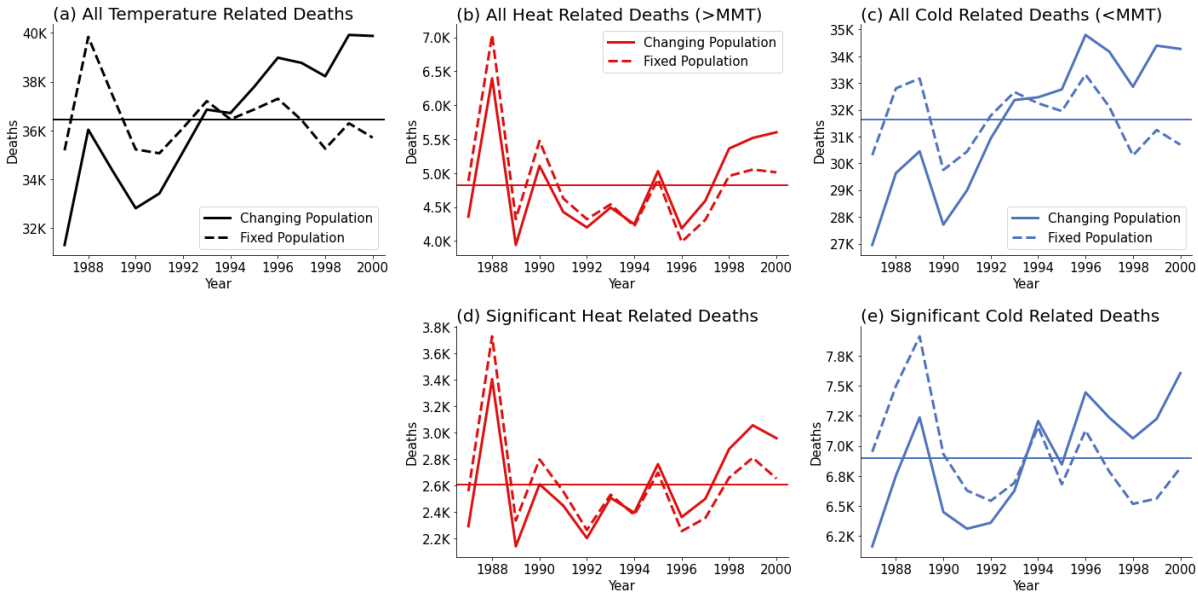

Figure 4.2. Time series of temperature-related deaths, summed over all 106 cities. (a) Solid line represents all temperature related deaths, while dashed line represents all temperature related deaths with fixed population (average population over 1987-2000 period). (b) Same as (a), but for heat-related deaths. (c) Same as (a), but for cold-related deaths. (d) Time series of deaths in the 30 days with largest number of heat-related deaths in each city. (e) Same as (d), but for cold-related deaths.

4.4. Measuring Adaptation

With the relatively short-term time period covered by the data (1987-2000), it is difficult to quantify the impacts of adaptation in data for a single city. However, we can quantify the effects of adaptation by comparing cities with different climates, an approach that has been used previously (Knowlton et al., 2007). In our implementation, for each city, we calculate the linear slope of cumulative RR versus the temperature for temperatures above the MMT (hot RR slope) and slope of RR below the MMT (cold RR slope). While the RR curves are not linear, the linear

fit gives us a metric for how steeply the curve rises. We do this fit separately for each age group. Fig. 4.3a and 3c show the hot RR slope regressed against median of daily average temperatures of the hot season (June, July, and August, JJA) of the 1987-2000 period. Fig. 4.3b and 3d show the cold RR slope regressed against the median daily average temperature of the cold season (December, January, and February, DJF).

There is a clear anti-correlation between the RR slopes and the cities' seasonal temperatures. Cities with warmer summers are less vulnerable to heat-related mortality (hot RR slopes closer to zero, Fig. 4.3a, c), while cities with colder winters are less vulnerable to cold-related mortality (cold RR slopes closer to zero, Fig. 4.3b, d). One can think of these fit lines in Fig. 4.3 as measures of existing adaptation to hot and cold climates (Gasparrini, Guo, Hashizume, Lavigne, et al., 2015; Heutel et al., 2021; Kalkstein & Greene, 1997; Knowlton et al., 2007).

We do not know how people will adapt as the climate warms, so we analyze two limiting scenarios. The first is no further adaptation. For this, we assume the RR curve of each city remains fixed at values obtained from the 1987-2000 mortality data as climate warms (Fig. 4.S1). Our second scenario, which we consider to be a strong adaptation case, assumes that, as each city warms up, the hot side of the city's mortality curve decreases following the regression lines in Figs. 4.3a and 4.3c. Specifically, we set the hot RR slope of each city in a particular year using the regression lines in Figs. 4.3a and 4.3c and that city's temperature over the previous 10 years. This is done by multiplying the hot-side RR curve by the ratio of the linear slope before and after adaptation. This process is done separately for two age groups.

The same methodology applied to the cold side of the mortality curve would result in cities becoming less adapted to the cold. We view this as implausible, so we incorporate adaptation on the cold side by scaling the cold RR slope by 18.5% of the ratio used to scale the hot RR slope

(18.5% is the ratio of the hot-side to cold-side fits shown in Fig. 4.3). A detailed example of how adaptation is incorporated is provided in Section 3 of the supplement.

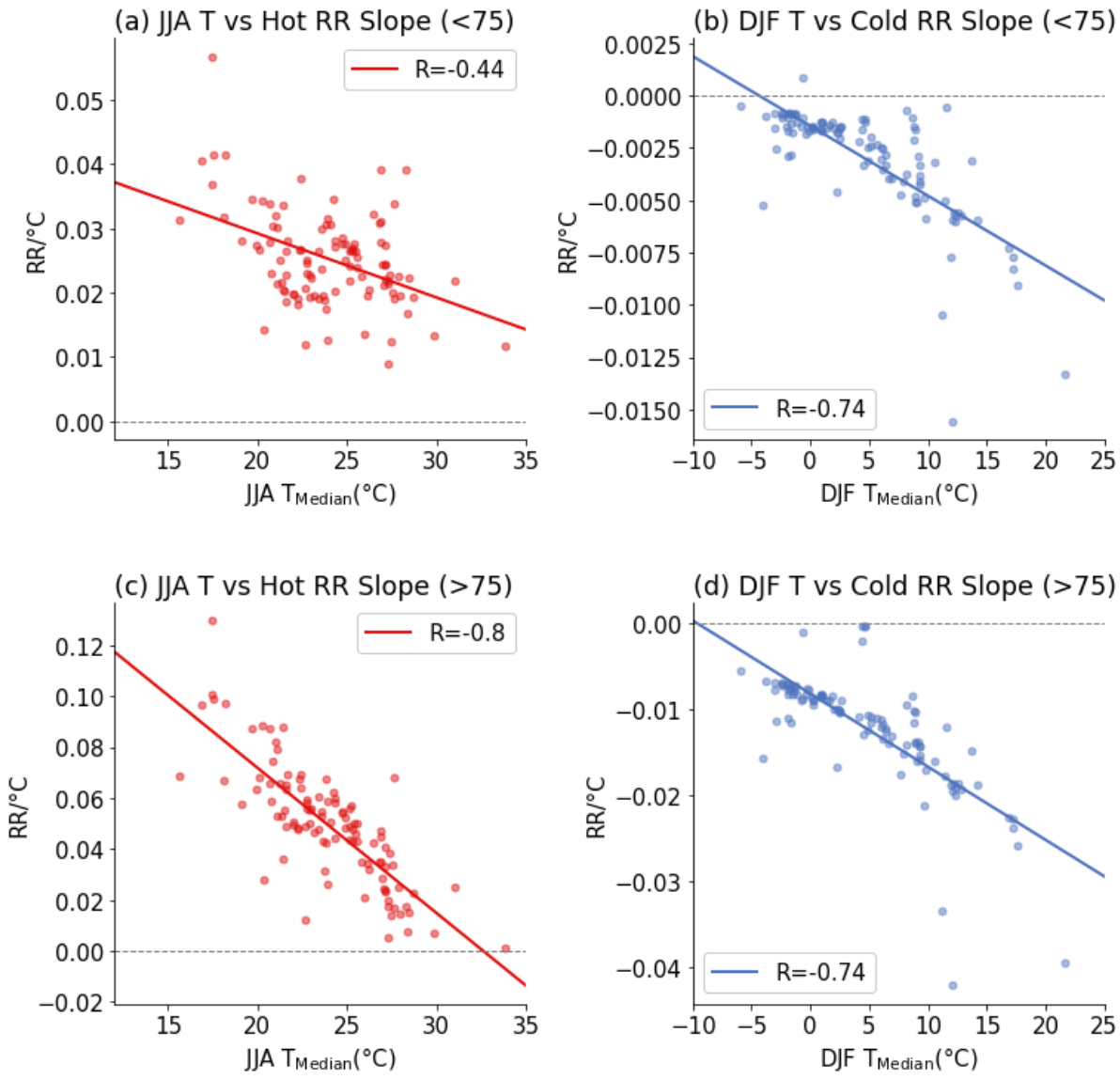

Figure 4.3. Relationship between the slope of each city's RR curve and that city's climate. (a) Relationship between slope of RR curve above MMT (hot RR slope) for under 75 age groups and the JJA median daily temperature. The points represent individual cities, and the line is a linear regression fit. (b) Same as (a), but for slope of RR curve below MMT (cold RR slope) and the median DJF temperature. (c, d) Same as (a, b), but for over 75 age groups.

4.5. Future Temperature-Related Deaths

For our projection of future temperature-related mortality, we utilize historical and RCP 8.5 scenario runs from NA-CORDEX (Mearns et al., 2017), which contain bias-corrected outputs of regional climate model (RCM) runs over North America, using boundary conditions from global climate models (GCM). Twelve combinations of GCMs and RCMs are used in this study, and these are summarized in Table 4.1. Historical simulations cover the period from 1950 to 2005 and RCP 8.5 simulations cover 2006 to 2099. Bias-corrected NA-CORDEX temperature only has daily maximum and daily minimum temperatures, so daily average temperature is calculated by averaging those. NA-CORDEX data are in 0.22°×0.22° horizontal resolution, so the 4 grid points nearest to each city are used to represent the temperature of the city.

Table 4.1. Description of NA-CORDEX members used in this study.

Scenario	Global Climate Model	Regional Climate Model	Bias-Correction
Historical + RCP 8.5	CanESM2	CanRCM4	MBCn using Daymet
		CRCM5-UQAM	
	GEMatm-Can	CRCM5-UQAM	
	GEMatm-MPI	CRCM5-UQAM	
	GFDL-ESM2M	RegCM4	
		WRF	
	HadGEM2-ES	RegCM4	
		WRF	
	MPI-ESM-LR	CRCM5-UQAM	
		RegCM4	
		WRF	
	MPI-ESM-MR	CRCM5-UQAM	

We validate the NA-CORDEX ensemble by predicting temperature-related deaths in 1987-2000 period. We do this by plugging temperatures from the NA-CORDEX ensemble for each city over that period into that city's regression model. The average number of temperature-related deaths estimated using NA-CORDEX temperatures is 36,675 (inter-model 95% CI = 36,189 – 37,231), in which 5,067 (95% CI = 4,666 – 5,332) deaths are heat-related, and 31,608 (95% CI = 31,111 – 32,331) are cold-related. Using ERA-5 temperatures, we estimated 36,444, 4,819, and 31,625 deaths, respectively. This provides some confidence in the NA-CORDEX temperature fields.

For future temperature-related mortality predictions, we also need predictions of population and demographics. For this, we use the SSP5 scenario, a fossil-fueled development scenario, which is usually paired with the RCP8.5 emissions. We use data from Hauer (2019), which contains county-level estimates of population and demographics at 5-year intervals from 2020 to 2100. To convert the county-level estimate to the city level, we extract counties containing each city in our analysis. 74% of the cities are within 1 county, and for these we assume that the city's population remains a constant fraction of the county's population. For cities that are in multiple counties, we sum the population of all counties that include the cities. Because the counties and city do not perfectly overlap, we take historical demographic data from 2020 and SSP5 data from 2020 and estimate the fraction of the total counties' population living in the city, and assume that fraction is constant over the century. From this, we come up with time series of population estimates in two age groups for each city in the coming century. A summary of population and demographic projections, as well as sensitivity due to choice of socioeconomic pathways can be found on the Supplement section 4.

To estimate future deaths, we plug NA-CORDEX temperatures for the 21st century for each city into that city's regression model (Fig. 4.6) and then use population and demographic information to convert RR to temperature-related mortality numbers.

RCP8.5 emissions will likely exceed actual emissions, so we plot estimated mortality as a function of global average surface temperature (relative to the 1850-1859 period). We take global average warming in each year of the CORDEX-NA from averages of the four global climate models included in CORDEX-NA: CanESM2 (5 ensemble members) (Chylek, Li, Dubey, Wang, & Lesins, 2011), GFDL-ESM2M (1 run) (Dunne et al., 2020), HadGEM2-ES (3 ensemble members) (Collins et al., 2011) and MPI-ESM (100 ensemble members) (Maher et al., 2019) with historical and RCP 8.5 forcing. We first average the ensemble members of each climate model and then average those to come up with the final global average temperature time series. This gives us the global average warming of 0.83°C in 2000 and 1.37°C in year 2022, close to observed values. With future climate projections from NA-CORDEX, future population and demographics projection from SSP5, and our two adaptation scenarios, we calculate future temperature-related mortality (Fig. 4.4a-d). Looking at total temperature-related deaths and no adaptation, we find that there are 45,800 deaths annually between 2011-2020 (1.16°C warming) and that is projected to grow to 200,000 with 3°C of global average warming, with both heat- and cold-related deaths increasing (Fig. 4.4a and 4.4b). There are 12,500 deaths due to significant temperatures (Fig. 4.4c, 4.4d), which is projected to increase to 63,000 at 3°C, a proportionally larger increase than all-temperature deaths. Adaptation will decrease this number, reducing the increase of temperature-related mortality at 3°C by about 28%.

We now decompose the increase in temperature-related mortality into contributions from climate change, demographics change, and population change. To estimate the impact of each of

these terms, we repeat the mortality calculation with that term fixed and then subtract the values obtained from the calculation with all terms varying.

To estimate the impact of climate change, we fix climate by repeating the daily temperature of recent years (2011-2020) for the entire period (1987-2100) and then subtracting the resulting temperature-related mortality from the all-factor calculation. For the no-adaptation case, lives saved by less cold balances the lives lost due to more hot temperatures until about 3°C. Above that, the increase in heat-related mortality overwhelms and total mortality rises rapidly. For the adaptation scenario, temperature-related mortality decreases at all temperatures.

We also find that temperature-related mortality in response to the most significant temperatures will increase at all levels of warming (Fig. 4.4g-h). This tells us that most of the lives saved in a warming world are due to a reduction in moderate cold temperatures.

Next, we look at impact of demographics (Fig. 4.4i-l) by performing a fixed-demographics calculation that fixes the ratio of under/over 75 population to the 2011-2020 average and then subtracting this from the all-factor calculation. We find that the aging of our population drives an enormous increase in deaths (Fig. 4.4i) due to the older age group being more vulnerable to temperature-related mortality (Fig. 4.4j).

Finally, we calculate the impact of population (Fig. 4.4m-p) by fixing population at the 2011-2020 average value and subtracting the results from the all-factor calculation. As the population increases, the total number of deaths also increases.

Comparing the three contributing terms, we find that changes in demographics and population are the most important driver of future mortality, and then climate change. This likely reflects the enormous investments in adaptation that have already been made (e.g., nearly 100% air conditioner penetration in cities like Phoenix and Houston). It seems certain that poorer

countries are experiencing more temperature-related mortality today and will experience even more as the climate warms in the future (Carleton et al., 2022).

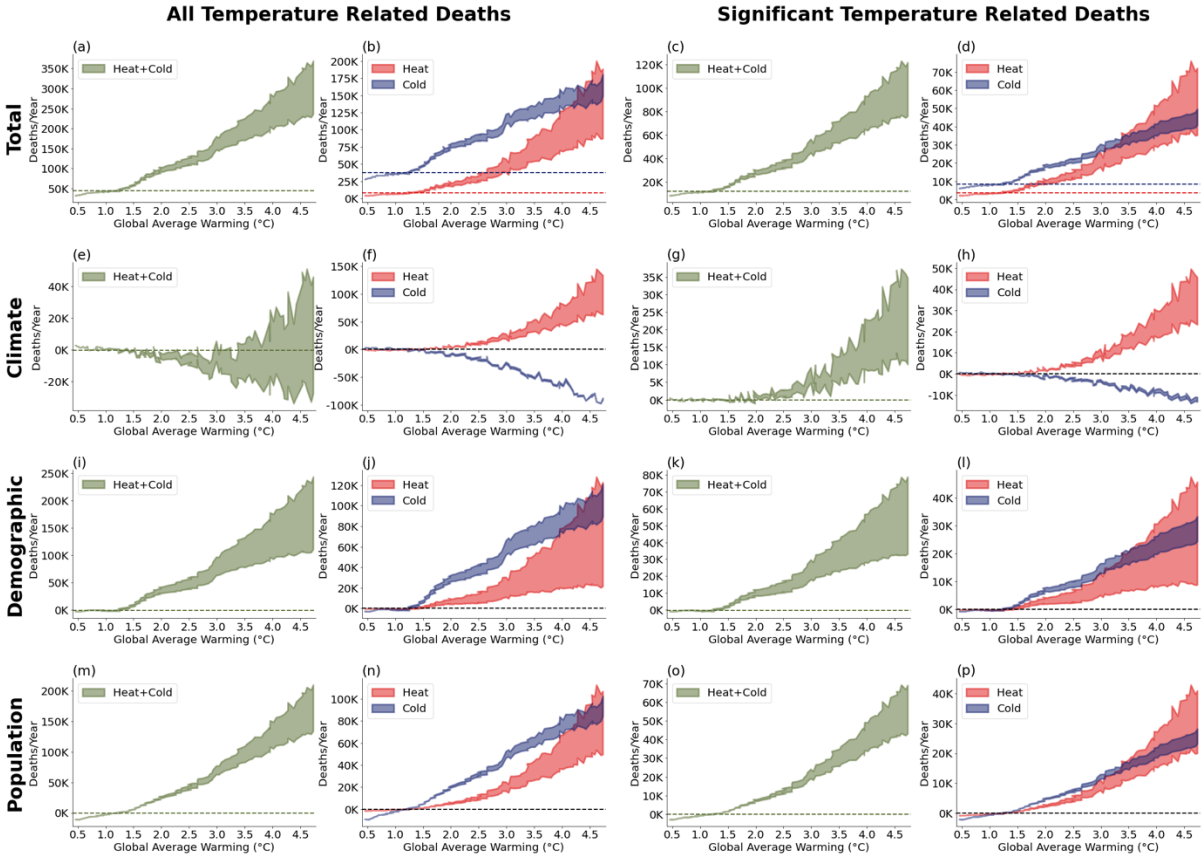

Figure 4.4. Estimates of future temperature-related deaths as a function of global average warming. (a-d) Future temperature-related deaths incorporating all factors: climate, demographics, and population. Upper limit of shaded region represents no-adaptation scenario, while the lower limit represents the adaptation scenario. (a) All temperature related mortality, (b) heat- and cold-related deaths, (c) mortality due to significant temperatures, (d) mortality due to significant heat and cold. Lower rows follow the same pattern as (a-d), but considering only climate change (e-h), demographics change (i-l) and population change (m-p). In all panels, dashed lines represent the average of the current value (2011-2020).

4.6. The Spatial Pattern of Temperature-Related Deaths

We now analyze the spatial distribution of heat-related mortality. We focus on the meridional variations in number of deaths at 3°C global average warming, approximately business-as-usual warming for 2100. We find that most of the temperature-related deaths occur between 40°N and 45°N (Fig. 4.5a). Analyzing per capita deaths, we find they are also weighted towards higher latitudes (Fig. 4.5c).

Looking at the climate contribution (Fig. 4.5e and 4.5g), we see that climate change shifts mortality poleward. This occurs because Southern cities in the U.S. are already well adapted to heat (Fig. 3), so further warming does not add significantly to heat-related deaths. However, these Southern cities do experience a decline of cold-related deaths, leading to a net reduction in temperature-related mortality. Northern cities, on the other hand, are less adapted to heat, so they experience large increases in heat-related mortality, which exceeds the decline in cold-related mortality.

The impact of adaptation is particularly pronounced between 30°N-35°N (Fig 4.5e) due to demographics. Currently, the 30°N-35°N region is the second youngest region (percentage of over 75 age group = 5.29%); when the Earth reaches 3°C of global average warming, it will be the oldest region (17.32%). Since the older age group is both more vulnerable to high temperatures and more sensitive to adaptation (Fig. 4.3), adaptation will have a large impact on mortality over this latitude range.

We have made similar plots for significant heat- and cold-related deaths (mortality in the hottest and coldest 30 days), and they show a stronger impact from climate change (Fig. S5). Numbers for all temperature-related deaths at 3°C warming are tabulated in Section S6 of the supplement.

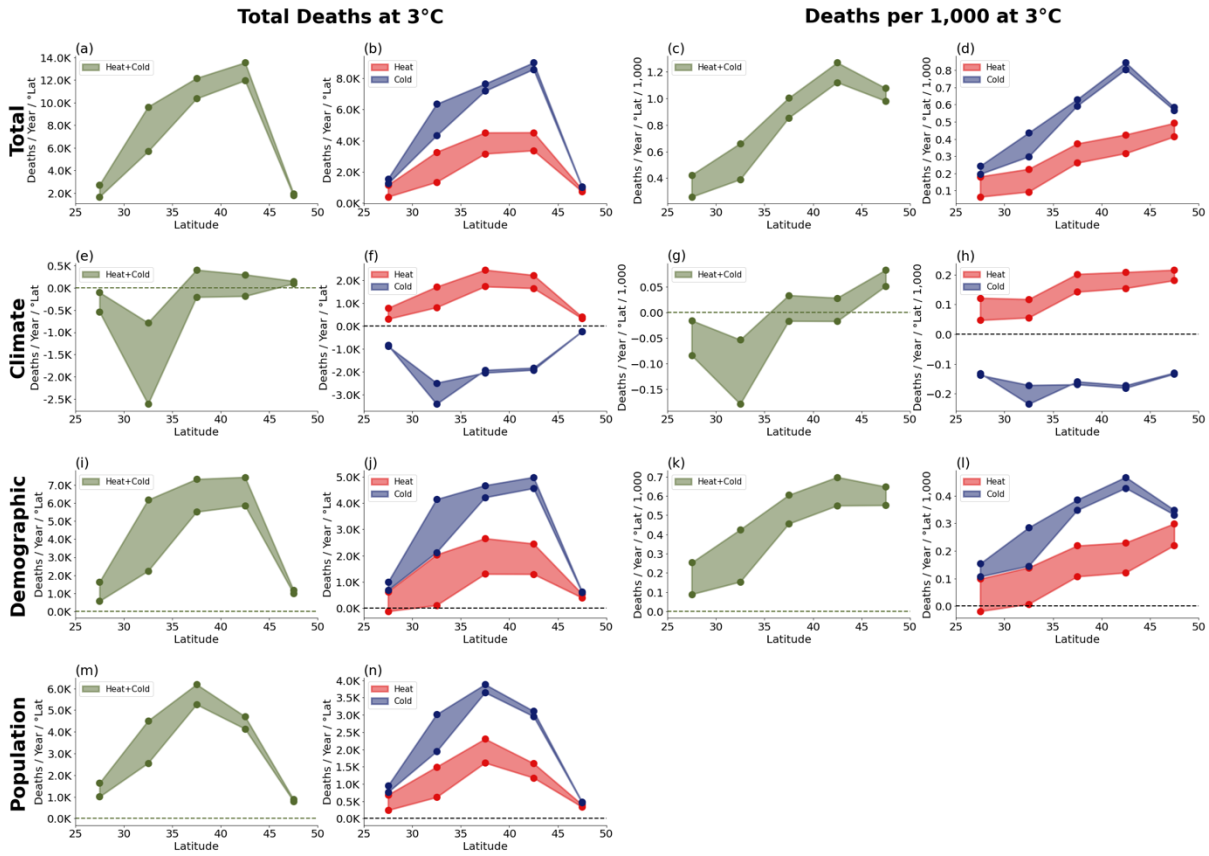

Figure 4.5. Meridional distribution of temperature-related deaths in 3°C world. (a) Number of temperature related deaths in 3°C world. The upper limit of the shaded region represents no-adaptation scenario, while the lower limit represents the adaptation scenario. (b) Same as (a), but for heat- and cold-related deaths. (c, d) Same as (a, b), but per capita (each bin has been divided by population in that bin). (e-h) Contribution of climate change to mortality, (i-l) contribution of demographic changes to mortality, (m-n) contribution of changes in population.

4.7. Conclusions

In this paper, we use mortality and temperature data obtained between 1987 and 2000 to develop a temperature-mortality relationship for 106 cities in the U.S. covering about 65% of the total population. We then use the regression models with temperatures from an ensemble of high-

resolution climate simulations to estimate future temperature-related deaths. Because of the key role of adaptation, we make two different adaptation scenarios: a scenario with no adaptation and what we consider to be an aggressive adaptation scenario that follows the observed variations in adaptation between cities with different climates. We also incorporate estimates of changing population and its age distribution.

We estimate that there was an average of 36,444 temperature-related deaths per year during the period 1987-2000 in the cities in our data set. Consistent with previous work (Berko, 2014; Gasparrini, Guo, Hashizume, Kinney, et al., 2015; Gasparrini et al., 2017; Heutel et al., 2021), we find that 86% of these deaths were cold-related. Most of the cold-related deaths took place at moderate temperatures just below the minimum mortality temperature (MMT), typically around 20°C, so they are categorized as cold related even though many would consider the temperatures to be mild.

We project that, with a warming climate and an increasing and aging population, temperature-related deaths will reach 200,000 per year at 3°C of global average warming without adaptation. Assuming effective adaptation reduces the increase of this number of temperature-related deaths at 3°C of warming by 28%.

By decomposing mortality into climate, demographics, and population factors, we find that demographic shifts, primarily the aging of the population, and increasing population – will be the biggest drivers of increased temperature-related mortality. Climate change will cause small changes in mortality below 3°C of global average warming due to offsetting decreases in cold-related mortality and increases in heat-related deaths. Above 3°C, the result depends on the level of adaptation with increases in heat-related deaths dominating without adaptation. Without adaptation, total mortality rises rapidly; with adaptation, mortality declines.

While changes in temperature-related mortality due to climate change may be small below 3°C, there is a meridional shift of mortality, with deaths shifting from the South to the North (Fig. 4.5g-4.5h). Since Southern cities in U.S. are already well adapted to heat, additional warming does not add a significant number of deaths. However, Northern cities are not well adapted to heat, so heat-related mortality increases there dominate decreases in cold-related mortality.

Ultimately, no one knows how effectively we will adapt to the warmer temperatures of the coming century. However, the investments society has made to make cities like Houston or Phoenix livable in a hot climate are massive and it is far from assured that we will make similar investments in other cities as the climate warms. Many adaptive responses (e.g., installing air conditioning, improved health care, better urban planning) are too expensive for poorer individuals or communities, so adaptation will necessarily require society to pay for much of the adaptation. This would represent a huge transfer of wealth from richer to poorer members of our society, a dicey proposition in today's political environment.

There are important limitations to our analysis. First, our analysis covered 106 large cities in the U.S., so we can't reach any conclusions about rural populations of the U.S. population or Northern states that are not included in the mortality dataset (MT, ID, WY, ND, and SD). Second, we also cannot comment on the future of heat-related mortality in the rest of the world. However, given the wealth of the U.S., our present levels of adaptation are higher than in many poorer countries and our ability to enhance our adaptation is also higher. Thus, it seems likely that heat-related mortality will be a more significant problem in the rest of the world as climate change progresses through the century (Carleton et al., 2022).

4.8. Supplementary Materials for Chapter 4

4.8.1. Distributed Lag Non-linear Model (DLNM) – Model Specification and Sensitivity

The DLNM setup in this study follows a framework from Gasparrini, Guo, Hashizume, Kinney, et al. (2015) and Gasparrini, Guo, Hashizume, Lavigne, et al. (2015). All calculations are done with the R packages *dlnm* and *mvmeta*.

4.8.1.1. First stage model

In the first stage, estimates of location and the age-specific temperature-mortality relationship is derived using a generalized linear model with a quasi-Poisson family. We use the following equation in this model:

$$log\left(Death_{c,a}\right) = cb(tMean_c, lag = 21) + DOW + ns(DOY) + ns(Year) \qquad (1)$$

Where $Death_{c,a}$ represents number of daily deaths in city *c* and age group *a*. $cb(tMean_c, lag = 21)$ is a cross basis function of temperature in city *c*, with up to 21 days of lag, which is obtained by the two equations of exposure-response relationship and lag-response relationship between temperature and mortality (Gasparrini, 2014). In this study, we select a cross-basis composed of quadratic B-spline with three internal knots placed at the 10^{th}, 75^{th}, and 90^{th} percentiles of the location-specific temperature. An indicator of day of week (*DOW*) is included for the weekly cycle. A natural cubic B-spline with 8 degrees of freedom for day of year is included to control the seasonal cycle (*ns(DOY)*), and a natural cubic B-spline with 1 degree of freedom per decade is included for the long-term trend (*ns(Year)*).

The association of overall temperature-mortality relationship from eq. 1 is reduced to the cumulative relationship between temperature and mortality with the function *crossreduce*, included in *dlnm*.

4.8.1.2. Second stage model

The multivariate meta-analysis model (Gasparrini & Armstrong, 2013; Gasparrini, Armstrong, & Kenward, 2012) is used for the meta-analysis. It is difficult to extract the temperature-mortality relationship from some of the cities with small number of populations, due to high signal-to-noise ratio of daily deaths. Multivariate meta-analysis allows the temperature-mortality relationship in small cities to share the information of temperature-mortality relationship of larger cities with similar characteristics. For the characteristics for the city, we include average temperature, temperature range (75^{th} percentile – 25^{th} percentile), and latitude of each city (Gasparrini & Armstrong, 2011; Gasparrini, Guo, Hashizume, Kinney, et al., 2015; Gasparrini, Guo, Hashizume, Lavigne, et al., 2015). Package *mvmeta* is used for this analysis, and technical details of this analysis can be found in Gasparrini and Armstrong (2013).

4.8.1.3. Calculation of excess deaths due to temperature

Cumulative risk ratio (RR) is calculated as a sum of RR in all lags (up to 21 days). This returns a cumulative RR relative to the mortality at minimum mortality temperature (MMT; Fig. 1 in main text and Fig. S1). Baseline deaths per thousand (baseline DPT) at the MMT is calculated by averaging the DPT values for the days within 0.5°C of MMT. From this, we can calculate DPT values at each day by multiplying cumulative RR to base DPT. We then calculate the number of excess deaths due to temperature by multiplying excess DPT by population.

4.8.1.4. Sensitivity analysis

We tested the sensitivity of our results to the selection of parameters in the DLNM. The number of degrees of freedom to account for seasonality (dfSeas) was modulated from 7 to 9 (current value=8), and the number of degrees of freedom to account for the long-term trend (dfTrend) was modulated from 1 to 2 (current value=1). Table 4.2. shows the percent change in the number of deaths caused by this modulation, calculated for each city. Overall, the choice of parameters changes excess deaths by less than 8%.

Table 4.2. Percent change of number of deaths due to sensitivity analysis. Percent changes are calculated for each city and average percent changes are shown in the table, while the inter-city standard deviation is shown in parentheses.

JJA

	dfSeas=7	dfSeas=8	dfSeas=9
dfTrend=1	1.76	0	0.02
	(3.95)		(3.21)
dfTrend=2	1.86	-0.08	-0.10
	(4.10)	(0.08)	(3.26)

DJF

	dfSeas=7	dfSeas=8	dfSeas=9
dfTrend=1	4.19	0	-7.55
	(8.84)		(5.06)
dfTrend=2	4.81	0.52	-6.92
	(8.60)	(0.84)	(4.47)

4.8.1.5. Impact of Ozone

High Ozone (O_3) concentration is known to impact human health (Ren, Williams, Morawska, Mengersen, & Tong, 2008). However, O3 is also known to be correlated with temperature, especially in summertime (Porter & Heald, 2019), so it is difficult to distinguish the impact of O_3 and temperature on number of deaths. In that context, we tested if prediction errors of the DLNM (residuals) correlated with O_3 concentration.

In cities that average more than 20 daily deaths (24 cities), we calculate the prediction residual and regress against O_3 concentration. Annually, the p value of this regression is 0.58 (inter-city standard deviation $1\sigma=0.28$). For JJA, the p value is 0.48 ($1\sigma=0.29$), showing no significant correlation between the prediction residual and O_3 concentration.

Since the effect of O_3 could be non-linear, we computed the composite analysis between the residuals on the high O_3 days (over 75^{th} percentile of O_3) and low O_3 days (under 25^{th} percentile of O_3). In a t-test comparing the means of the annual values, the p value is 0.59 ($1\sigma=0.27$). When comparing only JJA, the p value is 0.48 ($1\sigma=0.30$), showing that there is no significant difference of the prediction residuals on high O_3 days vs. low O_3 days.

With this analysis, we see no evidence that our results are impacted by O_3. However, given the high collinearity between temperature and O_3, we cannot rule out some contribution to mortality from O_3. Clearly, more work on this is warranted.

4.8.2. RR Curve for Populated Cities

Fig. 4.1 in the main text shows the RR values that are averaged for all cities. Fig. 4.6 shows the RR curves for the 25 most populated cities.

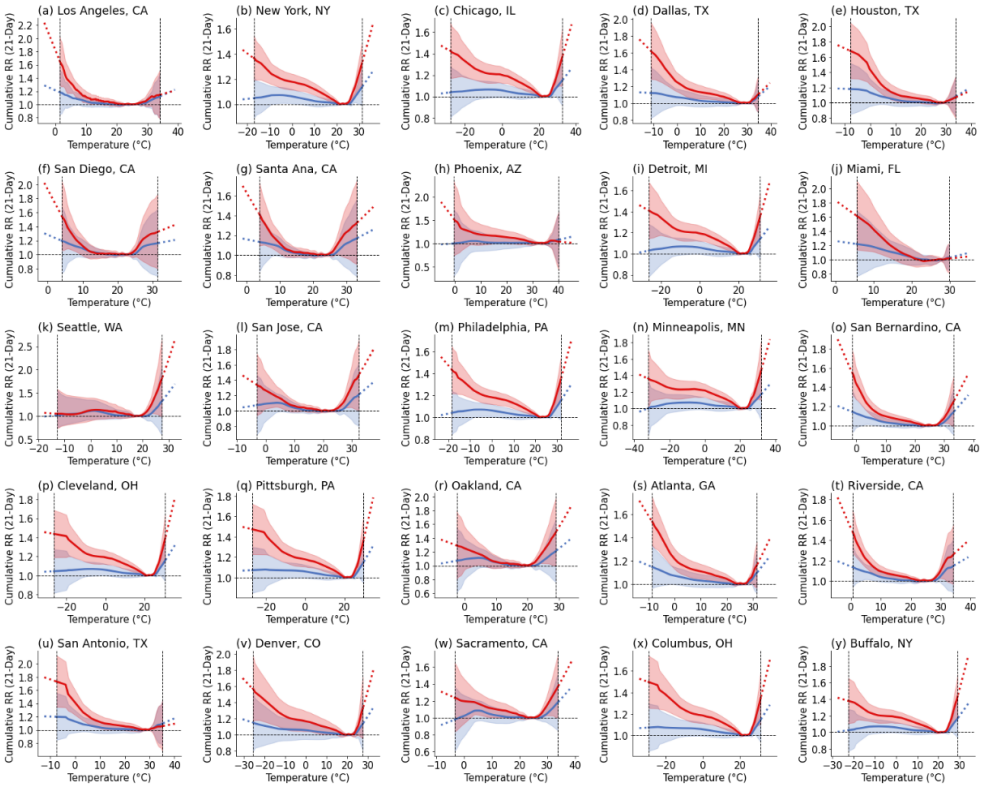

Figure 4.6. RR curve for 25 most populated cities. The red line represents the RR for the over 75 age group and the blue line represents the under 75 group. Solid lines are for historical temperature range, and dashed line are extrapolated RR values for the temperature outside the historical observations. Shaded regions show the 95% confidence interval of RR curve.

4.8.3. Measuring and Applying Adaptation – Example of New York

For a more detailed explanation of measuring adaptation, here we go through an example of how we apply adaptation in our analysis. We select the >75 old age group in the city of New York City (NYC) in this example, but same process is applied for all age groups and all individual cities.

Fig. S2a shows that, in the 1987-2000 period, median JJA temperature in NYC was 22.7°C, according to ERA-5. From the projections of CORDEX-NA, median JJA temperature rises to 25.6°C in a world with 3°C global average warming.

In the 1987-2000 period, the hot-side RR slope of NY is 0.0491 (RR/°C) (blue dashed line and blue dot in Fig. S2b). As seen in Fig. S2c, the RR curves are not exactly linear, but the linear fit gives us a metric for how steeply the curve rises.

Using the slopes of the linear fits computed from all cities, we find that the hot side RR slope changes by -0.0057 (RR/°C/°C) as JJA median temperature increases (Fig. 4.3c in the main text, gray dashed line in Fig S2b). Using the increase in JJA median temperature for NYC, we therefore estimate that the hot-side RR slope of NY would decrease to 0.0296 (RR/°C) in a 3°C warmer world (red dashed line and red dot in Fig. 4.7.b).

The last step is to adjust the RR curve by multiplying the hot-side mortality curve by the ratio of hot-side RR slope of 1987-2000 to that in 3°C world (0.0322/0.0491). This gives the RR curve in 3°C world (red line above the MMT in Fig. 4.7.c). For the cold-side RR curve, the mortality curve is decreased by 18.5% of the ratio of the hot-side RR curve (red line below the MMT Fig. 4.7.c), as discussed in the main text.

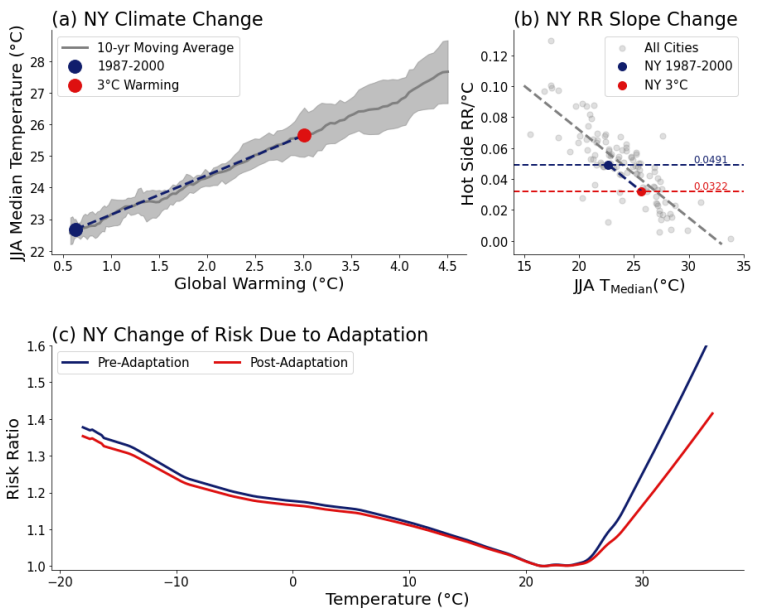

Figure 4.7. Example of measuring and applying adaptation, with >75 age group in New York City as example. (a) Current and future JJA median temperature. Gray shaded region is the upper and lower limit of climate projection from CORDEX-NA, and the gray solid line is the mean projection of NA-CORDEX. The values for the NA-CORDEX are smoothed with 10-yr moving average. Blue point is the 1987-2000 JJA median temperature from ERA-5, and red point is the JJA median temperature at 3°C of global warming. (b) Change of hot side RR slope with temperature. Gray points and dashed line represent the individual cities and the linear fit of those cities, same as Fig. 3c in the main text. Blue point and red point each show the hot side RR slope of NYC in 1987-2000 period and 3°C world. (c) Change of RR curve in NYC. Blue line represents the RR curve in 1987-2000 period, and red line represents the RR curve in 3°C world, when adaptation applied.

4.8.4. Future Population Scenario

Fig. 4.8 summarizes the future population and demographic change. In the 106 cities used in this study, total population increases at a rate of 18.5 million/decade. The fraction of population

over 75 also increases at an average rate of 1.7%/decade. Top three cities with highest population increase are Austin (TX), Denver (CO), and Raleigh (NC), wile top three cities with fastest aging population are Jackson (MS), Richmond (VA), and Santa Ana/Anaheim (CA).

Furthermore, we test the sensitivity due to future population scenario by comparing SSP2 (middle of the road) scenario with SSP5 scenario (currently used in the main text). First looking at total population, we observe a lower population increase in SSP2 scenario (Fig. 4.8.a). This would decrease the contribution of population to total deaths (Figs. 4.4.m-444.p). The proportion of >75 age groups are very similar until year 2080 (3.3°C warming, Fig. 4.8.b), so the contribution of changing demographics would be similar (Figs. 4.4.i-4.4.l), although the magnitude differs by the ratio of population in SSP5 and SSP2 (0.8 in 3°C warming). The impact of climate change (Figs. 4.4.e-4.4.h) is also similar with magnitude decreasing by the ratio of population in SSP5 and SSP2.

The inter-city pattern of slope of change in population and >75 age group ratio is nearly identical in SSP5 and SSP2. The R^2 of the regression between the population slope distribution (Fig. 4.8.c shows the slopes for SSP5) between SSP5 and SSP2 is 0.999 and R^2 value of aging slope distribution (Fig. 4.8.d) is 0.996.

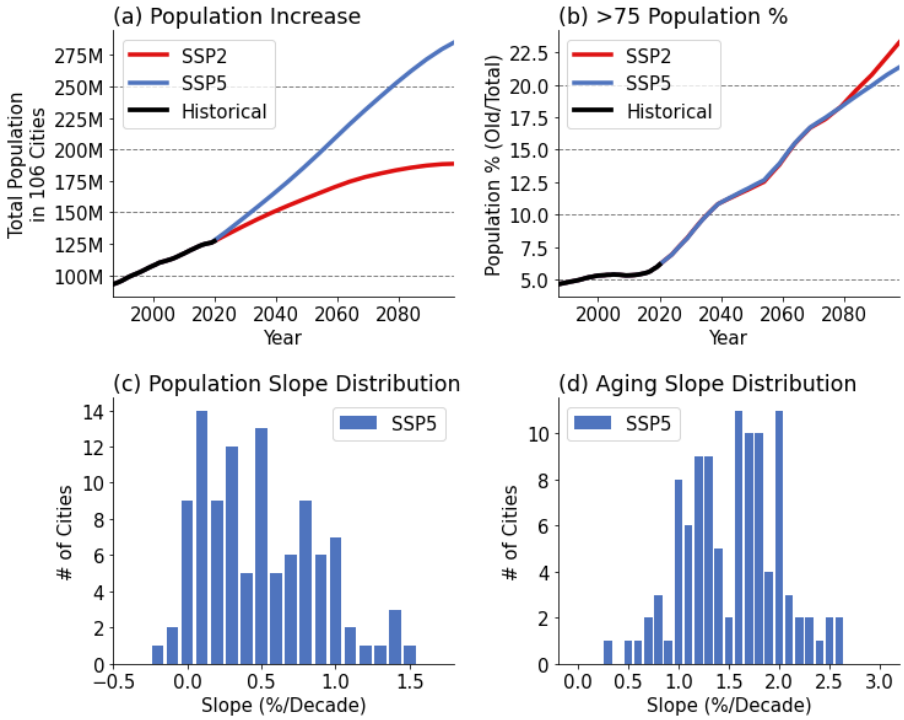

Figure 4.8. Summary of future population and demographic change. (a) Change of total population for all 106 cities in SSP2 and SSP5 scenarios. (b) Change in fraction of > 75 population, calculated by adding all > 75 population over 106 cities and dividing by total population. (c) Distribution of population trends of individual cities in the SSP5 scenario, relative to average historical population (1987-2020). (d) Distribution of growth of the fraction of the > 75 age group, in the SSP5 scenario.

4.8.5. Meridional Distribution of Significant Temperature Related Deaths

In correspondence with Fig. 4.5 in the main text, here we show the plot same as Fig. 4.5, but using significant temperature related deaths, which is 30 days each year with the highest heat- and cold-related deaths.

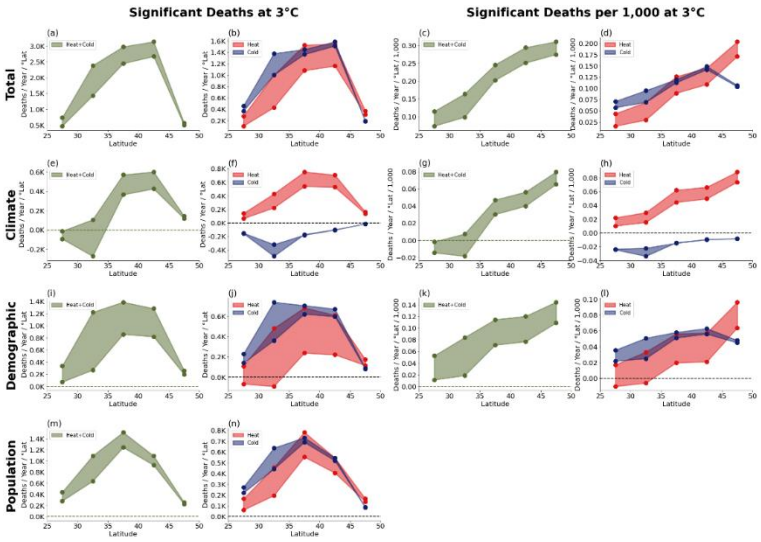

Figure 4.9. Meridional distribution of significant temperature-related deaths in 3°C world, where significant refers to the 30 days of the year with the highest number of heat- and cold-related deaths. (a) Number of deaths in 3°C world. Upper limit of the shaded region represents no-adaptation scenario, while the lower limit represents the adaptation scenario. (b) Same as (a), but for heat- and cold-related significant deaths. (c, d) Same as (a, b), but per capita (each bin has been divided by population in that bin). (e-h) Contribution of climate change to mortality, (i-l) contribution of demographic changes to mortality, (m, n) contribution of changes in population.

4.8.6. Future predictions of Temperature Related Deaths

In correspondence with Fig. 4.4 and 4.5 in the main text, Table 4.3 shows the values of total projected deaths including all factors at 3°C global average warming as well as our estimate of deaths just due to climate change. Table 4.4 shows the same thing for significant temperatures.

Table 4.3. The number of temperature related deaths in each city at 3°C warming, and number of deaths caused by climate change. XA = excluding adaptation, OA = with adaptation. Negative

numbers indicate a reduction in mortality at 3°C. Shading in the table represents the magnitude of increase (red) and decrease (blue)

City	Deaths						Climate Effect					
	Heat+Cold		Heat		Cold		Heat+Cold		Heat		Cold	
	XA	OA	XA	OA	XA	OA	XA	OA	XA	OA	XA	OA
Akron, OH	713	645	244	194	468	451	13	-8	118	93	-105	-101
Albuquerque, NM	972	706	320	129	652	577	-16	-90	159	66	-176	-156
Arlington, VA	623	555	199	150	424	405	-3	-22	93	69	-96	-92
Atlanta, GA	3080	2633	972	653	2109	1980	-75	-215	546	368	-621	-583
Austin, TX	2255	1451	674	143	1581	1308	-316	-516	376	93	-692	-609
Bakersfield, CA	1200	971	491	311	709	660	64	-20	271	173	-207	-193
Baltimore, MD	782	716	272	223	510	493	20	-1	138	113	-118	-114
Baton Rouge, LA	309	231	113	55	195	176	-17	-42	68	35	-85	-77
Biddeford, ME	613	562	238	198	375	364	38	19	125	103	-87	-84
Birmingham, AL	612	496	207	123	404	373	-1	-41	124	74	-125	-115
Boston, MA	2214	1993	837	667	1376	1326	98	21	427	338	-329	-317
Buffalo, NY	1536	1413	567	472	969	940	87	43	293	243	-207	-200
Cayce, SC	413	330	141	81	272	250	-10	-34	72	42	-82	-75
Cedar Rapids, IA	648	565	203	144	445	421	2	-20	92	65	-90	-85
Charlotte, NC	2658	2286	903	630	1754	1656	5	-114	479	333	-474	-447
Chicago, IL	8665	7827	2531	1949	6134	5878	-98	-329	1213	926	-1311	-1255
Cincinnati, OH	1042	921	347	259	695	662	12	-25	172	128	-160	-153
Cleveland, OH	1456	1348	468	390	988	958	15	-18	235	195	-220	-213
Columbus, GA	305	259	113	78	192	181	8	-9	70	49	-62	-58
Columbus, OH	3511	3126	1161	879	2351	2247	11	-101	548	412	-537	-513
Colorado Springs, CO	1833	1653	907	756	926	897	316	225	603	502	-286	-277
Corpus Christi, TX	327	228	187	104	140	124	21	-21	132	78	-111	-99
Coventry, RI	204	180	72	54	132	126	7	-1	38	28	-30	-29
Dayton, OH	528	471	181	140	346	331	9	-9	89	68	-80	-77
Washington, DC	2346	2109	772	599	1574	1509	8	-61	371	286	-363	-348
Denver, CO	8438	7269	3648	2713	4790	4556	1093	564	2293	1706	-1200	-1142
Des Moines, IA	1443	1253	450	316	993	937	2	-50	217	152	-214	-202
Detroit, MI	1555	1376	486	359	1069	1017	14	-35	220	162	-207	-197
Dallas/Fort Worth, TX	7806	5467	2411	792	5395	4675	-332	-1071	1472	516	-1804	-1587
El Paso, TX	818	532	194	35	625	497	-118	-173	81	19	-199	-192
Evansville, IN	333	282	115	78	218	204	10	-6	61	41	-51	-47
Fresno, CA	1472	1198	595	380	877	819	79	-18	304	192	-225	-210
Fort Wayne, IN	816	706	277	195	540	511	4	-26	124	87	-120	-113
Grand Rapids, MI	1835	1647	653	512	1182	1136	60	5	296	231	-235	-226
Greensboro, NC	981	862	348	259	633	603	13	-25	180	134	-167	-159
Houston, TX	5956	3763	1985	460	3971	3303	-770	-1387	1154	298	-1924	-1685

Huntsville, AL	740	629	238	159	501	470	-2	-39	140	94	-142	-133
Indianapolis, IN	1770	1536	592	422	1177	1115	9	-58	281	199	-272	-257
Jackson, MS	368	283	123	62	244	221	-12	-40	72	37	-85	-77
Jacksonville, FL	963	776	451	297	512	479	67	-19	303	202	-237	-221
Jersey City, NJ	1622	1433	561	420	1061	1013	35	-23	269	200	-234	-223
Johnstown, PA	89	81	33	27	56	55	4	1	16	13	-13	-12
Kansas City, MO	2175	1926	729	548	1446	1378	67	-22	423	318	-356	-339
Kansas City, KS	324	287	111	84	213	203	13	0	66	50	-53	-50
Kingston, NY	231	213	84	70	147	143	8	2	40	33	-32	-31
Knoxville, TN	732	649	265	203	467	446	30	-1	153	117	-123	-118
Los Angeles, CA	7391	4216	2581	369	4810	3848	-1894	-2435	1005	203	-2900	-2638
Lafayette, LA	439	304	160	59	279	244	-29	-72	95	38	-125	-109
Las Vegas, NV	6564	4997	1974	906	4591	4091	36	-369	974	467	-938	-837
Lexington, KY	653	558	221	151	433	407	6	-24	113	77	-108	-101
Lincoln, NE	779	646	246	153	533	493	10	-28	125	78	-115	-107
Lake Charles, LA	261	181	93	35	168	146	-18	-43	59	24	-77	-68
Louisville, KY	1498	1286	498	343	1000	943	9	-57	254	175	-245	-231
Little Rock, AR	569	452	175	93	394	359	-3	-41	105	57	-108	-98
Lubbock, TX	409	285	133	45	277	240	-26	-60	72	26	-98	-86
Madison, WI	1435	1279	447	336	988	942	-7	-45	188	141	-195	-186
Memphis, TN	1333	1147	462	325	870	822	51	-20	286	201	-235	-221
Miami, FL	1365	468	979	221	386	246	195	-391	785	189	-590	-580
Milwaukee, WI	1526	1349	460	335	1066	1014	18	-38	237	170	-218	-207
Minneapolis/St. Paul, MN	4752	4320	1403	1105	3349	3216	34	-73	610	480	-576	-553
Mobile, AL	302	227	119	62	183	165	2	-28	80	42	-77	-70
Modesto, CA	728	638	299	227	429	411	33	-1	161	122	-128	-123
Muskegon, MI	548	511	196	168	352	343	37	22	115	98	-78	-76
Nashville, TN	1553	1342	541	385	1012	957	44	-31	313	223	-268	-254
Newport News, VA	255	220	100	72	155	147	10	-3	54	39	-45	-42
New Orleans, LA	1532	1383	694	573	838	810	137	61	513	424	-375	-363
Norfolk, VA	327	287	129	97	198	189	14	-1	72	55	-58	-55
Newark, NJ	2122	1876	735	551	1388	1324	47	-29	353	264	-306	-292
New York, NY	18954	16245	6440	4439	12513	11805	381	-458	3164	2168	-2783	-2626
Oakland, CA	1589	1389	865	689	725	700	13	-65	450	356	-436	-421
Oklahoma City, OK	1615	1270	528	282	1087	988	6	-109	318	175	-312	-284
Olympia, WA	642	584	289	241	353	343	21	3	116	96	-95	-92
Omaha, NE	1534	1315	475	322	1059	993	14	-49	239	163	-226	-212
Orlando, FL	1423	1119	803	538	621	582	237	67	603	410	-367	-343
Philadelphia, PA	2795	2484	998	764	1797	1719	91	-8	491	376	-401	-384
Phoenix, AZ	9961	1098	2139	360	7822	738	-1076	-7074	684	171	-1760	-7245
Pittsburgh, PA	1646	1501	572	463	1074	1037	32	-13	275	221	-243	-234
Portland, OR	2855	2569	1270	1034	1585	1534	128	44	490	395	-363	-351
Providence, RI	971	842	348	250	623	592	36	-8	178	127	-142	-135

Raleigh, NC	2992	2573	1070	755	1923	1818	9	-120	537	380	-528	-499
Richmond, VA	1160	1015	420	311	739	704	16	-29	205	152	-189	-180
Riverside, CA	2388	1842	972	537	1416	1305	-123	-288	492	280	-615	-569
Rochester, NY	1072	993	389	329	683	664	44	15	206	173	-162	-158
Sacramento, CA	2427	2091	932	670	1494	1420	29	-81	452	320	-423	-401
Salt Lake City, UT	3578	3118	1438	1080	2140	2038	396	209	849	640	-453	-432
San Antonio, TX	2389	1291	725	170	1664	1120	-437	-848	380	116	-817	-964
San Bernardino, CA	2074	1789	775	556	1299	1233	-102	-186	396	288	-498	-474
San Diego, CA	2133	1385	1434	742	700	642	162	-213	922	486	-760	-699
San Francisco, CA	535	452	426	347	108	105	125	76	279	225	-154	-150
San Jose, CA	1728	1516	691	522	1037	994	-266	-310	257	191	-523	-501
Seattle, WA	2931	2732	1436	1267	1495	1465	284	210	670	588	-386	-378
Shreveport, LA	298	219	93	38	205	181	-16	-40	56	24	-72	-64
Spokane, WA	1592	1418	668	530	924	888	199	139	331	266	-132	-127
Santa Ana/Anaheim, CA	2211	1671	1251	774	960	897	-73	-288	707	442	-780	-730
St. Louis, MO	710	627	231	172	479	455	13	-14	124	92	-111	-106
Stockton, CA	933	829	404	320	529	509	35	-4	211	166	-176	-170
St. Petersburg, FL	736	466	375	148	362	318	50	-87	285	119	-235	-205
Syracuse, NY	611	549	236	188	375	361	29	8	113	89	-84	-81
Tacoma, WA	1706	1556	783	660	922	897	114	63	347	290	-233	-227
Tampa, FL	1407	986	756	396	651	590	178	-48	572	308	-394	-356
Toledo, OH	505	439	162	115	343	325	3	-15	72	51	-70	-66
Topeka, KS	225	193	78	55	147	138	9	-3	45	32	-37	-35
Tucson, AZ	456	232	114	25	342	207	-57	-150	43	13	-100	-164
Tulsa, OK	1373	1104	480	282	893	822	47	-55	301	178	-254	-234
Wichita, KS	871	684	287	152	583	531	22	-44	169	90	-147	-134
Worcester, MA	1164	1035	396	301	768	735	24	-15	181	136	-158	-151

Table 4.4. The number of significant temperature related deaths in each city at 3°C warming, and number of significant temperature related deaths caused by climate change.

	Deaths						Climate Effect					
City	Heat+Cold		Heat		Cold		Heat+Cold		Heat		Cold	
	XA	OA	XA	OA	XA	OA	XA	OA	XA	OA	XA	OA
Akron, OH	212	187	103	83	108	104	38	29	46	37	-8	-8
Albuquerque, NM	288	190	135	55	152	135	31	0	58	23	-27	-24
Arlington, VA	182	158	82	62	100	95	27	19	35	26	-8	-7
Atlanta, GA	956	796	400	273	556	522	111	56	195	135	-84	-79
Austin, TX	708	446	234	53	474	393	-32	-81	87	28	-120	-109

Bakersfield, CA	406	312	223	142	183	170	87	48	112	72	-25	-24
Baltimore, MD	241	216	120	99	121	117	48	38	58	48	-10	-10
Baton Rouge, LA	99	75	35	18	64	57	1	-4	15	8	-14	-13
Biddeford, ME	197	176	110	92	86	84	50	41	56	47	-6	-6
Birmingham, AL	188	148	80	49	108	100	24	10	40	25	-16	-15
Boston, MA	690	604	369	294	321	310	155	119	178	141	-23	-22
Buffalo, NY	476	427	261	218	215	209	117	95	131	109	-14	-14
Cayce, SC	126	98	52	31	73	68	12	4	21	13	-9	-8
Cedar Rapids, IA	184	154	85	61	99	93	31	21	36	26	-5	-5
Charlotte, NC	825	689	379	268	446	421	128	78	181	128	-53	-50
Chicago, IL	2408	2114	1066	827	1343	1287	374	275	453	351	-79	-76
Cincinnati, OH	303	261	139	104	164	156	48	33	62	47	-14	-13
Cleveland, OH	431	390	208	174	223	217	81	65	98	81	-17	-16
Columbus, GA	99	82	45	32	53	50	16	9	24	17	-9	-8
Columbus, OH	1017	882	464	354	552	528	156	110	198	150	-42	-40
Colorado Springs, CO	694	610	461	384	233	226	240	194	287	239	-47	-45
Corpus Christi, TX	117	86	57	32	60	53	5	-4	31	19	-25	-23
Coventry, RI	64	54	33	25	31	29	14	10	16	12	-2	-2
Dayton, OH	156	136	74	58	82	78	27	20	34	26	-7	-6
Washington, DC	702	615	328	256	374	359	116	85	145	113	-29	-28
Denver, CO	2877	2375	1766	1318	1110	1056	903	648	1033	771	-130	-124
Des Moines, IA	410	343	188	133	223	210	72	49	83	59	-11	-11
Detroit, MI	446	380	214	159	232	221	77	54	90	67	-13	-13
Dallas/Fort Worth, TX	2352	1551	935	321	1417	1230	188	-66	459	174	-271	-240
El Paso, TX	232	140	74	14	158	126	-12	-29	22	6	-34	-35
Evansville, IN	98	81	47	32	51	48	17	11	22	16	-5	-4
Fresno, CA	479	371	263	169	217	202	97	53	124	78	-27	-25
Fort Wayne, IN	233	195	109	78	124	117	36	23	44	31	-8	-8
Grand Rapids, MI	541	471	281	221	261	250	109	83	123	96	-14	-13
Greensboro, NC	299	256	140	105	159	151	47	32	65	49	-17	-17
Houston, TX	1878	1210	610	152	1268	1058	-134	-244	221	75	-355	-318
Huntsville, AL	223	184	95	64	128	120	32	17	49	33	-17	-16
Indianapolis, IN	510	430	234	168	276	262	78	51	99	71	-21	-20
Jackson, MS	110	83	42	22	68	62	7	0	18	10	-11	-10
Jacksonville, FL	342	278	158	106	184	172	58	31	92	63	-34	-32
Jersey City, NJ	484	413	239	180	244	233	88	62	106	79	-18	-17
Johnstown, PA	28	25	15	12	14	13	6	5	7	6	-1	-1
Kansas City, MO	661	567	326	247	335	319	155	113	180	137	-26	-24
Kansas City, KS	100	86	51	39	50	47	25	18	29	22	-4	-4
Kingston, NY	73	65	38	32	35	33	15	12	18	15	-2	-2
Knoxville, TN	230	200	111	85	119	114	45	32	59	46	-14	-14
Los Angeles, CA	2683	1517	972	147	1711	1369	-311	-482	247	59	-558	-541
Lafayette, LA	138	98	48	18	90	79	-2	-10	19	9	-21	-18

Las Vegas, NV	1836	1274	861	405	975	870	284	114	352	175	-68	-61
Lexington, KY	193	160	87	60	106	99	29	17	40	27	-11	-10
Lincoln, NE	225	177	105	66	120	111	42	25	49	31	-7	-6
Lake Charles, LA	82	58	29	12	54	47	0	-5	13	6	-13	-12
Louisville, KY	435	362	194	136	241	227	63	38	86	60	-23	-22
Little Rock, AR	171	129	73	40	98	89	25	9	38	21	-13	-12
Lubbock, TX	124	82	50	18	74	65	5	-6	21	8	-16	-14
Madison, WI	397	343	180	136	216	207	56	40	67	51	-11	-10
Memphis, TN	403	337	188	134	214	202	76	48	104	74	-27	-26
Miami, FL	582	259	263	57	319	202	-82	-232	157	37	-239	-269
Milwaukee, WI	439	372	210	154	229	218	88	60	102	74	-14	-14
Minneapolis/St. Paul, MN	1312	1156	612	484	700	672	229	177	253	200	-23	-22
Mobile, AL	97	73	39	21	57	52	10	1	21	12	-11	-10
Modesto, CA	248	211	138	105	111	106	52	36	70	53	-18	-17
Muskegon, MI	172	156	95	82	77	75	49	42	54	47	-5	-5
Nashville, TN	472	397	220	159	252	238	86	56	115	83	-29	-27
Newport News, VA	80	67	41	30	40	38	16	11	20	15	-4	-4
New Orleans, LA	461	413	235	194	226	219	118	94	145	121	-27	-26
Norfolk, VA	104	89	53	41	51	49	22	16	27	21	-5	-5
Newark, NJ	636	544	316	238	320	306	118	83	141	106	-23	-22
New York, NY	5627	4616	2759	1910	2869	2707	1032	650	1250	855	-218	-206
Oakland, CA	634	549	382	305	252	244	83	49	176	139	-93	-90
Oklahoma City, OK	487	364	218	119	269	245	77	31	114	65	-38	-34
Olympia, WA	240	212	152	127	88	85	51	41	59	49	-9	-8
Omaha, NE	438	359	202	138	235	221	82	54	94	65	-12	-11
Orlando, FL	569	462	277	189	292	273	113	61	186	129	-73	-68
Philadelphia, PA	852	734	434	334	418	400	169	124	200	153	-31	-30
Phoenix, AZ	2608	364	874	175	1734	189	10	-1336	187	72	-177	-1408
Pittsburgh, PA	493	440	237	193	256	247	88	68	108	87	-20	-19
Portland, OR	1048	912	664	541	383	371	227	177	261	210	-34	-33
Providence, RI	297	247	154	111	144	136	63	43	73	53	-10	-10
Raleigh, NC	902	756	412	293	490	463	125	76	180	128	-55	-52
Richmond, VA	352	300	169	126	183	175	57	39	75	56	-17	-17
Riverside, CA	862	639	424	235	439	404	87	8	199	112	-112	-103
Rochester, NY	331	300	175	149	156	152	78	64	89	75	-11	-11
Sacramento, CA	788	655	414	299	375	356	124	76	179	127	-54	-52
Salt Lake City, UT	1191	989	728	547	464	442	349	254	398	300	-48	-46
San Antonio, TX	782	422	251	62	530	360	-68	-184	88	34	-156	-218
San Bernardino, CA	713	599	338	243	375	356	75	35	159	115	-84	-80
San Diego, CA	1001	645	677	347	325	298	180	-1	416	215	-237	-217
San Francisco, CA	235	200	180	147	55	54	57	39	98	79	-41	-40
San Jose, CA	663	573	308	233	355	340	-4	-26	103	76	-107	-103
Seattle, WA	1147	1048	782	691	365	357	320	277	351	308	-31	-31

Shreveport, LA	91	64	35	15	56	50	6	-2	16	7	-10	-9
Spokane, WA	573	487	380	301	194	186	184	145	191	152	-7	-7
Santa Ana/Anaheim, CA	918	689	534	330	384	359	89	-5	279	173	-190	-177
St. Louis, MO	208	179	97	73	111	106	40	28	48	36	-8	-8
Stockton, CA	328	285	185	147	143	138	63	45	90	71	-27	-26
St. Petersburg, FL	285	199	112	47	173	153	17	-15	71	32	-54	-47
Syracuse, NY	189	166	103	82	87	83	42	32	48	38	-6	-6
Tacoma, WA	647	574	423	356	224	218	162	132	182	152	-20	-20
Tampa, FL	542	405	235	127	307	278	67	9	153	86	-86	-77
Toledo, OH	143	119	67	48	76	72	22	15	27	19	-5	-4
Topeka, KS	69	57	35	25	34	32	16	11	19	14	-3	-3
Tucson, AZ	127	62	43	11	84	51	-3	-26	10	4	-13	-30
Tulsa, OK	423	324	204	122	218	201	89	46	116	71	-27	-25
Wichita, KS	256	189	121	66	135	123	51	23	64	35	-13	-12
Worcester, MA	349	300	174	133	174	167	65	46	76	57	-11	-11

CHAPTER V

CONCLUSIONS

This thesis investigates extreme temperature events, including their drivers, corresponding metric changes, and societal impact. We find that the main large-scale drivers causing an increase in extreme heat events are global warming and ENSO (Chapter 2). Given that global warming is a long-term trend and ENSO is an internal variability of the climate, the impact of ENSO is greater in small regions, but the impact of global warming grows with the size of the regions. We also find the change of heat related metric with warmer climate. With 3°C of warming, which we are currently on track for, 10% of the population will experience over 132 deadly days (DD) and over 232 tropical nights (TN) per year. And 10% of the population will face temperatures in excess of 47°C and 30°C wet-bulb temperature. We also discover that most heat-related metrics increase significantly between 1.5°C and 2.0°C of global warming, supporting the Paris Agreement's goal of limiting global warming below 1.5°C and well below 2.0°C.

We have also examined the societal impact of extreme temperature events. There are three primary findings on this aspect. The first is economic inequity on projected extreme heat events (Chapter 2). The findings of Chapter 2 verify that the increase in frequency and magnitude of extreme heat is expected to disproportionately affect the poor. Given the high cost of adaptation and mitigation to higher temperatures, this conclusion highlights the moral aspect of climate change.

Secondly, this dissertation concludes that the current ERCOT method, which uses the last two decade's weather data to forecast future power demand, is insufficient to represent climate change and variability outside of the very recent decade (Chapter 3). Using the model developed

in Chapter 3, we found that ERCOT's electricity grid has little spare capacity. In the summer and winter 2022, there was a 17% and 19% chance power demand in Texas would exceed ERCOT's extreme peak-load scenario. Furthermore, in the Texas winter storm Uri in 2021, this study concludes that power demand in Texas exceeded ERCOT's extreme peak load scenario by 15 GW, or 22%. We encourage ERCOT to make probabilistic temperature forecasts using modern tools, such as climate model ensembles, as done in this dissertation.

Finally, this dissertation examines forecasting future temperature-related deaths in the US (Chapter 4). Using the advanced temperature-mortality regression model that integrates future climate change, population/demographic change, and adaptation, this dissertation reveals that temperature-related deaths will increase rapidly in the future. We found that annual temperature-related deaths will increase from 36,444 deaths today to 175,000 per year with 3°C of warming. The aging population is the primary driver, and the role of climate change is relatively minor below 3°C of global average warming because increases in heat-related deaths and decreases in cold-related deaths cancel each other. However, above 3°C, the increase in heat-related deaths outpaces cold-related deaths. The role of adaptation is also examined, and it is found to reduce temperature-related mortality. While total numbers of temperature-related deaths might not change, we do find a northward shift of deaths. This arises because Southern cities are already well adapted to heat, so that the reduction in cold-related mortality outpaces increases warm-related mortality. At higher latitudes, this is not the case and heat-related mortality dominates.

Although this dissertation examined the causes and impacts of extreme temperature events, there are several additional studies to be conducted related to this topic. This dissertation focused solely on large-scale drivers of extreme heat, such as global warming or ENSO. However, more regional drivers of extreme temperatures, such as the urban heat island effect, should be

investigated for a more detailed understanding of urban extreme temperature events. Furthermore, the impact of extreme temperature events on economic inequity, power demand in Texas, and temperature-related deaths in the US were the focus of this dissertation. More human and natural system sectors should be investigated, such as transportation, agriculture, dairy farming, and fishery. However, this dissertation can serve as capstone research for climate informatics, which integrates climate data and data from other sectors to investigate the climate impact.

REFERENCES

Allen, M., Antwi-Agyei, P., Aragon-Durand, F., Babiker, M., Bertoldi, P., Bind, M., . . . Cartwright, A. (2019). Technical Summary: Global warming of 1.5° C. An IPCC Special Report on the impacts of global warming of 1.5° C above pre-industrial levels and related global greenhouse gas emission pathways, in the context of strengthening the global response to the threat of climate change, sustainable development, and efforts to eradicate poverty.

Almuhtady, A., Alshwawra, A., Alfaouri, M., Al-Kouz, W., & Al-Hinti, I. (2019). Investigation of the trends of electricity demands in Jordan and its susceptibility to the ambient air temperature towards sustainable electricity generation. *Energy, Sustainability and Society, 9*(1), 1-18.

Anderson, G. B., Oleson, K. W., Jones, B., & Peng, R. D. (2018). Projected trends in high-mortality heatwaves under different scenarios of climate, population, and adaptation in 82 US communities. *Climatic change, 146*(3), 455-470.

Arbuthnott, K., Hajat, S., Heaviside, C., & Vardoulakis, S. (2016). Changes in population susceptibility to heat and cold over time: assessing adaptation to climate change. *Environmental Health, 15*(1), 73-93.

Argaud, L., Ferry, T., Le, Q. H., Marfisi, A., Ciorba, D., Achache, P., . . . Robert, D. (2007). Short- and long-term outcomes of heatstroke following the 2003 heat wave in Lyon, France. *Archives of Internal Medicine, 167*(20), 2177-2183. doi:DOI 10.1001/archinte.167.20.ioi70147

Åström, D. O., Forsberg, B., Edvinsson, S., & Rocklöv, J. (2013). Acute fatal effects of short-lasting extreme temperatures in Stockholm, Sweden: evidence across a century of change. *Epidemiology, 24*(6), 820-829.

Auffhammer, M., Baylis, P., & Hausman, C. H. (2017). Climate change is projected to have severe impacts on the frequency and intensity of peak electricity demand across the United States. *Proceedings of the National Academy of Sciences, 114*(8), 1886-1891.

Baldwin, J. W., Dessy, J. B., Vecchi, G. A., & Oppenheimer, M. (2019). Temporally Compound Heat Wave Events and Global Warming: An Emerging Hazard. *Earths Future, 7*(4), 411-427. doi:10.1029/2018ef000989

Barnett, A. G. (2007). Temperature and cardiovascular deaths in the US elderly: changes over time. *Epidemiology, 18*(3), 369-372.

Barreca, A., Clay, K., Deschenes, O., Greenstone, M., & Shapiro, J. S. (2016). Adapting to climate change: The remarkable decline in the US temperature-mortality relationship over the twentieth century. *Journal of Political Economy, 124*(1), 105-159.

Barreca, A. I. (2012). Climate change, humidity, and mortality in the United States. *Journal of Environmental Economics and Management, 63*(1), 19-34.

Berko, J. (2014). *Deaths attributed to heat, cold, and other weather events in the United States, 2006-2010*: US Department of Health and Human Services, Centers for Disease Control and ….

Birk, K., Lupo, A. R., Guinan, P., & Barbieri, C. (2010). The interannual variability of midwestern temperatures and precipitation as related to the ENSO and PDO. *Atmosfera, 23*(2), 95-128.

Black, B. A., Lamarque, J.-F., Marsh, D. R., Schmidt, A., & Bardeen, C. G. (2021). Global climate disruption and regional climate shelters after the Toba supereruption. *Proceedings of the National Academy of Sciences, 118*(29), e2013046118.

Bobb, J. F., Peng, R. D., Bell, M. L., & Dominici, F. (2014). Heat-related mortality and adaptation to heat in the United States. *Environmental health perspectives, 122*(8), 811-816.

Bonan, G. B., Oleson, K. W., Vertenstein, M., Levis, S., Zeng, X., Dai, Y., . . . Yang, Z.-L. (2002). The land surface climatology of the Community Land Model coupled to the NCAR Community Climate Model. *Journal of climate, 15*(22), 3123-3149.

Busby, J. W., Baker, K., Bazilian, M. D., Gilbert, A. Q., Grubert, E., Rai, V., . . . Webber, M. E. (2021). Cascading risks: Understanding the 2021 winter blackout in Texas. *Energy Research & Social Science, 77*, 102106.

Buzan, J., Oleson, K., & Huber, M. (2015). Implementation and comparison of a suite of heat stress metrics within the Community Land Model version 4.5. *Geoscientific Model Development, 8*(2), 151-170.

Buzan, J. R., & Huber, M. (2020). Moist heat stress on a hotter Earth. *Annual Review of Earth and Planetary Sciences, 48*.

Carleton, T., Jina, A., Delgado, M., Greenstone, M., Houser, T., Hsiang, S., . . . Nath, I. (2022). Valuing the global mortality consequences of climate change accounting for adaptation costs and benefits. *The Quarterly Journal of Economics, 137*(4), 2037-2105.

Carson, C., Hajat, S., Armstrong, B., & Wilkinson, P. (2006). Declining vulnerability to temperature-related mortality in London over the 20th century. *American journal of epidemiology, 164*(1), 77-84.

Chapman, C. C., Lea, M.-A., Meyer, A., Sallée, J.-B., & Hindell, M. (2020). Defining Southern Ocean fronts and their influence on biological and physical processes in a changing climate. *Nature Climate Change, 10*(3), 209-219.

Chen, R. D., & Lu, R. Y. (2014). Dry Tropical Nights and Wet Extreme Heat in Beijing: Atypical Configurations between High Temperature and Humidity. *Monthly Weather Review, 142*(5), 1792-1802. doi:10.1175/Mwr-D-13-00289.1

Chow, W. T., Chuang, W.-C., & Gober, P. (2012). Vulnerability to extreme heat in metropolitan Phoenix: spatial, temporal, and demographic dimensions. *The Professional Geographer, 64*(2), 286-302.

Chylek, P., Li, J., Dubey, M., Wang, M., & Lesins, G. (2011). Observed and model simulated 20th century Arctic temperature variability: Canadian earth system model CanESM2. *Atmospheric Chemistry and Physics Discussions, 11*(8), 22893-22907.

CIESIN. (2016). Gridded population of the world, version 4 (GPWv4): Population count. Palisades, NY: NASA socioeconomic data and applications center (SEDAC). *Center for International Earth Science Information Network (CIESIN) Columbia University*.

Collins, W., Bellouin, N., Doutriaux-Boucher, M., Gedney, N., Halloran, P., Hinton, T., . . . Liddicoat, S. (2011). Development and evaluation of an Earth-System model–HadGEM2. *Geoscientific Model Development, 4*(4), 1051-1075.

Colucci, R. R., & Guglielmin, M. (2019). Climate change and rapid ice melt: Suggestions from abrupt permafrost degradation and ice melting in an alpine ice cave. *Progress in Physical Geography: Earth and Environment, 43*(4), 561-573.

Craig, M. T., Jaramillo, P., Hodge, B.-M., Nijssen, B., & Brancucci, C. (2020). Compounding climate change impacts during high stress periods for a high wind and solar power system in Texas. *Environmental Research Letters, 15*(2), 024002.

Dahl, K., Licker, R., Abatzoglou, J. T., & Declet-Barreto, J. (2019). Increased frequency of and population exposure to extreme heat index days in the United States during the 21st century. *Environmental Research Communications, 1*(7), 075002.

Davies-Jones, R. (2008). An efficient and accurate method for computing the wet-bulb temperature along pseudoadiabats. *Monthly Weather Review, 136*(7), 2764-2785.

Davis, R. E., Knappenberger, P. C., Michaels, P. J., & Novicoff, W. M. (2003). Changing heat-related mortality in the United States. *Environmental health perspectives, 111*(14), 1712-1718.

de Lima, C. Z., Buzan, J. R., Moore, F. C., Baldos, U. L. C., Huber, M., & Hertel, T. W. (2021). Heat stress on agricultural workers exacerbates crop impacts of climate change. *Environmental Research Letters, 16*(4), 044020.

De Rosa, M., Bianco, V., Scarpa, F., & Tagliafico, L. A. (2014). Heating and cooling building energy demand evaluation; a simplified model and a modified degree days approach. *Applied energy, 128*, 217-229.

de Schrijver, E., Bundo, M., Ragettli, M. S., Sera, F., Gasparrini, A., Franco, O. H., & Vicedo-Cabrera, A. M. (2022). Nationwide analysis of the heat-and cold-related mortality trends in Switzerland between 1969 and 2017: the role of population aging. *Environmental health perspectives, 130*(3), 037001.

Dee, D. P., Uppala, S. M., Simmons, A. J., Berrisford, P., Poli, P., Kobayashi, S., . . . Vitart, F. (2011). The ERA-Interim reanalysis: configuration and performance of the data assimilation system. *Quarterly Journal of the Royal Meteorological Society, 137*(656), 553-597. doi:10.1002/qj.828

Demoury, C., Aerts, R., Vandeninden, B., Van Schaeybroeck, B., & De Clercq, E. M. (2022). Impact of Short-Term Exposure to Extreme Temperatures on Mortality: A Multi-City Study in Belgium. *International Journal of Environmental Research and Public Health, 19*(7), 3763.

Deschenes, O., & Moretti, E. (2009). Extreme weather events, mortality, and migration. *The Review of Economics and Statistics, 91*(4), 659-681.

Deschênes, O., & Greenstone, M. (2011). Climate change, mortality, and adaptation: Evidence from annual fluctuations in weather in the US. *American Economic Journal: Applied Economics, 3*(4), 152-185.

Deser, C., Phillips, A., Bourdette, V., & Teng, H. Y. (2012). Uncertainty in climate change projections: the role of internal variability. *Climate Dynamics, 38*(3-4), 527-546. doi:10.1007/s00382-010-0977-x

Deser, C., & Trenberth, K. E. (2016). The Climate Data Guide: Pacific Decadal Oscillation (PDO): Definition and Indices. Retrieved from https://climatedataguide.ucar.edu/climate-data/pacific-decadal-oscillation-pdo-definition-and-indices

Dibike, Y. B., & Coulibaly, P. (2006). Temporal neural networks for downscaling climate variability and extremes. *Neural Networks, 19*(2), 135-144. doi:10.1016/j.neunet.2006.01.003

Dickinson, R. E., Oleson, K. W., Bonan, G., Hoffman, F., Thornton, P., Vertenstein, M., . . . Zeng, X. (2006). The Community Land Model and its climate statistics as a component of the Community Climate System Model. *Journal of Climate, 19*(11), 2302-2324.

Diffenbaugh, N. S., & Burke, M. (2019). Global warming has increased global economic inequality. *Proceedings of the National Academy of Sciences, 116*(20), 9808-9813.

Dimitrova, A., Ingole, V., Basagana, X., Ranzani, O., Mila, C., Ballester, J., & Tonne, C. (2021). Association between ambient temperature and heat waves with mortality in South Asia: Systematic review and meta-analysis. *Environment International, 146*, 106170.

Doss-Gollin, J., Farnham, D. J., Lall, U., & Modi, V. (2021). How unprecedented was the February 2021 Texas cold snap? *Environmental Research Letters, 16*(6), 064056.

Dunne, J., Horowitz, L., Adcroft, A., Ginoux, P., Held, I., John, J., . . . Paulot, F. (2020). The GFDL Earth System Model version 4.1 (GFDL-ESM 4.1): Overall coupled model description and simulation characteristics. *Journal of Advances in Modeling Earth Systems, 12*(11), e2019MS002015.

Erlykin, A., Sloan, T., & Wolfendale, A. (2009). Solar activity and the mean global temperature. *Environmental Research Letters, 4*(1), 014006.

Feng, S., & Hao, Z. (2021). Quantitative contribution of ENSO to precipitation-temperature dependence and associated compound dry and hot events. *Atmospheric Research, 260*, 105695.

Fischer, E. M., & Schär, C. (2010). Consistent geographical patterns of changes in high-impact European heatwaves. *Nature Geoscience, 3*(6), 398-403.

Folkerts, M. A., Bröde, P., Botzen, W., Martinius, M. L., Gerrett, N., Harmsen, C. N., & Daanen, H. A. (2020). Long term adaptation to heat stress: Shifts in the minimum mortality temperature in the Netherlands. *Frontiers in Physiology, 11*, 225.

Fouillet, A., Rey, G., Wagner, V., Laaidi, K., Empereur-Bissonnet, P., Le Tertre, A., . . . De Crouy-Chanel, P. (2008). Has the impact of heat waves on mortality changed in France since the European heat wave of summer 2003? A study of the 2006 heat wave. *International journal of epidemiology, 37*(2), 309-317.

Franco, G., & Sanstad, A. H. (2008). Climate change and electricity demand in California. *Climatic Change, 87*(1), 139-151.

Frankenfield, J. (2021, 2/20/2021). Texas Seeks Relief as Winter Storm Damage Piles Up. *The New York Times*.

Frölicher, T. L., Winton, M., & Sarmiento, J. L. (2014). Continued global warming after CO2 emissions stoppage. *Nature Climate Change, 4*(1), 40-44.

Gasparrini, A. (2014). Modeling exposure–lag–response associations with distributed lag non-linear models. *Statistics in medicine, 33*(5), 881-899.

Gasparrini, A., & Armstrong, B. (2011). The impact of heat waves on mortality. *Epidemiology (Cambridge, Mass.), 22*(1), 68.

Gasparrini, A., & Armstrong, B. (2013). Reducing and meta-analysing estimates from distributed lag non-linear models. *BMC medical research methodology, 13*(1), 1-10.

Gasparrini, A., Armstrong, B., & Kenward, M. G. (2012). Multivariate meta-analysis for non-linear and other multi-parameter associations. *Statistics in medicine, 31*(29), 3821-3839.

Gasparrini, A., Guo, Y., Hashizume, M., Kinney, P. L., Petkova, E. P., Lavigne, E., . . . Leone, M. (2015). Temporal variation in heat–mortality associations: a multicountry study. *Environmental health perspectives, 123*(11), 1200-1207.

Gasparrini, A., Guo, Y., Hashizume, M., Lavigne, E., Zanobetti, A., Schwartz, J., . . . Forsberg, B. (2015). Mortality risk attributable to high and low ambient temperature: a multicountry observational study. *The lancet, 386*(9991), 369-375.

Gasparrini, A., Guo, Y., Sera, F., Vicedo-Cabrera, A. M., Huber, V., Tong, S., . . . Correa, P. M. (2017). Projections of temperature-related excess mortality under climate change scenarios. *The Lancet Planetary Health, 1*(9), e360-e367.

Gosling, S. N., McGregor, G. R., & Lowe, J. A. (2009). Climate change and heat-related mortality in six cities Part 2: climate model evaluation and projected impacts from changes in the mean and variability of temperature with climate change. *International journal of biometeorology, 53*(1), 31-51.

Guan, H., Beecham, S., Xu, H., & Ingleton, G. (2017). Incorporating residual temperature and specific humidity in predicting weather-dependent warm-season electricity consumption. *Environmental Research Letters, 12*(2), 024021.

Guan, H., Soebarto, V., Bennett, J., Clay, R., Andrew, R., Guo, Y., . . . Bellette, K. (2014). Response of office building electricity consumption to urban weather in Adelaide, South Australia. *Urban Climate, 10*, 42-55.

Guo, Y., Barnett, A. G., Pan, X., Yu, W., & Tong, S. (2011). The impact of temperature on mortality in Tianjin, China: a case-crossover design with a distributed lag nonlinear model. *Environmental health perspectives, 119*(12), 1719-1725.

Hajat, S., Vardoulakis, S., Heaviside, C., & Eggen, B. (2014). Climate change effects on human health: projections of temperature-related mortality for the UK during the 2020s, 2050s and 2080s. *J Epidemiol Community Health, 68*(7), 641-648.

Hao, Z., Hao, F., Singh, V. P., & Zhang, X. (2018). Quantifying the relationship between compound dry and hot events and El Niño–southern Oscillation (ENSO) at the global scale. *Journal of Hydrology, 567*, 332-338.

Harrington, L. J., Frame, D., King, A. D., & Otto, F. E. (2018). How uneven are changes to impact-relevant climate hazards in a 1.5° C world and beyond? *Geophysical Research Letters, 45*(13), 6672-6680.

Harrington, L. J., Frame, D. J., Fischer, E. M., Hawkins, E., Joshi, M., & Jones, C. D. (2016). Poorest countries experience earlier anthropogenic emergence of daily temperature extremes. *Environmental Research Letters, 11*(5), 055007.

Hauer, M. E. (2019). Population projections for US counties by age, sex, and race controlled to shared socioeconomic pathway. *Scientific data, 6*(1), 1-15.

Hausfather, Z., & Peters, G. P. (2020). Emissions–the 'business as usual'story is misleading. In: Nature Publishing Group.

Heo, S., Bell, M. L., & Lee, J. T. (2019). Comparison of health risks by heat wave definition: Applicability of wet-bulb globe temperature for heat wave criteria. *Environmental Research, 168*, 158-170. doi:10.1016/j.envres.2018.09.032

Hersbach, H., Bell, B., Berrisford, P., Hirahara, S., Horányi, A., Muñoz-Sabater, J., . . . Schepers, D. (2020). The ERA5 global reanalysis. *Quarterly Journal of the Royal Meteorological Society, 146*(730), 1999-2049.

Heutel, G., Miller, N. H., & Molitor, D. (2021). Adaptation and the mortality effects of temperature across US climate regions. *Review of Economics and Statistics, 103*(4), 740-753.

Hintz, M. J., Luederitz, C., Lang, D. J., & von Wehrden, H. (2018). Facing the heat: A systematic literature review exploring the transferability of solutions to cope with urban heat waves. *Urban Climate, 24*, 714-727.

Hoegh-Guldberg, O., Jacob, D., Bindi, M., Brown, S., Camilloni, I., Diedhiou, A., . . . Guiot, J. (2018). Impacts of 1.5 C global warming on natural and human systems. *Global warming of 1.5° C. An IPCC Special Report*.

Ihara, T., Genchi, Y., Sato, T., Yamaguchi, K., & Endo, Y. (2008). City-block-scale sensitivity of electricity consumption to air temperature and air humidity in business districts of Tokyo, Japan. *Energy, 33*(11), 1634-1645.

IPCC. (2022). Climate Change 2022: Impacts, Adaptation, and Vulnerability. Contribution of Working Group II to the Sixth Assessment Report of the Intergovernmental Panel on Climate Change. *Cambridge University Press*. doi:10.1017/9781009325844

Ivanova, I. (2021, 2/25/2021). Texas winter storm costs could top $200 billion — more than hurricanes Harvey and Ike. *CBS News*.

Jackson, J. E., Yost, M. G., Karr, C., Fitzpatrick, C., Lamb, B. K., Chung, S. H., . . . Fenske, R. A. (2010). Public health impacts of climate change in Washington State: projected mortality risks due to heat events and air pollution. *Climatic change, 102*(1), 159-186.

Jay, O., Capon, A., Berry, P., Broderick, C., de Dear, R., Havenith, G., . . . Malik, A. (2021). Reducing the health effects of hot weather and heat extremes: from personal cooling strategies to green cities. *The lancet, 398*(10301), 709-724.

Jenkins, K., Hall, J., Glenis, V., Kilsby, C., McCarthy, M., Goodess, C., . . . Birkin, M. (2014). Probabilistic spatial risk assessment of heat impacts and adaptations for London. *Climatic change, 124*(1), 105-117.

Jovanović, S., Savić, S., Bojić, M., Djordjević, Z., & Nikolić, D. (2015). The impact of the mean daily air temperature change on electricity consumption. *Energy, 88*, 604-609.

Kalkstein, L. S., & Greene, J. S. (1997). An evaluation of climate/mortality relationships in large US cities and the possible impacts of a climate change. *Environmental health perspectives, 105*(1), 84-93.

Kang, S., & Eltahir, E. A. B. (2018). North China Plain threatened by deadly heatwaves due to climate change and irrigation. *Nat Commun, 9*(1), 2894. doi:10.1038/s41467-018-05252-y

Kay, J. E., Deser, C., Phillips, A., Mai, A., Hannay, C., Strand, G., . . . Edwards, J. (2015). The Community Earth System Model (CESM) large ensemble project: A community resource for studying climate change in the presence of internal climate variability. *Bulletin of the American Meteorological Society, 96*(8), 1333-1349.

Kay, J. E., Deser, C., Phillips, A., Mai, A., Hannay, C., Strand, G., . . . Vertenstein, M. (2015). THE COMMUNITY EARTH SYSTEM MODEL (CESM) LARGE ENSEMBLE PROJECT A Community Resource for Studying Climate Change in the Presence of Internal Climate Variability. *Bulletin of the American Meteorological Society, 96*(8), 1333-1349. doi:10.1175/Bams-D-13-00255.1

Kharin, V. V., Flato, G. M., Zhang, X., Gillett, N. P., Zwiers, F., & Anderson, K. J. (2018). Risks from Climate Extremes Change Differently from 1.5 degrees C to 2.0 degrees C Depending on Rarity. *Earths Future, 6*(5), 704-715. doi:10.1002/2018ef000813

Kim, Y., & Lee, S. (2019). Trends of extreme cold events in the central regions of Korea and their influence on the heating energy demand. *Weather and Climate Extremes, 24*, 100199.

King, A. D., & Harrington, L. J. (2018). The inequality of climate change from 1.5 to 2 C of global warming. *Geophysical Research Letters, 45*(10), 5030-5033.

King, C. W., Rhodes, J. D., Zarnikau, J., Lin, N., Kutanoglu, E., Leibowicz, B., . . . Austgen, B. (2021). *The Timeline and Events of the February 2021 Texas Electric Grid Blackouts*: The University of Texas at Austin Energy Institute.

Knowlton, K., Lynn, B., Goldberg, R. A., Rosenzweig, C., Hogrefe, C., Rosenthal, J. K., & Kinney, P. L. (2007). Projecting heat-related mortality impacts under a changing climate in the New York City region. *American journal of public health, 97*(11), 2028-2034.

Koenigk, T., Key, J., & Vihma, T. (2020). Climate change in the Arctic. *Physics and chemistry of the Arctic atmosphere*, 673-705.

Kulk, G., Platt, T., Dingle, J., Jackson, T., Jönsson, B. F., Bouman, H. A., . . . Estrada, M. (2020). Primary production, an index of climate change in the ocean: satellite-based estimates over two decades. *Remote Sensing, 12*(5), 826.

Kummu, M. T., Maija; Guillaume, Joseph H. A. (2019). *Data from: Gridded global datasets for Gross Domestic Product and Human Development Index over 1990-2015 Dryad, Dataset, https://doi.org/10.5061/dryad.dk1j0*.

Kyselý, J., & Plavcová, E. (2012). Declining impacts of hot spells on mortality in the Czech Republic, 1986–2009: adaptation to climate change? *Climatic change, 113*(2), 437-453.

Lee, J., & Dessler, A. E. (2022). The Impact of Neglecting Climate Change and Variability on ERCOT's Forecasts of Electricity Demand in Texas. *Weather, Climate, and Society, 14*(2), 499-505.

Lee, J. Y., & Kim, H. (2016). Projection of future temperature-related mortality due to climate and demographic changes. *Environment International, 94*, 489-494.

Lelieveld, J., Hadjinicolaou, P., Kostopoulou, E., Chenoweth, J., El Maayar, M., Giannakopoulos, C., . . . Xoplaki, E. (2012). Climate change and impacts in the Eastern Mediterranean and the Middle East. *Climatic Change, 114*(3-4), 667-687. doi:10.1007/s10584-012-0418-4

Li, T., Horton, R. M., Bader, D. A., Zhou, M., Liang, X., Ban, J., . . . Kinney, P. L. (2016). Aging will amplify the heat-related mortality risk under a changing climate: projection for the elderly in Beijing, China. *Scientific reports, 6*(1), 1-9.

Liang, C., Zheng, G., Zhu, N., Tian, Z., Lu, S., & Chen, Y. (2011). A new environmental heat stress index for indoor hot and humid environments based on Cox regression. *Building and Environment, 46*(12), 2472-2479.

Likas, A., Vlassis, N., & Verbeek, J. J. (2003). The global k-means clustering algorithm. *Pattern Recognition, 36*(2), 451-461. Retrieved from <Go to ISI>://WOS:000179225600015

Lin, Y.-K., Ho, T.-J., & Wang, Y.-C. (2011). Mortality risk associated with temperature and prolonged temperature extremes in elderly populations in Taiwan. *Environmental research, 111*(8), 1156-1163.

Liu, Z., Anderson, B., Yan, K., Dong, W., Liao, H., & Shi, P. (2017). Global and regional changes in exposure to extreme heat and the relative contributions of climate and population change. *Scientific Reports, 7*(1), 1-9.

Lo, Y. E., Mitchell, D. M., Gasparrini, A., Vicedo-Cabrera, A. M., Ebi, K. L., Frumhoff, P. C., . . . Sparrow, S. (2019). Increasing mitigation ambition to meet the Paris Agreement's temperature goal avoids substantial heat-related mortality in US cities. *Science advances, 5*(6), eaau4373.

López-Moreno, J., Vicente-Serrano, S., Morán-Tejeda, E., Lorenzo-Lacruz, J., Kenawy, A., & Beniston, M. (2011). Effects of the North Atlantic Oscillation (NAO) on combined temperature and precipitation winter modes in the Mediterranean mountains: Observed relationships and projections for the 21st century. *Global and Planetary Change, 77*(1-2), 62-76.

Luber, G., & McGeehin, M. (2008). Climate change and extreme heat events. *American journal of preventive medicine, 35*(5), 429-435.

Lundgren, K., Kuklane, K., Gao, C., & Holmer, I. (2013). Effects of heat stress on working populations when facing climate change. *Industrial health, 51*(1), 3-15.

Ma, W., Wang, L., Lin, H., Liu, T., Zhang, Y., Rutherford, S., . . . Wang, X. (2015). The temperature–mortality relationship in China: an analysis from 66 Chinese communities. *Environmental research, 137*, 72-77.

Maher, N., Milinski, S., Suarez-Gutierrez, L., Botzet, M., Dobrynin, M., Kornblueh, L., . . . Marotzke, J. (2019). The Max Planck Institute Grand Ensemble: Enabling the Exploration of Climate System Variability. *Journal of Advances in Modeling Earth Systems, 11*(7), 2050-2069. doi:10.1029/2019ms001639

Mallen, E., Stone, B., & Lanza, K. (2019). A methodological assessment of extreme heat mortality modeling and heat vulnerability mapping in Dallas, Texas. *Urban Climate, 30*, 100528.

Mann, M. E., Steinman, B. A., Brouillette, D. J., & Miller, S. K. (2021). Multidecadal climate oscillations during the past millennium driven by volcanic forcing. *Science, 371*(6533), 1014-1019.

Marcotullio, P. J., Keßler, C., & Fekete, B. M. (2021). The future urban heat-wave challenge in Africa: Exploratory analysis. *Global Environmental Change, 66*, 102190.

Mariano, E., Carolina, V., & Miranda Leandro, A. (2018). Influences of ENSO and PDO phenomena on the local climate variability can drive extreme temperature and depth conditions in a Pampean shallow lake affecting fish communities. *Environmental Biology of Fishes, 101*(4), 653-666.

Marsh, G. E. (2014). Interglacials, Milankovitch cycles, solar activity, and carbon dioxide. *Journal of Climatology, 2014*.

Marsha, A., Sain, S., Heaton, M., Monaghan, A., & Wilhelmi, O. (2018). Influences of climatic and population changes on heat-related mortality in Houston, Texas, USA. *Climatic change, 146*(3), 471-485.

Martínez-Solanas, È., Quijal-Zamorano, M., Achebak, H., Petrova, D., Robine, J.-M., Herrmann, F. R., . . . Ballester, J. (2021). Projections of temperature-attributable mortality in Europe: a time series analysis of 147 contiguous regions in 16 countries. *The Lancet Planetary Health, 5*(7), e446-e454.

Masson-Delmotte, V., Zhai, P., Pörtner, H.-O., Roberts, D., Skea, J., Shukla, P. R., . . . Pidcock, R. (2018). Global warming of 1.5 C. *An IPCC Special Report on the impacts of global warming of, 1*.

Mearns, L., McGinnis, S., Korytina, D., Arritt, R., Biner, S., Bukovsky, M., . . . Gutowski, W. (2017). *The NA-CORDEX dataset, version 1.0. NCAR Climate Data Gateway*.

Meehl, G. A., Tebaldi, C., Teng, H., & Peterson, T. C. (2007). Current and future US weather extremes and El Niño. *Geophysical Research Letters, 34*(20).

Melillo, J. M., Richmond, T., & Yohe, G. (2014). Climate change impacts in the United States. *Third national climate assessment, 52*.

Mirasgedis, S., Sarafidis, Y., Georgopoulou, E., Kotroni, V., Lagouvardos, K., & Lalas, D. (2007). Modeling framework for estimating impacts of climate change on electricity demand at regional level: case of Greece. *Energy Conversion and Management, 48*(5), 1737-1750.

Moore, G., & Renfrew, I. (2012). Cold European winters: interplay between the NAO and the East Atlantic mode. *Atmospheric Science Letters, 13*(1), 1-8.

Mora, C., Dousset, B., Caldwell, I. R., Powell, F. E., Geronimo, R. C., Bielecki, C. R., . . . Trauernicht, C. (2017). Global risk of deadly heat. *Nature Climate Change, 7*(7), 501-+. doi:10.1038/Nclimate3322

Morris, C. E., Gonzales, R. G., Hodgson, M. J., & Tustin, A. W. (2019). Actual and simulated weather data to evaluate wet bulb globe temperature and heat index as alerts for occupational heat-related illness. *Journal of Occupational and Environmental Hygiene, 16*(1), 54-65. doi:10.1080/15459624.2018.1532574

Muñoz-Sabater, J., Dutra, E., Agustí-Panareda, A., Albergel, C., Arduini, G., Balsamo, G., . . . Hersbach, H. (2021). ERA5-Land: A state-of-the-art global reanalysis dataset for land applications. *Earth System Science Data, 13*(9), 4349-4383.

Murata, A., Nakano, M., Kanada, S., Kurihara, K., & Sasaki, H. (2012). Summertime temperature extremes over Japan in the late 21st century projected by a high-resolution regional climate model. *Journal of the Meteorological Society of Japan. Ser. II, 90*, 101-122.

Murphy, S., Sowell, F., & Apt, J. (2019). A time-dependent model of generator failures and recoveries captures correlated events and quantifies temperature dependence. *Applied energy, 253*, 113513.

Muthers, S., Matzarakis, A., & Koch, E. (2010). Climate change and mortality in Vienna—a human biometeorological analysis based on regional climate modeling. *International Journal of Environmental Research and Public Health, 7*(7), 2965-2977.

Naughten, K. A., De Rydt, J., Rosier, S. H., Jenkins, A., Holland, P. R., & Ridley, J. K. (2021). Two-timescale response of a large Antarctic ice shelf to climate change. *Nature communications, 12*(1), 1-10.

North, G. R. (1984). Empirical orthogonal functions and normal modes. *Journal of Atmospheric Sciences, 41*(5), 879-887.

Overland, J. E. (2021). Causes of the record-breaking pacific northwest Heatwave, late June 2021. *Atmosphere, 12*(11), 1434.

Parkes, B., Cronin, J., Dessens, O., & Sultan, B. (2019). Climate change in Africa: costs of mitigating heat stress. *Climatic Change, 154*(3-4), 461-476.

Patel, L., Conlon, K. C., Sorensen, C., McEachin, S., Nadeau, K., Kakkad, K., & Kizer, K. W. (2022). Climate change and extreme heat events: how health systems should prepare. *NEJM Catalyst Innovations in Care Delivery, 3*(7), CAT. 21.0454.

Patz, J. A., Campbell-Lendrum, D., Holloway, T., & Foley, J. A. (2005). Impact of regional climate change on human health. *Nature, 438*(7066), 310-317. doi:10.1038/nature04188

Perkins, S., Alexander, L., & Nairn, J. (2012). Increasing frequency, intensity and duration of observed global heatwaves and warm spells. *Geophysical Research Letters, 39*(20).

Petkova, E. P., Vink, J. K., Horton, R. M., Gasparrini, A., Bader, D. A., Francis, J. D., & Kinney, P. L. (2017). Towards more comprehensive projections of urban heat-related mortality: estimates for New York City under multiple population, adaptation, and climate scenarios. *Environmental health perspectives, 125*(1), 47-55.

Porter, W. C., & Heald, C. L. (2019). The mechanisms and meteorological drivers of the summertime ozone–temperature relationship. *Atmospheric Chemistry and Physics, 19*(21), 13367-13381.

Psiloglou, B., Giannakopoulos, C., Majithia, S., & Petrakis, M. (2009). Factors affecting electricity demand in Athens, Greece and London, UK: A comparative assessment. *Energy, 34*(11), 1855-1863.

Qian, Y., Chakraborty, T., Li, J., Li, D., He, C., Sarangi, C., . . . Leung, L. R. (2022). Urbanization impact on regional climate and extreme weather: Current understanding, uncertainties, and future research directions. *Advances in Atmospheric Sciences*, 1-42.

Quinn, A., Tamerius, J. D., Perzanowski, M., Jacobson, J. S., Goldstein, I., Acosta, L., & Shaman, J. (2014). Predicting indoor heat exposure risk during extreme heat events. *Science of the total environment, 490*, 686-693.

Ren, C., Williams, G. M., Morawska, L., Mengersen, K., & Tong, S. (2008). Ozone modifies associations between temperature and cardiovascular mortality: analysis of the NMMAPS data. *Occupational and environmental medicine, 65*(4), 255-260.

Ruddell, D. M., Harlan, S. L., Grossman-Clarke, S., & Buyantuyev, A. (2009). Risk and exposure to extreme heat in microclimates of Phoenix, AZ. In *Geospatial techniques in urban hazard and disaster analysis* (pp. 179-202): Springer.

Russo, S., Sillmann, J., Sippel, S., Barcikowska, M. J., Ghisetti, C., Smid, M., & O'Neill, B. (2019). Half a degree and rapid socioeconomic development matter for heatwave risk. *Nature communications, 10*(1), 1-9.

Russo, S., Sillmann, J., & Sterl, A. (2017). Humid heat waves at different warming levels. *Scientific Reports, 7*. doi:ARTN 7477

10.1038/s41598-017-07536-7

Sailor, D. J., & Muñoz, J. R. (1997). Sensitivity of electricity and natural gas consumption to climate in the USA—Methodology and results for eight states. *Energy, 22*(10), 987-998.

Samet, J. M., Zeger, S. L., Dominici, F., Curriero, F., Coursac, I., Dockery, D. W., . . . Zanobetti, A. (2000). The national morbidity, mortality, and air pollution study. *Part II: morbidity and mortality from air pollution in the United States Res Rep Health Eff Inst, 94*(pt 2), 5-79.

Seager, R., Kushnir, Y., Nakamura, J., Ting, M., & Naik, N. (2010). Northern Hemisphere winter snow anomalies: ENSO, NAO and the winter of 2009/10. *Geophysical research letters, 37*(14).

SEDAC. (2018). *Gridded Population of the World, Version 4 (GPWv4): Population Density, Revision 11*.

Shi, J., Cui, L., Wen, K., Tian, Z., Wei, P., & Zhang, B. (2018). Trends in the consecutive days of temperature and precipitation extremes in China during 1961–2015. *Environmental Research, 161*, 381-391.

Shin, M., & Do, S. L. (2016). Prediction of cooling energy use in buildings using an enthalpy-based cooling degree days method in a hot and humid climate. *Energy and Buildings, 110*, 57-70.

Silberner, J. (2021). Heat wave causes hundreds of deaths and hospitalisations in Pacific north west. *BMJ: British Medical Journal (Online), 374*.

Simolo, C., Brunetti, M., Maugeri, M., & Nanni, T. (2011). Evolution of extreme temperatures in a warming climate. *Geophysical Research Letters, 38*. doi:Artn L16701
10.1029/2011gl048437

Sivak, M. (2009). Potential energy demand for cooling in the 50 largest metropolitan areas of the world: Implications for developing countries. *Energy Policy, 37*(4), 1382-1384.

Stokes, C. R., Abram, N. J., Bentley, M. J., Edwards, T. L., England, M. H., Foppert, A., . . . Lenaerts, J. (2022). Response of the East Antarctic Ice Sheet to past and future climate change. *Nature, 608*(7922), 275-286.

Stouffer, R. J., & Manabe, S. (2017). Assessing temperature pattern projections made in 1989. *Nature Climate Change, 7*(3), 163-165.

Sun, Y., Zhang, X., Zwiers, F. W., Song, L., Wan, H., Hu, T., . . . Ren, G. (2014). Rapid increase in the risk of extreme summer heat in Eastern China. *Nature Climate Change, 4*(12), 1082-1085.

Syakur, M. A., Khotimah, B. K., Rochman, E. M. S., & Satoto, B. D. (2018). Integration K-Means Clustering Method and Elbow Method For Identification of The Best Customer Profile Cluster. *2nd International Conference on Vocational Education and Electrical Engineering (Icvee), 336*. doi:Unsp 012017
10.1088/1757-899x/336/1/012017

Takahashi, K., Honda, Y., & Emori, S. (2007). Assessing mortality risk from heat stress due to global warming. *Journal of risk research, 10*(3), 339-354.

Tan, J. G., Zheng, Y. F., Tang, X., Guo, C. Y., Li, L. P., Song, G. X., . . . Chen, H. (2010). The urban heat island and its impact on heat waves and human health in Shanghai. *International Journal of Biometeorology, 54*(1), 75-84. doi:10.1007/s00484-009-0256-x

Thirumalai, K., DiNezio, P. N., Okumura, Y., & Deser, C. (2017). Extreme temperatures in Southeast Asia caused by El Nino and worsened by global warming. *Nat Commun, 8*, 15531. doi:10.1038/ncomms15531

Thompson, D. W. J., Barnes, E. A., Deser, C., Foust, W. E., & Phillips, A. S. (2015). Quantifying the Role of Internal Climate Variability in Future Climate Trends. *Journal of Climate, 28*(16), 6443-6456. doi:10.1175/Jcli-D-14-00830.1

Trenberth, K. E. (2020). The Climate Data Guide: Nino SST Indices (Nino 1+2, 3, 3.4, 4; ONI and TNI). Retrieved from https://climatedataguide.ucar.edu/climate-data/nino-sst-indices-nino-12-3-34-4-oni-and-tni

Trenberth, K. E., & Zhang, R. (2021). The Climate Data Guide: Atlantic Multi-decadal Oscillation (AMO). Retrieved from https://climatedataguide.ucar.edu/climate-data/atlantic-multi-decadal-oscillation-amo

Ulrich, R. N. (2022). When Texas went dark. *Nature Reviews Earth & Environment, 3*(2), 105-105.

Vardoulakis, S., Dear, K., Hajat, S., Heaviside, C., Eggen, B., & McMichael, A. J. (2014). Comparative assessment of the effects of climate change on heat-and cold-related mortality in the United Kingdom and Australia. *Environmental health perspectives, 122*(12), 1285-1292.

Vasquez, T. (2022). An Unprecedented Pacific Northwest Heat Wave Rings Alarm Bells. *Weatherwise, 75*(1), 22-27.

Vicedo-Cabrera, A. M., Guo, Y., Sera, F., Huber, V., Schleussner, C.-F., Mitchell, D., . . . Lavigne, E. (2018). Temperature-related mortality impacts under and beyond Paris Agreement climate change scenarios. *Climatic change, 150*(3), 391-402.

Wang, Y., Shi, L., Zanobetti, A., & Schwartz, J. D. (2016). Estimating and projecting the effect of cold waves on mortality in 209 US cities. *Environment International, 94*, 141-149.

Weinberger, K. R., Haykin, L., Eliot, M. N., Schwartz, J. D., Gasparrini, A., & Wellenius, G. A. (2017). Projected temperature-related deaths in ten large US metropolitan areas under different climate change scenarios. *Environment International, 107*, 196-204.

Wilhelmi, O. V., & Hayden, M. H. (2010). Connecting people and place: a new framework for reducing urban vulnerability to extreme heat. *Environmental Research Letters, 5*(1), 014021.

Wobus, C., Zarakas, C., Malek, P., Sanderson, B., Crimmins, A., Kolian, M., . . . Weaver, C. P. (2018). Reframing Future Risks of Extreme Heat in the United States. *Earths Future, 6*(9), 1323-1335. doi:10.1029/2018ef000943

Wood, A. W., Leung, L. R., Sridhar, V., & Lettenmaier, D. P. (2004). Hydrologic implications of dynamical and statistical approaches to downscaling climate model outputs. *Climatic Change, 62*(1-3), 189-216. doi:DOI 10.1023/B:CLIM.0000013685.99609.9e

Wuebbles, D. J., Fahey, D. W., & Hibbard, K. A. (2017). Climate science special report: fourth national climate assessment, volume I.

Yang, J., Zhou, M., Ren, Z., Li, M., Wang, B., Liu, D. L., . . . Tong, S. (2021). Projecting heat-related excess mortality under climate change scenarios in China. *Nature communications, 12*(1), 1-11.

Yi, W., & Chan, A. P. (2015). Effects of temperature on mortality in Hong Kong: a time series analysis. *International journal of biometeorology, 59*(7), 927-936.

Zhang, G., Zeng, G., Li, C., & Yang, X. (2020). Impact of PDO and AMO on interdecadal variability in extreme high temperatures in North China over the most recent 40-year period. *Climate Dynamics, 54*(5), 3003-3020.

Zhang, H., Wang, F., Li, J., Duan, Y., Zhu, C., & He, J. (2022). Potential impact of Tonga volcano eruption on global mean surface air temperature. In: Springer.

Zhang, Y., Li, C., Feng, R., Zhu, Y., Wu, K., Tan, X., & Ma, L. (2016). The short-term effect of ambient temperature on mortality in Wuhan, China: a time-series study using a distributed lag non-linear model. *International Journal of Environmental Research and Public Health, 13*(7), 722.

Zhou, C., & Wang, K. (2016). Coldest temperature extreme monotonically increased and hottest extreme oscillated over Northern Hemisphere land during last 114 years. *Scientific reports, 6*(1), 1-9.